Signal Extraction and Control for an Interferometric Gravitational Wave Detector

Thesis by

Martin W. Regehr

In Partial Fulfillment of the Requirements
for the Degree of
Doctor of Philosophy

California Institute of Technology
Pasadena, California

1995

(Submitted August 1, 1994)

To my Father

Acknowledgements

I am indebted to my three advisors: to Ron Drever, who accepted me into the LIGO team, to Fred Raab, without whose tremendous patience and valuable suggestions my experiment might never have been completed, and whose painstaking reading of this thesis eliminated countless errors therefrom, and to Amnon Yariv, whose interest, enthusiasm, and kindness have been a constant source of inspiration for me.

I am grateful to the entire LIGO team, whose support, technical and emotional, has been invaluable during my stay at Caltech, and especially to Alex Abramovici, Jake Chapsky, Torrey Lyons, David Shoemaker, Lisa Sievers and Stan Whitcomb, each of whom contributed very substantially to the work described herein.

This work was supported by the National Science Foundation cooperative agreement no. PHY-9210038.

Abstract

Large interferometers are currently under construction for the detection of gravitational radiation. These will contain a number of optical surfaces at each of which the relative phase of incident beams must be kept strictly controlled in order to achieve high sensitivity.

The type of interferometer considered here consists of two Fabry-Perot cavities illuminated by a laser beam which is split in half by a beam splitter, together with a recycling mirror between the laser and the beam splitter, which reflects light returning from the beam splitter toward the laser back into the interferometer. A scheme for sensing deviations from proper interference has been analyzed and the adequacy of this method for incorporation in a control system has been evaluated. The sensing scheme involves phase modulating the laser light incident on the interferometer, introducing an asymmetry in the distances between the Fabry-Perot cavities and the beam splitter, and demodulating the signals from photodetectors monitoring three optical outputs of the interferometer. These optical outputs are light returning to the laser, light extracted by a pick-off from between the recycling mirror and the beam splitter, and light leaving the interferometer at the beam splitter.

The analysis has shown that the matrix of transfer functions from mirror displacement to demodulated signal is ill-conditioned, that as many as three of the transfer functions may contain right half plane zeros, and that one of these transfer functions can be affected by the modulation depth. The performance of the closed-loop system, however, need not be significantly affected, provided that certain constraints are observed in the optical and electronic design.

A table-top interferometer has been constructed, to demonstrate the feasibility of constructing a control system using this sensing scheme and to compare the response of the interferometer with that predicted by calculations. Good agreement between the experiment and the calculation has been obtained.

Contents

List of Tables

List of Figures

Table of Mathematical Symbols

Symbol	Page number
l_I, l_P, L_I, L_P, δ, λ_{mod}, f_{mod}	6
v_1, v_2, v_3, v_4	8
Φ_+	10
Φ_-	11
ϕ_+	10
ϕ_-	11
Ω	16
E	16
E_l, E_{inc}	16
i_p	17
v_I, v_Q	18
r	19
t	19
N, N'	21
$r_c(\Phi_I)$	23
r_{c0}, r'_{c0}	23
T, R	25
E_r, E_f, E_{sym}, E_{retP}, E_{retI}, E_{anti}	24
r_{BS}, t_p	23
r_R	25
E_{ref}	25
r_{c1}, r'_{c1}	27
α	29
N_0, N_1	35

N'_0, N'_1	36
ω	41
$S_{0\,1}$	43
$E_{R\,-1\,-1}$	42
τ	44
K_{01}	44
V	45
τ_{arm}	53
τ_{rec}	56
M	66
P, P_+, P_-	99
ϵ	98
C, C_1, C_2	99
ξ_1, ξ_2, ω_a, Q_1, Q_2, K_1, K_2	101
ω_1, ω_2	105
d_1, d_2, e_1, e_2	108
S	109
Δ, G_1, G_2	111

Chapter 1 Introduction

In the year 1915, Albert Einstein published a theory which he called the General theory of Relativity. This theory interprets the force of gravity as a distortion of space and time produced by objects with mass. The theory also predicts that wave-like distortions of space and time be able to propagate across the universe, in a fashion similar to the propagation of electromagnetic waves. These waves would be produced by accelerating mass, much as electromagnetic waves are produced by accelerating charge. The direct detection of these waves would provide a strong confirmation of Einstein's theory. Their observation with good signal-to-noise ratio could provide a wealth of new information about the universe, since most anticipated sources of gravitational radiation are difficult to observe optically.

Although the General theory of Relativity is conceptually quite subtle, the effect of gravitational waves on detectors is simple: they produce a fluctuating shear strain transverse to the direction of propagation. This is shown in Fig. 1.1 for a gravitational wave propagating horizontally through a human being. Also visible from the size of the effect* indicated on this figure is the fact that a human being is not nearly sensitive enough to detect gravitational waves directly.

---

* The size shown is the rms amplitude of gravitational waves expected with a mean frequency of three times per year in bursts from coalescing compact binaries.

Figure 1.1 Effect that a horizontally propagating gravitational wave might have on a human being.

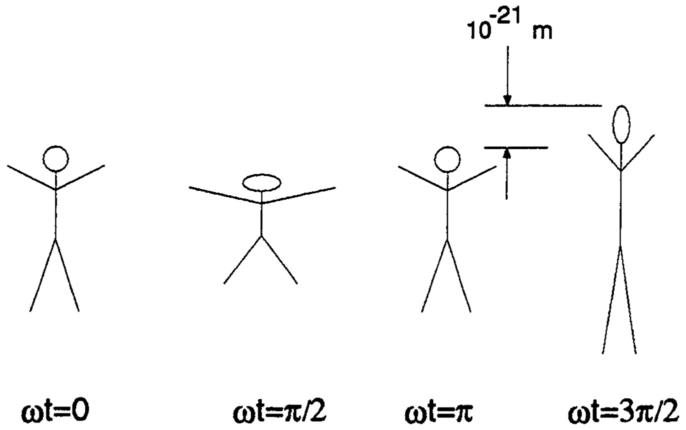

Figure 1.2 Michelson interferometer.

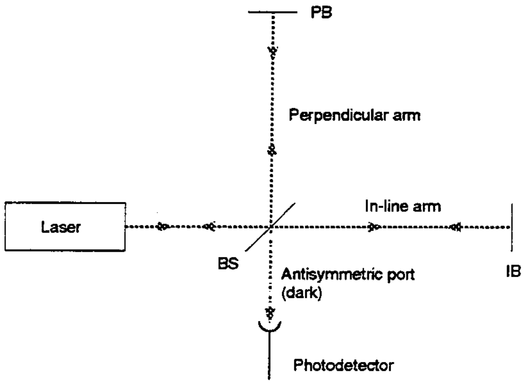

The fact that the wave produces a transverse shear strain makes the Michelson interferometer (Fig. 1.2) an obvious candidate for a detector and in fact early detectors used this configuration[1,2]. Interferometers currently being developed for LIGO (Laser Interferometer Gravitational Observatory[3]) will be variants (to be described below) of the Michelson interferometer.

If the detector is operated with the mirrors positioned so that the antisymmetric output is dark then a displacement of $\lambda/4$ (about 125 nanometers for green light) of either of the back mirrors PB and IB will cause the intensity at the output to change to full brightness. One easy way to increase the sensitivity is to increase the length of the arms. The planned LIGO detectors will have arms that are 4 km long. Since the gravitational wave strains space, stretching it in one direction and compressing it in the orthogonal direction, the change in length of an arm is equal to the size of the strain times the initial length of the arm.

Another way to increase the sensitivity of the detector is to have the light in each arm reflect several times from each back mirror. This can be accomplished by using an optical delay line[4], where the light strikes the mirror in a different spot on each traversal of the arm, or by using a "Fabry-Perot" resonant cavity[5], where light from many traversals interferes in a single spot on each mirror. In initial LIGO detectors the Fabry-Perot resonators (or "arm cavities") are formed by inserting partially transmitting "front" mirrors PF and IF between the beam splitter and the back mirrors, as shown in Figure 1.3. Such a cavity is said to be resonant when light entering through the partially transmitting front mirror interferes constructively with light traveling back and forth inside the resonator. Near resonance the phase of the light returning from the resonator is very sensitive to the length of the resonator, and the effect of the small displacement produced by a gravitational wave on the intensity at the output is magnified.

Larger signals can also be obtained by increasing the amount of power

Figure 1.3 Interferometer with Fabry-Perot arms.

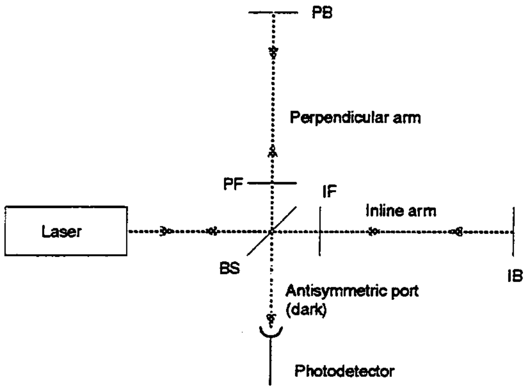

incident on the beam splitter*. This is accomplished, in a technique referred to as "power recycling,"[6] by inserting a (partially transmitting) "recycling mirror" R between the laser and the beam splitter as shown in Figure 1.4. If light returning from the arms to the beam splitter interferes destructively in the direction of the photodetector, then by energy conservation the light must interfere constructively in the direction of the laser. The recycling mirror allows this light to be reused. To do so, the recycling mirror must be placed so that the light it reflects back into the interferometer interferes constructively with fresh light transmitted through it from the laser.

This work addresses two problems that exist with the simple interferometric detector outlined thus far. The first problem is that the intensity at the output is minimum in the absence of a gravitational wave and increases when a gravitational wave distorts the arms in either direction. By symmetry, the signal is

---

* A more precise way to state the advantage obtained thus is to note that the signal to shot noise ratio is improved. We will discuss this in more detail in chapter 7.

Figure 1.4 Interferometer with power recycling.

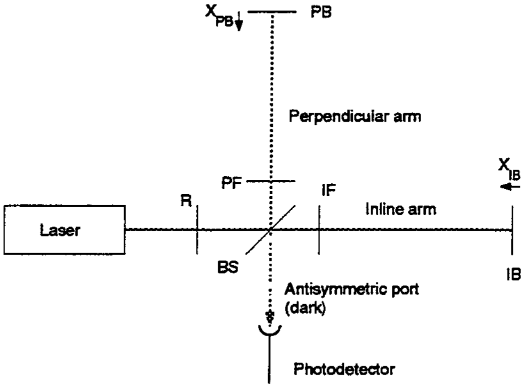

at best a quadratic function of the gravitational-wave induced distortion; thus $\frac{\partial i_p}{\partial(X_{PB}-X_{IB})} = 0$, where i_p is the signal from the photodetector, and X_{IB} and X_{PB} are the displacements of the two back mirrors, as shown in Figure 1.4.

The second problem is that it is virtually impossible to build a mechanical structure sufficiently stiff and thermally stable to hold the mirrors in the locations where the interference conditions are satisfied. (There are four such interference conditions, one for each optical surface where interference takes place: the two front mirrors, the beam splitter, and the recycling mirror.) In practice, the mirrors are individually suspended from wires (Figure 1.5)[†] in order to attenuate seismic noise which would otherwise shake the mirrors, imitating gravitational waves. While these passive suspensions reduce seismic noise at higher frequencies, they can amplify low-frequency seismic noise.

[†] Drawing courtesy of Aaron Gillespie.

Figure 1.5 Interferometer, showing mirror suspensions.

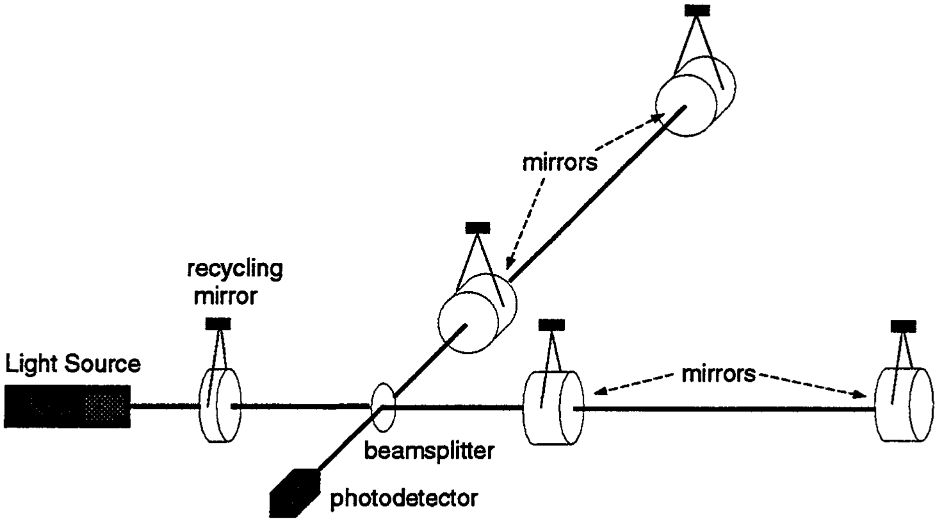

One way to keep the interferometer resonating is to implement some sort of sensing scheme which produces signals corresponding to the deviations from perfect interference, and to use these signals to feed back to the positions of the mirrors and to the laser frequency, in order to cancel any such deviations.

In 1991 S. Whitcomb suggested that the following scheme[7,8,9], illustrated in Figure 1.6, would accomplish this task. The phase of the laser light is modulated at a radio frequency ("RF"), typically on the order of 10 MHz (we will use 12.5 MHz in examples throughout this text). The effect of this modulation is to impose two sidebands on the light, one at 12.5 MHz above the optical "carrier" frequency and one at 12.5 MHz below the carrier. The arm cavity lengths are chosen so that the sidebands do not resonate in the arms, the "in-line" cavity is placed farther from the beam splitter than the "perpendicular" cavity by a distance $l_I - l_P = \delta$, and the "average recycling cavity length" $\frac{l_P+l_I}{2}$ is arranged to be* $\lambda_{mod}/4$ where λ_{mod} is the modulation wavelength $\lambda_{mod} = c/f_{mod}$ (and f_{mod} is the modulation frequency). The effect of these choices of lengths is to allow both the carrier and the sidebands to resonate in the recycling cavity, and to allow sideband light to be transmitted to the antisymmetric port while that port remains dark for the carrier. When the interferometer is distorted by a gravitational wave, some carrier light exits the antisymmetric port, where it beats against the sidebands. This light is detected and demodulated with a mixer (circled "x" in Figure 1.6).

Figure 1.6 Signal extraction scheme.

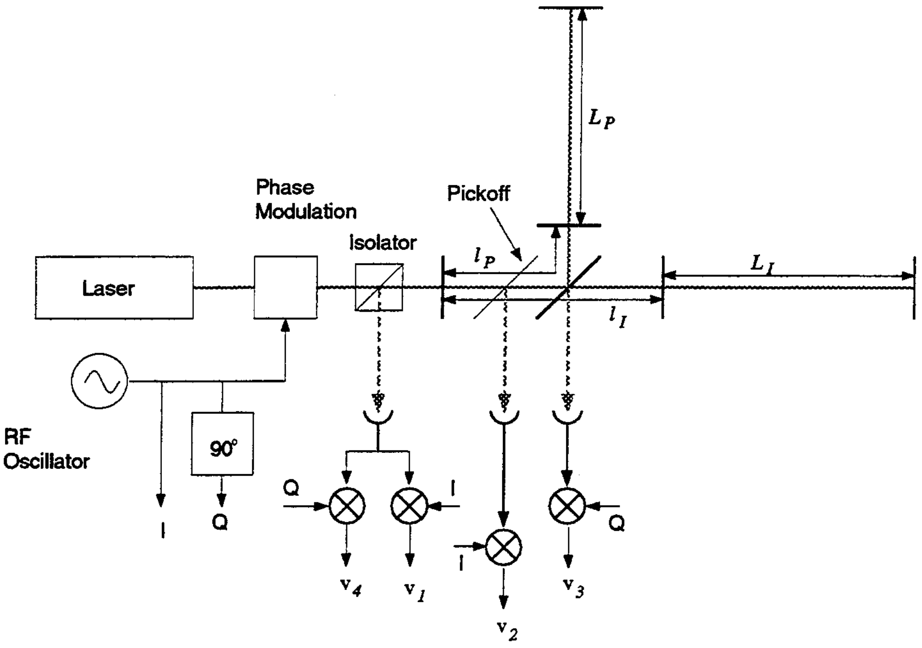

---

[*] An average length of $(n+\frac{1}{2})\frac{\lambda_{mod}}{2}$ for any integral n will work.

The insertion of a pick-off[*] into the recycling cavity and an isolator between the phase modulator and the recycling mirror[†] produces two more optical outputs, each of which can be demodulated using either the inphase modulating signal "I" or the quadrature phase signal "Q", as shown in Figure 1.6. Four of the signals obtained this way[‡] (labelled v_1 through v_4 in Figure 1.6) can then be fed back as shown in Figure 1.7. The inphase signal from the isolator is fed back to the laser frequency. The quadrature phase signal at the isolator is fed back to all four of the arm cavity mirrors in proportion such that l_I and l_P are changed by equal and opposite amounts. The inphase signal from the pick-off is fed back to the recycling mirror, and the quadrature phase signal from the antisymmetric port is fed back in equal and opposite amounts to the two arm cavity back mirrors. Other feedback configurations are also possible; some of these are discussed in Appendix C.

---

[*] This pick-off need not be a separate optical element. From example, the anti-reflection-coated surface of the beam splitter might be usable if it faces the recycling mirror. Even if this surface faces away from the recycling mirror, useful signals are likely to be available in the light reflected at this surface. This latter situation has not been analyzed in detail.

[†] In addition, LIGO will have a passive optical filter, sometimes called a "mode cleaner," installed between the isolator and the recycling mirror. This filter will be transparent to the carrier and the RF sidebands, and its effect is irrelevant for most of the issues addressed here.

[‡] The quadrature phase signal at the pick-off contains the same information as the quadrature phase signal at the isolator, but generally with lower signal-to-noise ratio. There is in addition an optical output available at the other side of the pick-off (since light propagates in both directions in the recycling cavity); this output contains virtually identical signals to the output shown. Some (generally small) improvements in some of the signals are possible by mixing down the signals from all of the optical outputs in both phases and taking appropriate linear combinations.

Figure 1.7 Feedback configuration.

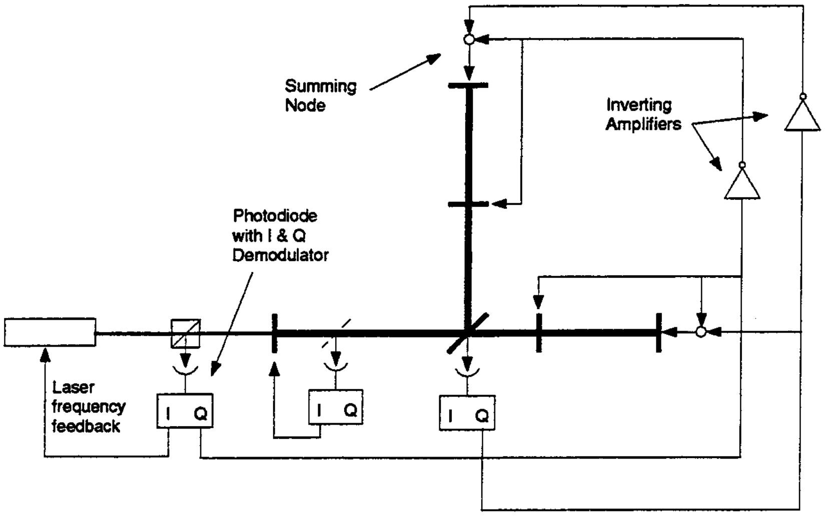

Let us restate in greater detail the problem to be solved. We will concentrate on the problem of keeping the above-mentioned interference conditions satisfied, and show along the way that the configuration described here also meets the requirement of producing a gravitational wave signal. For each interference condition, we must examine the consequence of allowing small errors, so that we can determine the deviations from each condition that can be tolerated without significantly degrading the sensitivity of the detector. This issue is examined in Appendix B; the results are summarized below.

A constraint on the cavity lengths is due to the fact that if the arm cavities deviate from resonance in the same direction, the phase of the light returning to the recycling mirror will change. This would degrade the constructive interference between light reflected there and light entering from the laser. This sets a limit of $6 \times 10^{-13} m$ to the common-mode-displacement of the cavity back mirrors, or equivalently, a limit on the common-mode arm cavity phase*

$$\Phi_+ < 3 \times 10^{-5} \quad (radians) \tag{1.1}$$

Φ_+ is defined as the sum of the arm cavity round-trip phases†:

$$\Phi_+ \equiv \delta\Phi_{I\,0} + \delta\Phi_{P\,0} \tag{1.2}$$

The condition on the phase of light returning to the recycling mirror also constrains the common-mode recycling cavity phase, such that

$$\begin{aligned} \phi_+ &\equiv \delta\phi_{I\,0} + \delta\phi_{P\,0} \\ &< 0.01 \end{aligned} \tag{1.3}$$

(where $\phi_{I\,0} = 2k_0 l_I - 2\phi_{Guoy}$ and $\phi_{P\,0} = 2k_0 l_P - 2\phi_{Guoy}$).

If the arm cavities deviate from resonance in opposite directions, then the destructive interference at the antisymmetric port could be disturbed, allowing excess light to hit the photodetector‡. This sets a condition on the differential

---

[*] We will see that using differential and common-mode combinations of phases is more convenient than using the individual phases themselves.

[†] The round-trip phase is the phase change the light accumulates in travelling twice the length of the cavity, including the Guoy phase, which is a phase deficit due to the fact that the laser beam has a finite diameter. For example $\Phi_{I\,0} = 2k_0 L_I - 2\phi_{Gouy}$, where $k_0 = 2\pi/\lambda_0$ is the wave number of the light. It will generally be more useful for us to work with these round-trip phases than with the distances between adjacent mirrors. We use the subscript 0 to identify quantities related to the carrier; later we will use the subscripts 1 and −1 for the upper and lower RF sidebands.

[‡] Excess light on the photodetector represents an unnecessary loss of light from the interferometer which reduces the optical efficiency and generates additional shot noise.

change in arm cavity phases:

$$\begin{aligned}\Phi_- &\equiv \delta\Phi_{I\,0} - \delta\Phi_{P\,0} \\ &< 5 \times 10^{-4}\end{aligned} \tag{1.4}$$

The requirement above, to keep excess light from the antisymmetric port photodetector, also constrains the differential recycling cavity phase, such that

$$\begin{aligned}\phi_- &\equiv \delta\phi_{I\,0} - \delta\phi_{P\,0} \\ &< 6 \times 10^{-2}\end{aligned} \tag{1.5}$$

In the following chapters we will investigate the behavior of the interferometer output signals in response to motion of the mirrors and changes in the laser frequency. This detailed characterization is necessary for the design and analysis of a control system. There are two parts to this analysis: an analytic approach in which approximations are made and relatively simple expressions describing the interferometer response are derived, and a numerical approach, within which the approximations are less significant and which therefore can be used to test the validity of the approximations made in the analytic derivations. The value of the analytic derivation is that it more clearly expresses how the choice of certain optical parameters in the interferometer (such as mirror reflectivities and positions) affects critical aspects of the behavior of the instrument. For example, we will see that if the asymmetry δ is chosen to be too large, the response of v_2 to ϕ_+ contains a right-half-plane-zero, which compromises control system performance. This sort of conclusion can be derived from numerical models only through a tedious exploration of parameter space and the use of inductive assumptions.

On the other hand, some accuracy has been sacrificed in the derivation of the analytic model. Our goal will be to derive expressions which are accurate to 10% over the range of frequencies in which the servos feeding back to the mirror positions are active. It is for honing these predictions that the numerical models are useful.

The LIGO interferometers are not yet sufficiently well specified to merit a detailed numerical analysis and control system design*. Nonetheless, the exercise of analyzing a possible interferometer and designing a control system for it is useful, and will give insight toward a final design. A set of possible optical parameters for a LIGO interferometer is listed in Table 1.1. We will apply our analytic results and our numerical model to this interferometer to explore its behavior, and then we will design a control system around it, to meet the specifications listed above.

It is virtually certain that neither the optical parameters nor the specifications will remain unchanged between the time of this writing and the time when a LIGO control system is installed, and for this reason we will emphasize more the methods of analysis and design than the details of our numerical example. The numerical model will provide examples of the size of neglected quantities

---

[*] For example, specifications for mirror surface error have not been set and possible trade-offs between cost and quality are still being evaluated.

[†] The arm cavity lengths are displaced slightly from the length where the RF sidebands would be exactly anti-resonant. See also the footnote on p. 27, and Section 7.5.

Table 1.1 Possible optical parameters for a LIGO interferometer.

Quantity		Symbol	Value	Units
Mirror (power) transmissions	Recycling mirror	T_R	5%	
	Arm cavity front mirrors	T_F	3%	
	Arm cavity Back mirrors	T_{BS}	$\mathcal{L}$	
	Beam Splitter	T_{BS}	50%-$\mathcal{L}/2$	
Pick-off reflectivity		R_p	0.1%	
Loss in each optical element		$\mathcal{L}$	100 ppm	
Arm cavity length	In-line cavity	L_I	4002.004†	meters
	Perpendicular cavity	L_P	4001.996	meters
Recycling cavity lengths	recycling mirror to in-line cavity	l_I	6.29	meters
	recycling mirror to perpendicular cavity	l_P	5.71	meters
Laser power		$\|E_l\|^2$	2.6×10^{18}	photons/ second
Modulation index		Γ	0.1	radians
Modulation Frequency		Ω	12.5	MHz

compared to relevant ones, and will give us some idea of the magnitude of the errors introduced by the approximations made within the analytic approach. It is hoped that, as the parameters and specifications of LIGO interferometers become better defined, these same methods will be valuable tools for designing and analyzing control systems, and may even influence the choice of optical parameters and the definition of performance specifications.

Chapter 2 DC Analysis

We begin our analysis of the interferometer by obtaining the derivatives of the voltages v_i with respect to the mirror positions.[‡]

Consider a small region, as shown for example in Figure 2.1, inside one of the laser beam paths within our interferometer.

Figure 2.1 Example of a section of laser beam.

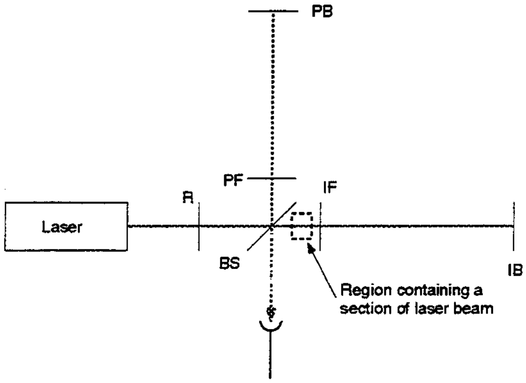

It contains electromagnetic radiation travelling in two directions, which we will call the $+z$ and $-z$ directions, and the electric field due to that radiation can be written:

$$\vec{\mathbf{E}}(z,t) = \vec{p}\sqrt{\frac{2h\nu}{c\epsilon_0}}Re\left\{E_{(+z)}(t)e^{i(2\pi\nu t-kz)} + E_{(-z)}(t)e^{i(2\pi\nu t+kz)}\right\} \qquad (2.1)$$

We will assume uniform linear polarization in the $\vec{p}$ direction. For the remainder of this work, we will concern ourselves exclusively with the complex functions

---

[‡] Expressions similar to the ones in this chapter were first derived by A. Abramovici using a different approach.

of time $E_{(+z)}(t)$ and $E_{(-z)}(t)$, which we will refer to as the *field* traveling in the +z direction and the field traveling in the –z direction, respectively. The factor $\sqrt{\frac{2h\nu}{c\epsilon_0}}$ is used to make the units of the fields $1/\sqrt{\text{second}}$ (the field magnitude squared equals the number of photons per second), which is convenient when calculating shot noise.

The light from the laser is phase modulated at some angular frequency Ω before entering the interferometer. This means that[10] if E_l is the field from the laser and E_{inc} is the field incident on the interferometer,

$$\begin{aligned} E_{inc} &= E_l e^{i\Gamma\cos\Omega t} \\ &\simeq J_0(\Gamma)E_l + iJ_1(\Gamma)E_l e^{i\Omega t} + iJ_1(\Gamma)E_l e^{-i\Omega t} \\ &\equiv E_{inc\,0} + E_{inc\,1}e^{i\Omega t} + E_{inc\,-1}e^{-i\Omega t} \end{aligned} \tag{2.2}$$

we call $E_{inc\,0}$ the *carrier field*, and $E_{inc\,1}$ and $E_{inc\,-1}$ the *upper RF sideband field* and the *lower RF sideband field*, respectively. We will continue to use numeral subscripts to index different frequency components of the light, and literal subscripts to denote location.

In the remainder of this chapter, we will first show how the fields incident on a photodetector affect the corresponding mixer output and how the derivatives of the mixer output are related to the derivatives of those fields. Then we will analyze a simple Fabry-Perot cavity to find the fields and their derivatives within the cavity. Finally we will solve for the fields in the interferometer and their derivatives, and conclude with expressions for the derivatives of the mixer outputs with respect to the phases Φ_+, Φ_-, ϕ_+, and ϕ_-. These are then easily interpreted as the response in the mixer outputs to changes in mirror position or laser frequency.

2.1 Photodetector, Mixer

If we assume that the photodetectors have unit quantum efficiency then the photocurrent in a detector is

$$\begin{aligned} i_p &= |E|^2 \\ &= \left|E_0 + E_1 e^{i\Omega t} + E_{-1} e^{-i\Omega t}\right|^2 \\ &= |E_0|^2 + |E_1|^2 + |E_{-1}|^2 + 2Re\left\{E_1 E_{-1}^* e^{2i\Omega t}\right\} \\ &\qquad + 2Re\left\{\left(E_{-1}^* E_0 + E_0^* E_1\right) e^{i\Omega t}\right\} \end{aligned} \tag{2.3}$$

We assume that the mixers are double-balanced mixers, followed by low-pass or notch filters to eliminate harmonics of the modulation frequency. To a reasonable approximation§, the mixer multiplies its input by $\cos \Omega t$ (or $\sin \Omega t$ if the mixer is fed by the quadrature phase local oscillator signal). By the Fourier shift theorem (or "heterodyne" theorem[11]), the only frequency components of the photocurrent which will pass through the low-pass filter unattenuated are at frequencies near

---

§ The true effect of most mixers is to multiply by something more closely resembling a square wave. This has little effect if the modulation index is small or if the photodiode is tuned, with a resonant filter, to be sensitive only to amplitude modulation at frequencies near the modulation frequency.

Ω. The inphase low-pass filter output then is

$$\begin{aligned} v_I(t) &= \frac{1}{T}\int_{t-T}^{t} 2Re\Big\{\big(E^*_{-1}E_0 + E^*_0 E_1\big)e^{i\Omega t'}\Big\}\cos\Omega t' dt' \\ &= Re\big\{E^*_{-1}E_0 + E^*_0 E_1\big\} \end{aligned} \tag{2.4}$$

where for convenience we have modelled the low pass filter as a device which averages over an integral number of modulation periods $T \equiv \frac{2\pi}{\Omega}$.

Similarly,

$$v_Q(t) = -Im\big\{E^*_{-1}E_0 + E^*_0 E_1\big\} \tag{2.5}$$

Note that for pure phase modulation, for example if $E = E_{inc}$, both outputs vanish: $v_I = v_Q = 0$.

Now we can find the rate of change of these mixer outputs. Suppose E_0, E_1, and E_{-1} are all functions of some parameter θ; then

$$\frac{\partial v_I}{\partial\theta} = Re\left\{\frac{\partial E_0}{\partial\theta}(E_1 + E_{-1})^* + E_0\frac{\partial}{\partial\theta}(E_1 + E_{-1})^*\right\} \tag{2.6}$$

In the special case where $E_1 = E_{-1}$ and both are pure imaginary and their derivatives are real and equal, and E_0 is real and its derivative imaginary, we have

$$\frac{\partial v_I}{\partial\theta} = 2iE_0E_1\left[\frac{1}{(-iE_0)}\frac{\partial E_0}{\partial\theta} - \frac{1}{(-iE_1)}\frac{\partial E_1}{\partial\theta}\right] \tag{2.7}$$

Recognizing $\frac{1}{iE_k}\frac{\partial E_k}{\partial\theta}$ as the rate of change of the phase of E_k, we see that in this special situation $\frac{\partial v_I}{\partial\theta}$ is proportional to the difference between the rate of change of carrier phase and the rate of change of sideband phase.

Similarly

$$\frac{\partial v_Q}{\partial \theta} = Im\left\{\frac{\partial E_0}{\partial \theta}(E_1 - E_{-1})^* + E_0\frac{\partial}{\partial \theta}(E_1 - E_{-1})^*\right\} \tag{2.8}$$

and if E_1 and E_{-1} are equal and pure imaginary, and if E_0 is real, we have

$$\frac{\partial v_Q}{\partial \theta} = E_0 Im\left\{\frac{\partial}{\partial \theta}(E_1 - E_{-1})^*\right\} \tag{2.9}$$

We see that a quadrature phase signal is produced if one sideband grows and the other shrinks.

2.2 Fields in Optical Cavities

Now let us show how the fields are related to the mirror positions.

Figure 2.2 Partially transmitting mirror.

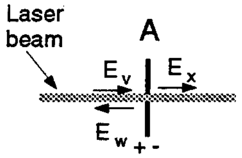

Consider first a partially transmitting mirror A, illuminated from the left, as in Figure 2.2. We define its *reflectivity* r_A (sometimes called "amplitude reflectivity") as the ratio of the reflected field E_w to the incident field E_v. We will always model our mirrors as having positive real reflectivity on one side, and we denote that side with a "+" as shown. We will also model the transmission t_A as being positive and real; then energy conservation requires[12] that we assign negative real reflectivity to the other side of the mirror, denoted by a "-".

Figure 2.3 Fabry-Perot cavity.

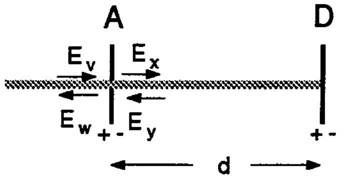

Next, consider the cavity AD, shown in Figure 2.3.

It is easy to find the other fields in terms of E_v:

$$E_x = t_A E_v - r_A E_y \tag{2.10}$$

$$E_y = r_D e^{-i\phi} E_x \tag{2.11}$$

$$E_w = r_A E_v + t_A E_y \tag{2.12}$$

where ϕ is the travel phase corresponding to the optical path from A to D and back: $\phi = 2kd - 2\phi_{Guoy}$. Solving:

$$E_x = \frac{t_A}{1 + r_A r_D e^{-i\phi}} E_v \tag{2.13}$$

$$E_y = \frac{t_A r_D e^{-i\phi}}{1 + r_A r_D e^{-i\phi}} E_v \tag{2.14}$$

$$\begin{aligned} E_w &= \left(r_A + \frac{t_A^2 r_D e^{-i\phi}}{1 + r_A r_D e^{-i\phi}} \right) E_v \\ &= \frac{r_A + \left(r_A^2 + t_A^2\right) r_D e^{-i\phi}}{1 + r_A r_D e^{-i\phi}} E_v \end{aligned} \tag{2.15}$$

To find derivatives, we define

$$z = r_D e^{-i\phi} \tag{2.16}$$

then

$$\frac{d}{dz}\left(\frac{E_x}{E_v}\right) = \frac{-r_A t_A}{(1+r_A z)^2} \tag{2.17}$$

$$\frac{d}{dz}\left(\frac{E_y}{E_v}\right) = \frac{t_A}{(1+r_A z)^2} \tag{2.18}$$

$$\frac{d}{dz}\left(\frac{E_w}{E_v}\right) = \frac{t_A^2}{(1+r_A z)^2} \tag{2.19}$$

As we saw in (2.7), the rate of change of the phase of a field can be a useful quantity; we define

$$\begin{aligned} N &\equiv \frac{E_v}{E_y}\frac{d}{d(-i\phi)}\left(\frac{E_y}{E_v}\right) \\ &= \frac{1}{1+r_A r_D e^{-i\phi}} \end{aligned} \tag{2.20}$$

and

$$\begin{aligned} N' &\equiv \frac{E_v}{E_w}\frac{d}{d(-i\phi)}\left(\frac{E_w}{E_v}\right) \\ &= \frac{t_A^2 r_D e^{-i\phi}}{\left(r_A + \left(r_A^2 + t_A^2\right) r_D e^{-i\phi}\right)\left(1 + r_A r_D e^{-i\phi}\right)} \end{aligned} \tag{2.21}$$

and call these the *bounce number** and *augmented bounce number* respectively. For a resonant cavity, the bounce number is the ratio of the rate at which the phase of the field returning to the front mirror changes when the rear mirror moves, to

---

* The expression "bounce number" is something of a misnomer in this context, since it does not correspond to the number of times any physical quantity "bounces." It derives historically from an analogous quantity for "delay line" gravitational wave detectors.

the rate at which that phase would change if the front mirror were absent. The augmented bounce number is the same ratio except that it is defined for the field E_w reflected from the cavity.

2.3 Fields in the Interferometer

We can use these expressions to solve rather easily for the fields in our interferometer and also for their derivatives. We will first find the carrier fields everywhere, then the sideband fields. Then we will find the derivatives of these fields. Finally we will assemble these into expressions for the derivatives of the mixer outputs.

Figure 2.4 Fields at in-line arm cavity.

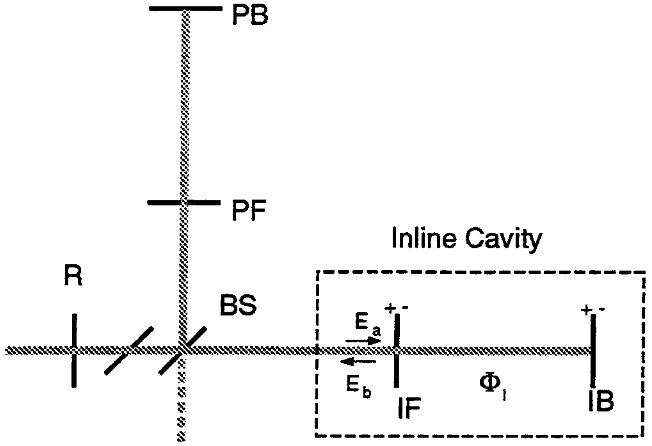

First, consider the carrier fields in an arm cavity, the in-line one for example. Using (2.15), and assuming that the two arm cavities are identical, e.g., $r_{IF} =$

$r_{PF} \equiv r_F$, etc., we have

$$\begin{aligned}\frac{E_b}{E_a} &= r_F + \frac{t_F^2 r_B e^{-i\Phi_I}}{1 + r_F r_B e^{-i\Phi_I}} \\ &\equiv r_c(\Phi_I)\end{aligned} \tag{2.22}$$

where Φ_I is the round-trip phase of the in-line arm cavity, and we have defined r_c as the reflectivity of an arm cavity. We choose the length of the arm cavity so that the carrier resonates in it. This means

$$\Phi_{I\,0} = \pi \qquad \text{(modulo } 2\pi) \tag{2.23}$$

Then from (2.19),

$$\frac{\partial}{\partial \Phi_{I\,0}} \left(\frac{E_{b\,0}}{E_{a\,0}} \right) = \frac{i t_F^2 r_B}{(1 - r_F r_B)^2} \tag{2.24}$$

The arm cavity reflectivity and its derivative will occur so frequently that we assign them special symbols[†]:

$$\begin{aligned} r_{c0} &\equiv -r_c(\pi) \\ &= -r_F + \frac{t_F^2 r_B}{1 - r_F r_B} \end{aligned} \tag{2.25}$$

$$r'_{c0} \equiv \frac{i t_F^2 r_B}{(1 - r_F r_B)^2} \tag{2.26}$$

Next, we include the beam splitter and pick-off, illustrated in Figure 2.5:

For convenience we will assume that the beam splitter, pick-off and recycling mirror (identified by the subscripts "BS," "p" and "R" respectively) are all

---

[†] The sign of r_{c0} is chosen so that this quantity is positive for an over-coupled, resonant cavity.

Figure 2.5 Fields at beam splitter and pick-off.

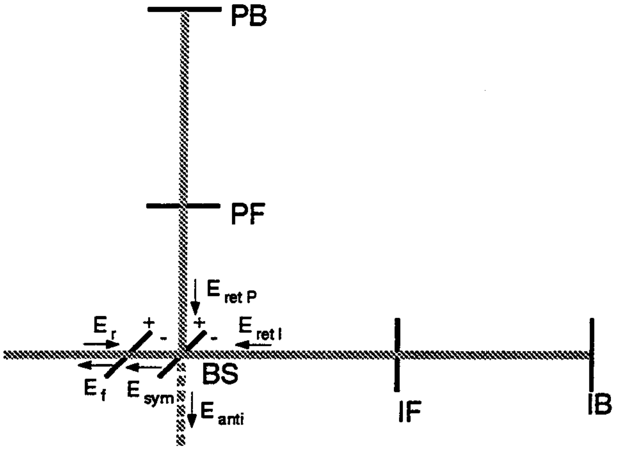

very close together*. The generalization to arbitrary component positions is straight forward, but clutters the formulae. We make the approximation that $r_{BS} = t_{BS} = \frac{1}{\sqrt{2}}$ to get, for the carrier:

$$\frac{E_{ret\ P\ 0}}{E_{r\ 0}} = \frac{t_p}{\sqrt{2}} r_c(\Phi_{P\ 0}) e^{-i\phi_{P\ 0}} \tag{2.27}$$

$$\frac{E_{ret\ I\ 0}}{E_{r\ 0}} = \frac{t_p}{\sqrt{2}} r_c(\Phi_{I\ 0}) e^{-i\phi_{I\ 0}} \tag{2.28}$$

$$\frac{E_{anti\ 0}}{E_{r\ 0}} = \frac{t_p}{2}\left(r_c(\Phi_{P\ 0}) e^{-i\phi_{P\ 0}} - r_c(\Phi_{I\ 0}) e^{-i\phi_{I\ 0}}\right) \tag{2.29}$$

$$\frac{E_{sym\ 0}}{E_{r\ 0}} = \frac{t_p}{2}\left(r_c(\Phi_{I\ 0}) e^{-i\phi_{I\ 0}} + r_c(\Phi_{P\ 0}) e^{-i\phi_{P\ 0}}\right) \tag{2.30}$$

$$\frac{E_{f\ 0}}{E_{r\ 0}} = \frac{T_p}{2}\left(r_c(\Phi_{I\ 0}) e^{-i\phi_{I\ 0}} + r_c(\Phi_{P\ 0}) e^{-i\phi_{P\ 0}}\right) \tag{2.31}$$

---

* Here "very close together" means separated by distances small compared to λ_{mod}.

where, in the final equation, we have written T_p for t_p^2, using the convention that upper case R's and T's equal the squares of the corresponding lower case quantities. Taking

$$\Phi_{I\,0} = \Phi_{P\,0} = \pi \tag{2.32}$$

we have

$$\frac{E_{f\,0}}{E_{r\,0}} = \frac{-T_p}{2} r_{c0} \left(e^{-i\phi_{I\,0}} + e^{-i\phi_{P\,0}} \right) \tag{2.33}$$

In this last equation we have the ratio between the light to the right of the recycling mirror travelling away from the recycling mirror, and the light returning to the recycling mirror. Another way to think of this (shown in Figure 2.6) is that all of the mirrors of Figure 2.5 form a compound back mirror for the cavity having the recycling mirror as its front mirror.

Figure 2.6 Compound mirror.

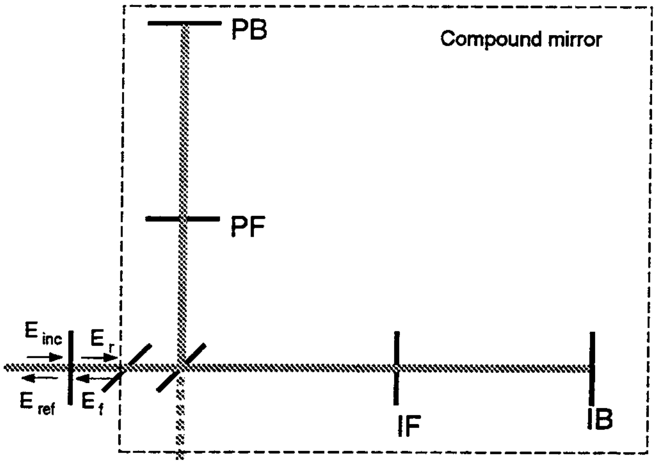

Using (2.13) we have

$$\frac{E_{r\,0}}{E_{inc\,0}} = \frac{t_R}{1 - r_R T_p r_{c0} \frac{1}{2}\left(e^{-i\phi_{I\,0}} + e^{-i\phi_{P\,0}}\right)} \tag{2.34}$$

and to achieve maximum power buildup in the recycling cavity,[†] we need to arrange for the second term in the denominator to be as nearly as possible equal -1. Hence we choose

$$\phi_{I\,0} = \phi_{P\,0} = 0 \tag{2.35}$$

so that

$$\frac{E_{r\,0}}{E_{inc\,0}} = \frac{t_R}{1 - r_R T_p r_{c0}} \tag{2.36}$$

Using (2.14) and (2.15)

$$\frac{E_{f\,0}}{E_{inc\,0}} = \frac{-t_R T_p r_{c0}}{1 - r_R T_p r_{c0}} \tag{2.37}$$

$$\begin{aligned} \frac{E_{ref\,0}}{E_{inc\,0}} &= r_R - \frac{t_R^2 T_p r_{c0}}{1 - r_R T_p r_{c0}} \\ &\simeq \frac{r_R - T_p r_{c0}}{1 - r_R T_p r_{c0}} \end{aligned} \tag{2.38}$$

where the last expression was derived using the approximation that losses in the recycling mirror can be neglected[‡]: $r_R^2 + t_R^2 \simeq 1$.

[†] The ratio $\left|\frac{E_{r\,0}}{E_{inc\,0}}\right|^2$ is called the *recycling gain* or the *recycling factor* and is a measure of the benefit delivered by the recycling mirror.

[‡] Losses of a few tens of parts per million are anticipated in the recycling mirror, whereas the total round-trip loss in the recycling cavity is expected to be a few percent.

Since $E_f = E_{sym} t_p$,

$$\frac{E_{sym\,0}}{E_{inc\,0}} = \frac{-t_R t_p r_{c0}}{1 - r_R T_p r_{c0}} \tag{2.39}$$

and from (2.29)

$$E_{anti\,0} = 0 \tag{2.40}$$

Now we turn to the sideband fields in an arm cavity. We begin with the upper sideband; the derivation for the lower sideband is almost identical. The arm cavity length is chosen so that the sidebands are almost exactly antiresonant[§], i.e. $\Phi_{I\,1} \simeq 0$. Referring back to Fig. 2.4,

$$\begin{aligned} r_{c1} &\equiv \frac{E_{b\,1}}{E_{a\,1}} \\ &= r_F + \frac{t_F^2 r_B}{1 + r_F r_B} \end{aligned} \tag{2.41}$$

and

$$\begin{aligned} r'_{c1} &\equiv \frac{\partial}{\partial \Phi_{I\,1}} \frac{E_{b\,1}}{E_{a\,1}} \\ &= \frac{-i t_F^2 r_B}{(1 + r_F r_B)^2} \end{aligned} \tag{2.42}$$

Because the sidebands are nearly perfectly excluded from the arm cavities, we can approximate the expressions above as being unity and zero, respectively (in our numerical example, their values are 0.99995 and 0.008).

[§] If they were exactly antiresonant then the RF sidebands at $2n\Omega$ would all be resonant, causing the interferometer response to be very sensitive to arm cavity length and modulation depth. See also Section 7.5.

Figure 2.7 Equivalent optical configuration for the analysis of sideband fields.

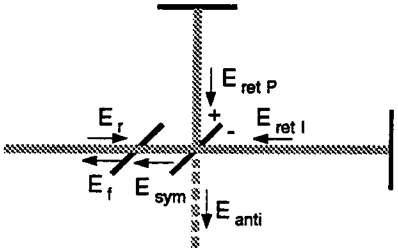

Accordingly, Figure 2.7 shows the interferometer with the arm cavities replaced by mirrors with unit reflectivity. Then

$$\frac{E_{ret\,I\,1}}{E_{r\,1}} = \frac{t_p}{\sqrt{2}} e^{-i\phi_{I\,1}} \tag{2.43}$$

$$\frac{E_{ret\,P\,1}}{E_{r\,1}} = \frac{t_p}{\sqrt{2}} e^{-i\phi_{P\,1}} \tag{2.44}$$

$$\frac{E_{f\,1}}{E_{r\,1}} = \frac{T_p}{2}\left(e^{-i\phi_{I\,1}} + e^{-i\phi_{P\,1}}\right) \tag{2.45}$$

$$\frac{E_{anti\,1}}{E_{r\,1}} = \frac{t_p}{2}\left(e^{-i\phi_{P\,1}} - e^{-i\phi_{I\,1}}\right) \tag{2.46}$$

We have stated already that the average distance between the beam splitter and the arm cavity front mirrors is[‖] $\frac{\lambda_{mod}}{4}$; because of the asymmetry it is $\frac{\lambda_{mod}}{4} + \frac{\delta}{2}$

[‖] See footnote, p. 7, and Section 7.5.

for the in-line arm and $\frac{\lambda_{mod}}{4} - \frac{\delta}{2}$ for the perpendicular arm. Then

$$\begin{aligned} \phi_{I\,1} &= 2\frac{2\pi\nu + \Omega}{c}\left(\frac{\lambda_{mod}}{4} + \frac{\delta}{2}\right) \\ &= \phi_{I\,0} + \frac{2\Omega}{c}\left(\frac{\lambda_{mod}}{4} + \frac{\delta}{2}\right) \\ &= \pi + \alpha \end{aligned} \tag{2.47}$$

where $\alpha \equiv \frac{\Omega\delta}{c}$.

In similar fashion one can show that $\phi_{P\,1} = \pi - \alpha$. It then follows that

$$\frac{E_{sym\,1}}{E_{r\,1}} = -t_p \cos\alpha \tag{2.48}$$

$$\frac{E_{anti\,1}}{E_{r\,1}} = -it_p \sin\alpha \tag{2.49}$$

Similarly

$$\frac{E_{sym\,-1}}{E_{r\,-1}} = -t_p \cos\alpha \tag{2.50}$$

$$\frac{E_{anti\,-1}}{E_{r\,-1}} = it_p \sin\alpha \tag{2.51}$$

Finally, as we did for the carrier, we find the sideband fields everywhere by considering the pick-off and everything to its right as a compound mirror (shown in Figure 2.8). The difference 2α between $\phi_{I\,1}$ and $\phi_{P\,1}$ affects the transmission (to the antisymmetric port) of this mirror. The average of $\phi_{I\,1}$ and $\phi_{P\,1}$ determines whether the cavity formed by the compound mirror and the recycling mirror is resonant.

From (2.13) through (2.15):

$$\frac{E_{r\,1}}{E_{inc\,1}} = \frac{t_R}{1 - r_R T_p \cos\alpha} \tag{2.52}$$

Figure 2.8 Compound mirror for the RF sidebands.

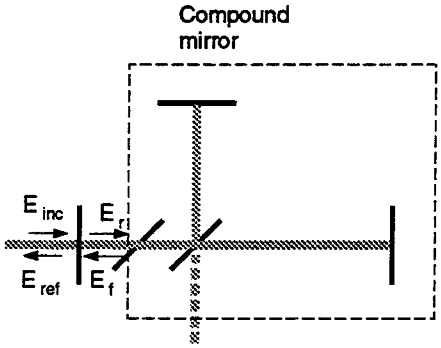

$$\frac{E_{f\,1}}{E_{inc\,1}} = \frac{-t_R T_p \cos\alpha}{1 - r_R T_p \cos\alpha} \tag{2.53}$$

$$\frac{E_{sym\,1}}{E_{inc\,1}} = \frac{-t_R t_p \cos\alpha}{1 - r_R T_p \cos\alpha} \tag{2.54}$$

$$\begin{aligned}\frac{E_{ref\,1}}{E_{inc\,1}} &= r_R - \frac{t_R^2 T_p \cos\alpha}{1 - r_R T_p \cos\alpha} \\ &\simeq \frac{r_R - T_p \cos\alpha}{1 - r_R T_p \cos\alpha}\end{aligned} \tag{2.55}$$

(the approximate equality above holds when we neglect losses in the recycling mirror) and using (2.49) and (2.52)

$$\frac{E_{anti\,1}}{E_{inc\,1}} = \frac{-it_R t_p \sin\alpha}{1 - r_R T_p \cos\alpha} \tag{2.56}$$

Let us summarize this in words. For the carrier and for the sidebands, the field is amplified in the recycling cavity because the circulating field interferes constructively with the incoming field. For the sidebands, the amplification is mainly limited by the transmission to the antisymmetric port, whereas for the carrier it is limited principally by loss in the arm cavities.

2.4 Derivatives of Mixer Outputs

Now we can differentiate the fields and find the derivatives of mixer outputs. We will consider first the differential signals: the derivatives of the gravitational wave output v_3 and the isolator quadrature output v_4 with respect to phase changes Φ_- and ϕ_-. Then we will calculate the common-mode signals: the derivatives of the pick-off and isolator inphase outputs v_1 and v_2 with respect to Φ_+ and ϕ_+.

First we note that since

$$\begin{aligned} \delta\Phi_{I\,0} &= \frac{1}{2}(\Phi_+ + \Phi_-) \\ \delta\Phi_{P\,0} &= \frac{1}{2}(\Phi_+ - \Phi_-) \end{aligned} \tag{2.57}$$

we have

$$\begin{aligned} \frac{\partial}{\partial\Phi_-} &= \frac{\partial\Phi_{I\,0}}{\partial\Phi_-}\frac{\partial}{\partial\Phi_{I\,0}} + \frac{\partial\Phi_{P\,0}}{\partial\Phi_-}\frac{\partial}{\partial\Phi_{P\,0}} \\ &= \frac{1}{2}\left(\frac{\partial}{\partial\Phi_{I\,0}} - \frac{\partial}{\partial\Phi_{P\,0}}\right) \end{aligned} \tag{2.58}$$

and that for Ω constant and $\Omega \ll \nu$

$$\begin{aligned} \phi_{I\,1} &= 2l_I\left(\frac{2\pi\nu}{c} + \frac{\Omega}{c}\right) - 2\phi_{Guoy} \\ &= \phi_{I\,0} + 2l_I\frac{\Omega}{c} \end{aligned} \tag{2.59}$$

so that

$$\frac{\partial\phi_{I\,1}}{\partial\phi_{I\,0}} \simeq 1 \tag{2.60}$$

whether the independent variable is ν or l_I.

Differential Signals

We begin with the gravitational wave signal. Differentiating (2.29)

$$\begin{aligned} \frac{\partial E_{anti\ 0}}{\partial \Phi_-} &= \frac{\partial E_{anti\ 0}}{\partial \Phi_{I\ 0}} \frac{\partial \Phi_{I\ 0}}{\partial \Phi_-} + \frac{\partial E_{anti\ 0}}{\partial \Phi_{P\ 0}} \frac{\partial \Phi_{P\ 0}}{\partial \Phi_-} \\ &= -\frac{1}{2} E_{r\ 0} t_p r'_{c0} \end{aligned} \tag{2.61}$$

and, using (2.8), we have (at the antisymmetric port)

$$\begin{aligned} \frac{\partial v_3}{\partial \Phi_-} &= Im\left\{ \frac{\partial E_{anti\ 0}}{\partial \Phi_-} (E_{anti\ 1} - E_{anti\ -1})^* \right\} \\ &= -E_l^2 J_0(\Gamma) J_1(\Gamma) t_p \left(\frac{E_{r\ 0}}{E_{inc\ 0}} \right) \left| \left(\frac{E_{anti\ 1}}{E_{inc\ 1}} \right) \right| |r'_{c0}| \end{aligned} \tag{2.62}$$

which can be further expanded using (2.49) and (2.51). Equation (2.62) can be understood as follows. When Φ_- deviates from 0 we cease to have perfect destructive interference at the antisymmetric port for the carrier. The size of this deviation from perfect destructive interference is proportional to the rate $|r'_{c0}|$ at which the carrier field returning to the beam splitter from the arm cavities changes with Φ_-. This carrier light then beats against the sidebands which are present because of the asymmetry, producing modulation of the photocurrent at Ω, and a signal at the mixer output.

A similar mechanism is responsible for the sensitivity to ϕ_- at the antisymmetric port. When ϕ_- deviates from 0 we also cease to have perfect destructive interference at the antisymmetric port for the carrier. Quantitatively, to find $\frac{\partial v_3}{\partial \phi_-}$, again differentiate (2.29)

$$\frac{\partial v_3}{\partial \phi_-} = E_l^2 J_0(\Gamma) J_1(\Gamma) \left(\frac{E_{r\,0}}{E_{inc\,0}} \right) \left(\frac{E_{anti\,1}}{E_{inc\,1}} \right) t_p r_{c0} \tag{2.63}$$

We now move on to $\frac{\partial v_4}{\partial \phi_-}$. From (2.45) the reflectivity of the compound mirror for the upper sideband is $-T_p \cos(\alpha + \phi_-/2)$; using (2.19) with $z = -T_p \cos(\alpha + \phi_-/2)$ we have

$$\frac{\partial}{\partial \phi_-} \left(\frac{E_{ref\,1}}{E_{inc\,1}} \right) = \frac{t_R^2 T_p \sin \alpha}{2(1 - r_R T_p \cos \alpha)^2} \tag{2.64}$$

Similarly,

$$\frac{\partial}{\partial \phi_-} \left(\frac{E_{ref\,-1}}{E_{inc\,-1}} \right) = \frac{-t_R^2 T_p \sin \alpha}{2(1 - r_R T_p \cos \alpha)^2} \tag{2.65}$$

Since the conditions leading to (2.9) are satisfied, we have

$$\frac{\partial v_4}{\partial \phi_-} = -E_l^2 J_0(\Gamma) J_1(\Gamma) \frac{E_{ref\,0}}{E_{inc\,0}} \frac{t_R^2 T_p \sin \alpha}{(1 - r_R T_p \cos \alpha)^2} \tag{2.66}$$

which can be further expanded using (2.38).

In words, this sensitivity in v_4 to ϕ_- is due to the fact that when ϕ_- changes, the reflectivity of the compound mirror increases for one RF sideband and decreases for the other. This causes a corresponding change in the relative size of the sidebands reflected from the recycling mirror and a signal according to (2.9).

There is also a small dependence in v_4 on Φ_-. Because the derivative (2.42) of the arm cavity reflectivity for the sideband is not exactly 0, it is non-negligible when it is responsible for the only contribution to the signal. We re-insert $r_c(\Phi_{I\,1})$ and $r_c(\Phi_{P\,1})$ into (2.45) and differentiate to get (using (2.9))

$$\frac{\partial v_4}{\partial \Phi_-} = \left|r'_{c1}\right| E_l^2 J_0(\Gamma) J_1(\Gamma) \frac{E_{ref\,0}}{E_{inc\,0}} \frac{t_R^2 T_p \sin\alpha}{\left(1 - r_R T_p \cos\alpha\right)^2} \tag{2.67}$$

Common-mode Signals

Now let us look at the common-mode signals. We begin with v_2, the inphase pick-off signal. Using (2.31) and (2.18) with

$$z = \frac{E_{f\,0}}{E_{r\,0}} \tag{2.68}$$

to find $\frac{\partial}{\partial \Phi_+}\left(\frac{E_{f\,0}}{E_{inc\,0}}\right)$ we have:

$$\frac{\partial}{\partial \Phi_+}\left(\frac{E_{sym\,0}}{E_{inc\,0}}\right) = \frac{t_R t_p r'_{c0}}{2\left(1 - r_R T_p r_{c0}\right)^2} \tag{2.69}$$

Then, using (2.7), we obtain

$$\frac{\partial v_2}{\partial \Phi_+} = E_l^2 J_0(\Gamma) J_1(\Gamma) R_p \left(\frac{E_{sym\,0}}{E_{inc\,0}}\right)\left(\frac{E_{sym\,1}}{E_{inc\,1}}\right) N_0 \frac{|r'_{c0}|}{r_{c0}} \tag{2.70}$$

which can be further expanded using (2.25), (2.26), (2.39) and (2.54), and where

$$\begin{aligned} N_0 &= \left|\frac{1}{E_{sym\,0}} \frac{\partial E_{sym\,0}}{\partial \phi_+}\right| \\ &= \left|\frac{1}{\frac{E_{sym\,0}}{E_{inc\,0}}} \frac{\partial}{\partial \phi_+}\left(\frac{E_{sym\,0}}{E_{inc\,0}}\right)\right| \\ &= \frac{1}{1 - r_R T_p r_{c0}} \end{aligned} \tag{2.71}$$

is the bounce number for the carrier in the recycling cavity. In words: When Φ_+ changes, the phase of the carrier light changes in proportion to the factors $\frac{|r'_{c0}|}{r_{c0}}$

(which is just the augmented bounce number for the carrier in an arm cavity) and N_0, generating a signal according to (2.7).

When ϕ_+ changes, the phases of the carrier and of the sidebands all change, so that by (2.7) the signal is proportional to the difference in the rates of change of these phases. To find $\frac{\partial v_2}{\partial \phi_+}$ we have, using (2.31) and (2.45),

$$z = -e^{-i\phi_+/2} T_p r_{c0} \tag{2.72}$$

for the carrier and

$$z = -e^{-i\phi_+/2} T_p \cos\alpha \tag{2.73}$$

for the sidebands; then using (2.18) and (2.7), we have

$$\frac{\partial v_2}{\partial \phi_+} = E_l^2 J_0(\Gamma) J_1(\Gamma) R_p \frac{E_{sym\,0}}{E_{inc\,0}} \frac{E_{sym\,1}}{E_{inc\,1}} [N_0 - N_1] \tag{2.74}$$

where

$$N_1 = \frac{1}{1 - r_R T_p \cos\alpha} \tag{2.75}$$

N_0 and N_1 are the bounce number for the carrier and upper sideband (respectively) in the recycling cavity. The bounce number for the lower sideband equals the bounce number for the upper sideband.

We now move on to v_1, the inphase signal at the isolator. This signal is produced by the same mechanism as $\frac{\partial v_2}{\partial \Phi_+}$ except that the rate of change of carrier phase is proportional to N_0' instead of N_0. $\frac{\partial v_1}{\partial \Phi_+}$ is found using (2.31), (2.21), (2.19), and (2.7):

$$\frac{\partial}{\partial\Phi_+}\left(\frac{E_{ref\,0}}{E_{inc\,0}}\right) = \frac{t_R^2 T_p r'_{c0}}{2(1 - r_R T_p r_{c0})^2} \tag{2.76}$$

$$\frac{\partial v_1}{\partial\Phi_+} = E_l^2 J_0(\Gamma) J_1(\Gamma) \left(\frac{E_{ref\,0}}{E_{inc\,0}}\right)\left(\frac{E_{ref\,1}}{E_{inc\,1}}\right) N'_0 \frac{|r'_{c0}|}{r_{c0}} \tag{2.77}$$

To find $\frac{\partial v_1}{\partial\phi_+}$ we use (2.31), (2.19), (2.45), and (2.7):

$$\frac{\partial v_1}{\partial\phi_+} = E_l^2 J_0(\Gamma) J_1(\Gamma) \left(\frac{E_{ref\,0}}{E_{inc\,0}}\right)\left(\frac{E_{ref\,1}}{E_{inc\,1}}\right) [N'_0 - N'_1] \tag{2.78}$$

Here the mechanism is the same as the one for $\frac{\partial v_2}{\partial\phi_+}$, except that again, augmented bounce numbers are used. With the approximation that the recycling mirror is lossless, we can write

$$\begin{aligned} N'_0 &= \frac{1}{-iE_{ref\,0}} \frac{\partial E_{ref\,0}}{\partial\phi_+} \\ &= \frac{-t_R^2 T_p r_{c0}}{(r_R - T_p r_{c0})(1 - r_R T_p r_{c0})} \end{aligned} \tag{2.79}$$

and

$$\begin{aligned} N'_1 &= \frac{1}{-iE_{ref\,1}} \frac{\partial E_{ref\,1}}{\partial\phi_+} \\ &= \frac{-t_R^2 T_p \cos\alpha}{(r_R - T_p\cos\alpha)(1 - r_R T_p \cos\alpha)} \end{aligned} \tag{2.80}$$

Both (2.77) and (2.78) can be expanded using (2.38) and (2.55).

This completes our analysis of the signals of interest. One can show that the remaining eight derivatives all vanish. Table 2.1 shows the factors which vanish to make (2.6) vanish, and Table 2.3 shows the factors which cause (2.8) to vanish.

Table 2.1 Vanishing terms in equation (2.6) for derivatives of v_1 and v_2 with respect to the differential degrees of freedom.

		Output	
		v_1	v_2
Derivative with respect to:	Φ_-	$\frac{\partial E_0}{\partial \Phi_-} = 0$ $\frac{\partial}{\partial \Phi_-}(E_1 + E_{-1})^* = 0$	$\frac{\partial E_0}{\partial \Phi_-} = 0$ $\frac{\partial}{\partial \Phi_-}(E_1 + E_{-1})^* = 0$
	ϕ_-	$\frac{\partial E_0}{\partial \phi_-} = 0$ $\frac{\partial}{\partial \phi_-}(E_1 + E_{-1})^* = 0$	$\frac{\partial E_0}{\partial \phi_-} = 0$ $\frac{\partial}{\partial \phi_-}(E_1 + E_{-1})^* = 0$

Table 2.2 Vanishing terms in equation (2.8) for derivatives of v_3 and v_4 with respect to the differential degrees of freedom.

		Output	
		v_3	v_4
Derivative with respect to:	Φ_+	$E_0 = 0$ $\frac{\partial E_0}{\partial \Phi_+} = 0$	$E_1 - E_{-1} =$ $0 \frac{\partial}{\partial \Phi_+}(E_1 - E_{-1}) = 0$
	ϕ_+	$E_0 = 0$ $\frac{\partial E_0}{\partial \phi_+} = 0$	$E_1 - E_{-1} =$ $0 \frac{\partial}{\partial \phi_+}(E_1 - E_{-1}) = 0$

Finally we consider the effect of a change in the laser frequency. Since, for example,

$$\begin{aligned} \Phi_{I\,0} &= 2kL_I + 2\phi_{Guoy} \\ &= \frac{4\pi\nu}{c} L_I + 2\phi_{Guoy} \end{aligned} \tag{2.81}$$

changes in this phase can be effected either by a change in the length of the in-line arm cavity or by a change in the laser frequency. Now

$$\frac{\partial \Phi_+}{\partial \nu} = \frac{8\pi L}{c} \tag{2.82}$$

and

$$\frac{\partial \phi_+}{\partial \nu} = \frac{8\pi l}{c} \tag{2.83}$$

so that, for example

$$\begin{aligned} \frac{\partial v_1}{\partial \nu} &= \frac{\partial v_1}{\partial \Phi_+}\frac{\partial \Phi_+}{\partial \nu} + \frac{\partial v_1}{\partial \phi_+}\frac{\partial \phi_+}{\partial \nu} \\ &= \frac{8\pi}{c}\left(L\frac{\partial v_1}{\partial \Phi_+} + l\frac{\partial v_1}{\partial \phi_+}\right) \\ &\simeq \frac{8\pi L}{c}\frac{\partial v_1}{\partial \Phi_+} \end{aligned} \tag{2.84}$$

where we can make the approximation in the last line because $l \ll L$ and because $\frac{\partial v_1}{\partial \phi_+} \ll \frac{\partial v_1}{\partial \Phi_+}$. Similarly, we will use

$$\frac{\partial v_2}{\partial \nu} \simeq \frac{8\pi L}{c}\frac{\partial v_2}{\partial \Phi_+} \tag{2.85}$$

which is a very good approximation for the same reasons.

In chapter 4 we will compare, for our numerical example, the values of the derivatives found using this analysis and the values found by a numerical model which makes fewer approximations.

It is easy to generalize the analysis above, of the response to particular combinations of mirror displacements, to the case of arbitrary combinations. We simply note that the following combinations of mirror displacements and changes in laser frequency produce no signal at all. They are in the kernel of the Jacobian of interferometer outputs with respect to mirror position and optical frequency.

1. Displacement of the entire interferometer towards (or away from) the laser.
2. Displacement of the arm cavities towards the beam splitter and displacement of the recycling mirror away from the beam splitter, all by equal amounts.
3. A change $\Delta\nu$ in the laser frequency, together with displacements of the arm cavity input mirrors PF and IF away from the recycling mirror, through distances $l_P\frac{\Delta\nu}{\nu}$ and $l_I\frac{\Delta\nu}{\nu}$, and displacements of the arm cavity back mirrors PB and IB through distances of $(L_P + l_P)\frac{\Delta\nu}{\nu}$ and $(L_I + l_I)\frac{\Delta\nu}{\nu}$ respectively.

These three combinations have the property that they leave the relative phases of any interfering beams unchanged.

From this observation we can conclude, for example, that a displacement of the recycling mirror towards the beam splitter will generate the same signals as an equal-sized displacement of all of the arm cavity mirrors towards the beam splitter, since the two differ by an element (#2 above) of the kernel. Similarly, displacement of the beam splitter and of the recycling mirror, such that l_I and l_P change by equal and opposite amounts, differs only by an element of the kernel from a displacement of the two arm cavities in opposite directions in the same amounts, and the two combinations must produce the same signal.

Chapter 3 Interferometer Frequency Response

Implicit in the analysis of the last chapter, since we did not allow any of the fields E_0, E_1, or E_{-1} to depend on time, is the assumption that changes in the phases Φ and ϕ occur slowly. Suppose instead that we want to know what the response in the output signals is when the laser frequency changes abruptly, or when a mirror vibrates at a high frequency. This is the problem we will analyze here.

3.1 Fabry-Perot Cavity

As in Chapter 2 we will begin by analyzing a single cavity in some detail, and then extending the results to the complete interferometer. The response of a Fabry-Perot cavity to back mirror motion has been understood for some time[13,14], but we will re-derive it because our method will include the RF phase modulation in a natural way and will be easily generalized to more complex optical systems. Our cavity, shown in Figure 3.1, consists of two mirrors A and D, separated by a distance d such that the carrier resonates in the cavity but the two RF sidebands do not.

Figure 3.1 Fabry-Perot cavity.

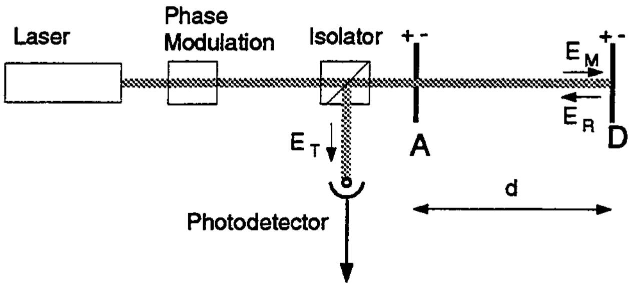

If both mirrors are stationary, then as in (2.2), the field at the back mirror essentially consists of three frequencies:

$$E_M = E_{M\,0} + E_{M\,1}e^{i\Omega t} + E_{M\,-1}e^{-i\Omega t} \tag{3.1}$$

Now suppose the back mirror is shaking with small amplitude at a frequency ω ($\omega \ll \Omega$), i.e.,

$$\begin{aligned} x_D(t) &= Re\{Xe^{i\omega t}\} && |X| \ll \lambda \\ &= X\cos\omega t && \text{for} \quad X \epsilon \Re \end{aligned} \tag{3.2}$$

This motion modulates the optical path within the cavity so that

$$\begin{aligned} E_R &= r_D E_M e^{i2kX\cos\omega t} \\ &\simeq r_D E_M\left(1 + ikXe^{i\omega t} + ikXe^{-i\omega t}\right) \end{aligned} \tag{3.3}$$

Clearly if E_M contains three frequencies

$$E_M = E_{M\,0} + E_{M\,1}e^{i\Omega t} + E_{M\,-1}e^{-i\Omega t} \tag{3.4}$$

then E_R contains nine:

$$E_R = r_D[ikXE_{M\,-1}e^{-i(\Omega+\omega)t} + E_{M\,-1}e^{-i\Omega t} + ikXE_{M\,-1}e^{-i(\Omega-\omega)t}$$

$$+ikXE_{M\,0}e^{-i\omega t} + E_{M\,0} + ikXE_{M\,0}e^{i\omega t}$$

$$+ikXE_{M\,1}e^{i(\Omega-\omega)t} + E_{M\,1}e^{i\Omega t} + ikXE_{M\,1}e^{i(\Omega+\omega)t}] \qquad (3.5)$$

We will call the additional six frequencies "audio sidebands" imposed on the original three "RF frequencies" (the carrier and its two RF sidebands), and we will identify them with an additional index. Using this notation, we write:

$$\begin{aligned} E_R &= E_{R\,-1\,-1}e^{-i(\Omega+\omega)t} + \cdots + E_{R\,1\,1}e^{i(\Omega+\omega)t} \\ &= \sum_{u=-1}^{1}\sum_{v=-1}^{1} E_{Ruv}e^{i(u\Omega+v\omega)t} \end{aligned} \qquad (3.6)$$

In the summation above, u indexes RF frequency and v indexes audio sidebands. To avoid ambiguities between the use of the "-" to indicate a negative index and a subtraction, we will enclose any operation in parentheses; for example if $u = 0$ we would write $E_{(u-1)}$ for E_{-1}.

Now suppose the field E_M incident on the moving mirror contains nine frequencies instead of only three (which in general it will, since mirror A reflects E_R back to mirror D). Then by (3.3) E_R is a product of a factor (E_M) containing nine terms and a factor $\left(1 + ikXe^{i\omega t} + ikXe^{-i\omega t}\right)$ of three terms, so E_R has 27 terms (at 15 distinct frequencies). However, 12 of these terms are of order $(kX)^2$ and we neglect them. The remaining 15 terms (at nine frequencies) are:

$$E_R = r_D\left[\sum_{u=-1}^{1}\left(E_{Muo}e^{iu\Omega t} + \sum_{v=-1,1}(E_{Muv} + ikXE_{Muo})e^{i(u\Omega+v\omega)t}\right)\right] \qquad (3.7)$$

Evidently the shaking of the mirror causes, for example, an amount

$$S_{0\,1} \equiv r_D ikX E_{M\,0\,0} \tag{3.8}$$

to be added to the incident $E_{M\,0\,1}$ field upon reflection (and corresponding quantities to be added to the other audio sideband fields). The moving mirror acts as a source of this frequency component of the light. As in (2.10) — (2.15) we can solve for the field at this frequency everywhere. At the two mirrors, we have:

$$E_{M\,0\,1} = -r_A e^{-i\phi_{0\,1}} E_{R\,0\,1} \tag{3.9}$$

$$E_{R\,0\,1} = r_D E_{M\,0\,1} + S_{0\,1} \tag{3.10}$$

Solving:

$$E_{R\,0\,1} = \frac{1}{1 + r_A r_D e^{-i\phi_{0\,1}}} S_{0\,1} \tag{3.11}$$

$$E_{T\,0\,1} = \frac{t_A e^{-i\phi_{0\,1}/2}}{1 + r_A r_D e^{-i\phi_{0\,1}}} S_{0\,1} \tag{3.12}$$

if the carrier is resonant in the cavity,

$$\phi_{0\,0} = \pi \qquad (\text{modulo } 2\pi) \tag{3.13}$$

$$\begin{aligned}\phi_{0\,1} &= \frac{2\pi\nu+\omega}{c}2d \\ &= \phi_{0\,0}+\omega\tau \qquad \text{where } \tau=\frac{2d}{c}\end{aligned} \tag{3.14}$$

$$e^{-i\phi_{0\,1}} = -e^{-i\omega\tau} \tag{3.15}$$

$$e^{-i\phi_{0\,1}/2} = -ie^{-i\omega\tau/2} \tag{3.16}$$

Then

$$E_{T0\,1} = \frac{-it_A e^{-i\omega\tau/2}}{1-r_A r_D e^{-i\omega\tau}} S_{0\,1} \tag{3.17}$$

We call the ratio of the audio sideband field at the photodetector to the source $S_{0\,1}$ of that field the *transmission function* $K_{0\,1}$ from the shaking mirror to the optical output and write

$$E_{T0\,1} = K_{0\,1} S_{0\,1} \tag{3.18}$$

We find for the lower audio sideband on the carrier

$$E_{T0\,-1} = \frac{-it_A e^{i\omega\tau/2}}{1-r_A r_D e^{i\omega\tau}} S_{0\,-1} \tag{3.19}$$

Similar expressions can be found for the other audio sidebands.

Given full information about the spectral content of E_T we still need to know the mixer output when this light is present at the photodetector. As before, the photodetector output is

$$
\begin{aligned}
i_p(t) &= |E_T|^2 \\
&= \left| \sum_{u=-1}^{1} \sum_{v=-1}^{1} E_{T\,uv} e^{i(u\Omega + v\omega)t} \right|^2
\end{aligned}
\tag{3.20}
$$

Again, as in (2.3), this contains terms at a number of frequencies, of which only those near Ω will be mixed down to near DC and pass through the low-pass filter. Moreover, of those frequencies, we are only interested in the ones at frequencies of $\Omega + \omega$ and $\Omega - \omega$ because these will be mixed down to ω, and it is the response in the mixer output at ω that we want*. These terms are

$$
\begin{aligned}
i_{p\ at\ \Omega\mp\omega} = 2Re\{ \sum_{u=-1}^{0} \sum_{v=-1}^{0} (&E^*_{T\ u\ v} E_{T\ (u+1)\ (v+1)} e^{i(\Omega+\omega)t} \\
&+ E^*_{T\ u\ (v+1)} E_{T\ (u+1)\ v} e^{i(\Omega-\omega)t})\}
\end{aligned}
\tag{3.21}
$$

Then

$$
\begin{aligned}
v_I(t) &= \frac{1}{T} \int_{t-T}^{t} i_{p\ at\ \Omega\mp\omega}(t') \cos \Omega t' dt' \\
&= Re\left\{ \left[\sum_{u=-1}^{0} \sum_{v=-1}^{0} (E^*_{T\ u\ v} E_{T\ (u+1)\ (v+1)} + E_{T\ u\ (v+1)} E^*_{T\ (u+1)\ v}) \right] e^{i\omega t} \right\}
\end{aligned}
\tag{3.22}
$$

which is in the form

$$
v_I(t) = Re\{ V_I e^{i\omega t} \}
\tag{3.23}
$$

---

* The only other component passed by the lowpass filter is at DC, corresponding to (2.4) and (2.5). We are usually interested in the response to small motions around the point of perfect resonance, where this term vanishes.

with

$$V_I \equiv \sum_{u=-1}^{0} \sum_{v=-1}^{0} (E^*_{T\ u\ v} E_{T\ (u+1)\ (v+1)} + E_{T\ u\ (v+1)} E^*_{T\ (u+1)\ v}) \tag{3.24}$$

so that $|V_I|$ is the size of the response and $\arg(V_I)$ is its phase.

Hence we define the transfer function from mirror position to inphase mixer output

$$H_{v_I x_D} = \frac{V_I}{X} \tag{3.25}$$

which is a function of frequency. By a similar argument, we can show that

$$V_Q = \sum_{u=-1}^{0} \sum_{v=-1}^{0} \left(E^*_{T\ u\ v} E_{T\ (u+1)\ (v+1)} - E_{T\ u\ (v+1)} E^*_{T\ (u+1)\ v} \right) \tag{3.26}$$

In principle, this completes our analysis of the frequency response. For a given amplitude and frequency of mirror motion we know how to find the spectral content of the light on the photodetector and we know how to find the mixer output given that spectral content. This algorithm is well suited to numerical implementation and is in fact the one used in the program described in Chapter 4.

Let us examine the expressions for V_I and V_Q more carefully. Each term in these expressions is the product of an RF field which is independent of the shaking frequency ω and either an upper audio sideband field or the complex conjugate of a lower audio sideband field. Each audio sideband field is proportional to the transmission function from the shaking mirror to the optical output or to a sum of transmission functions if several mirrors are shaking or if the shaking mirror is illuminated from both sides. In any event, the transfer functions from X to V_I and V_Q are linear combinations of transmission functions and complex conjugates of transmission functions.

It is often the case that a few reasonable approximations can reduce these linear combinations to a very simple form. In our analysis of the interferometer we will see that the transmission functions for the audio sidebands on the RF sidebands are all frequency independent, and that the complex conjugate of each transmission function for the lower audio sideband on the carrier differs at most by a constant from the corresponding transmission function for the upper audio sideband on the carrier. From these two facts we can state immediately that

$$V_I = C + FK_{0\,1}(\omega) \tag{3.27}$$

for some constants C and F (and a similar expression for V_Q). The constants C and F can usually be found from the DC model of Chapter 2; the transmission function $K_{0\,1}$ will need to be derived separately.

For the simple cavity being analyzed here we assume that the RF sidebands are essentially absent from inside the cavity so that the sources of audio sidebands on the RF sidebands are negligible:

$$S_{-1\,-1}, S_{-1\,1}, S_{1\,-1}, S_{1\,1} \simeq 0 \tag{3.28}$$

This means that the corresponding four terms in V_I vanish, and

$$V_I = \left(E^*_{T\,-1\,0} + E^*_{T\,1\,0}\right)E_{T\,0\,1} + \left(E_{T\,-1\,0} + E_{T\,1\,0}\right)E^*_{T\,0\,-1} \tag{3.29}$$

We also restrict our analysis to frequencies much smaller than the cavity free spectral range:

$$\omega\tau \ll 1 \tag{3.30}$$

So that (3.17) becomes (by neglecting the exponential in the numerator[†] and Taylor expanding the one in the denominator):

$$\begin{aligned} E_{T0\,1} &= \frac{-it_A e^{-i\omega\tau/2}}{1 - r_A r_D e^{-i\omega\tau}} S_{0\,1} \\ &\simeq \frac{-it_A}{1 - r_A r_D} \frac{1}{1 + \frac{i\omega}{\omega_{cav}}} S_{0\,1} \end{aligned} \tag{3.31}$$

where $\omega_{cav} = \frac{1 - r_A r_D}{r_A r_D \tau}$.

For the lower audio sideband on the carrier,

$$E^*_{T0\,-1} \simeq \frac{it_A}{1 - r_A r_D} \frac{1}{1 + \frac{i\omega}{\omega_{cav}}} S^*_{0\,-1} \tag{3.32}$$

since $E_{M\,0\,0}$ is pure imaginary,

$$S^*_{0\,-1} = -ir_D kX E^*_{M\,0\,0} = ir_D kX E_{M\,0\,0} = S_{0\,1} \tag{3.33}$$

[†] The exponential in the numerator only produces a small phase change in the frequency range of interest.

so $E^*_{T0\,-1} = -E_{T0\,1}$ and, using (3.29)

$$V_I = -\frac{4r_D t_A k X E_{M\,0\,0} E_{T\,1\,0}}{1 - r_A r_D} \frac{1}{1 + \frac{i\omega}{\omega_{cav}}} \tag{3.34}$$

For compatibility with notation used in references on control systems, we may let $s = i\omega$ and write

$$V_I = H_{v_I x_D}(s) X \tag{3.35}$$

where

$$H_{v_I x_D}(s) = H_{v_I x_D\,DC} \frac{1}{1 + \frac{s}{\omega_{cav}}} \tag{3.36}$$

and

$$\begin{aligned} H_{v_I x_D\,DC} &= \frac{\partial V_I}{\partial x_D} \\ &= -\frac{4r_D t_A k X E_{M\,0\,0} E_{T\,1\,0}}{1 - r_A r_D} \end{aligned} \tag{3.37}$$

What if we were to shake the front mirror instead of the back mirror? We could use the same method to answer this question, adding an additional source for each of the audio sidebands (since they would now be produced at both surfaces of the front mirror). This is in fact the approach taken in the program. In our analytic derivation, however, this becomes quite tedious since we can no longer neglect the audio sidebands on the RF sidebands, and since, for each audio sideband on the carrier, there are different transmission functions from each of the two sources to the photodetector.

Instead we use a simple thought-experiment to argue that if the carrier is resonant, the response to motion of the two mirrors must be the same in amplitude (and opposite in phase except for a factor which is negligible for frequencies small compared to $1/\tau$). Suppose we shake both mirrors with the same amplitude and in the same direction and with a relative phase such that motion of the front mirror lags motion of the back mirror by a time delay of $\tau/2$. Now if the back mirror, mirror D, is moving with a certain velocity when a particular bit of light reflects from it, then all of the frequency components in that piece of light will be Doppler shifted to new frequencies, only to be shifted back to their original frequencies when the bit of light reflects from mirror A, after travelling the length of the cavity, which takes a time $\tau/2$. The light travelling towards the back mirror then has no audio phase modulation because it is a combination of fresh light from outside the cavity and light which has been modulated by reflection from the back mirror and un-modulated by reflection from the front mirror. The light inside the cavity travelling towards the front mirror then has a total phase modulation corresponding to one reflection from a moving mirror, as does the light reflected from the outside of the front mirror. All of the RF frequency components of the light returning to the photodetector then have the same audio phase modulation, that amount corresponding to one reflection from a moving mirror:

$$E_T = \left(E_{T\,0\,0} + E_{T\,1\,0}e^{i\Omega t} + E_{T\,-1\,0}e^{-i\Omega t}\right)\left(1 + ikXe^{i\omega t} + ikXe^{-i\omega t}\right) \quad (3.38)$$

which produces no signal at the mixer output. Since the mixer output is linear in (small) mirror motions, and since this combination of mirror motions produces no output, either motion by itself must produce the opposite signal as that which the other motion by itself would produce.

Finally we want to show that the response to laser frequency modulation is the same as the response to motion of the back mirror; we will show that for frequencies small compared to $1/\tau$,

$$H_{v_I\,\delta\nu} = \frac{d}{\nu} H_{v_I\,X} \tag{3.39}$$

The argument is the following:

Modulating the laser such that $\nu(t) = \nu_{DC} + \delta\nu\cos\omega t$, for example by changing the length of the laser cavity, is equivalent to modulating the laser phase:

$$E_l(t) = E_{l\,DC}e^{i\theta\sin\omega t} \tag{3.40}$$

with

$$\theta = \frac{2\pi}{\omega}\delta\nu \tag{3.41}$$

and we have already seen that the latter will impose audio sidebands on the light. Now the field E_T on the photodetector as before will contain nine frequency components. The audio sidebands on the RF sidebands will be frequency independent, whereas the audio sidebands on the carrier will have some frequency dependence.

$$\begin{aligned} E_{T\,01} &= \left[r_A + \frac{r_D t_A^2 e^{-i\phi_{01}}}{1 + r_A r_D e^{-i\phi_{01}}} \right] S_{01} \\ &\simeq r_A S_{01} - \frac{r_D t_A^2}{1 - r_A r_D} \frac{1}{1 + \frac{i\omega}{w_{cav}}} S_{01} \end{aligned} \tag{3.42}$$

where $S_{01} \propto \theta$ is again the source of audio sidebands (in this case they originate in the laser).

Because of this, some of the terms in the expression for V_I will be frequency independent, and some will have a $1/\left(1 + \frac{i\omega}{w_{cav}}\right)$ frequency dependence:

$$V_I = \left(C + F \frac{1}{1 + \frac{i\omega}{w_{cav}}} \right) \theta \tag{3.43}$$

Now $F = -C$, because in the limit $\omega \rightarrow 0$ the response in V_I to finite $\delta\nu$ is finite (see for example (2.82)); hence the response to finite θ vanishes.

$$\begin{aligned} V_I &= C \left(1 - \frac{1}{1 + \frac{i\omega}{w_{cav}}} \right) \theta \\ &= \frac{2\pi C}{\omega_{cav}} \frac{1}{1 + \frac{i\omega}{w_{cav}}} \delta\nu \end{aligned} \tag{3.44}$$

We know (as in (2.81–2.85)) what the low frequency limit of this response is:

$$\begin{aligned} \frac{\partial v_I}{\partial \nu} &= \frac{4\pi d}{c} \frac{\partial v_I}{\partial \phi} \\ &= \frac{4\pi d}{c} \frac{1}{2k} \frac{\partial v_I}{\partial x} \\ &= \frac{d}{\nu} \frac{\partial v_I}{\partial x} \end{aligned} \tag{3.45}$$

Substituting, we get:

$$H_{v_I\,\delta\nu} = \frac{d}{\nu} H_{v_I\,X} \tag{3.46}$$

3.2 Response of the Complete Interferometer

At this point we are ready to compute the frequency response corresponding to the derivatives we found in Chapter 2. We will proceed in roughly the same order as we did there, finding first the response, as a function of frequency, in the gravitational wave output v_3 and in v_4, the isolator quadrature phase output, to Φ_- and ϕ_-. These responses are relatively simple because for each of them either the audio sidebands on the carrier or the audio sidebands on the RF sidebands can be ignored. Moreover, we will argue that the transmission function for the audio sidebands on the RF sidebands is frequency independent; this further simplifies two of the transfer functions.

Next we will analyze the response in the common-mode outputs v_1 and v_2 to Φ_+ and ϕ_+. The responses to ϕ_+ are the most complex ones we will encounter. In these responses, all of the audio sidebands contribute significantly to the signal.

Throughout our analysis of frequency response, we will restrict our attention to frequencies much smaller than the free spectral range of an arm cavity:

$$\omega\tau_{arm} \ll 1 \tag{3.47}$$

(where $\tau_{arm} \equiv \frac{2L_I}{c} \simeq \frac{2L_P}{c}$). This allows us to make a number of simplifying approximations, and moreover gives us all of the information we need to design any of the servo loops which will feed back to a force on a mirror, since all of these loops are constrained to have unity-gain frequencies much smaller than the arm cavity free spectral range, due to internal resonances in the mirrors. The loop which feeds back to the laser frequency can have a bandwidth approaching or even exceeding the arm cavity free spectral range; here our analysis is of little help. For this one loop we rely on a numerical model (see Chapter 4) to verify that the interferometer transfer function is sufficiently well behaved to permit us to implement a stable controller.

Differential Signals

We begin our characterization of the interferometer with the signal in which we would observe gravitational waves. Suppose the mirrors IB and PB are shaking at frequency ω with opposite phase. Each will be a source of audio sidebands on the carrier and these sidebands will propagate out to the beam splitter. At the beam splitter, they will interfere almost perfectly destructively on the symmetric side and almost perfectly constructively on the antisymmetric side. The reason that the interference is not perfect is that one pair has had to travel a distance δ farther than the other. For an asymmetry of 57 cm and an audio sideband wavelength of $\lambda_{audio} = 30\ km$ (corresponding to a shaking frequency of 10kHz), a fraction $\sin^2\left(\frac{2\delta}{\lambda_{audio}}\right) \simeq 1.4 \times 10^{-9}$ of the audio sideband power is diverted from the antisymmetric port to the symmetric port. We will ignore this effect.

Again we ignore the effect of the arm cavity back mirrors on the RF sidebands. Then each term in V_3 is proportional to the transmission function from the sources of audio sidebands (at the back mirrors) to the antisymmetric port:

$$H_{v_3\Phi_-} = H_{v_3\Phi_-DC}\frac{1}{1+\frac{s}{\omega_c}} \tag{3.48}$$

where

$$\omega_c \equiv \frac{1-r_F r_B}{r_F r_B \tau_{arm}} \tag{3.49}$$

The response at this output to ϕ_- is essentially frequency independent. To see this we imagine shaking both mirrors of the in-line arm cavity in the same phase, and at the same time shaking both mirrors of the perpendicular arm cavity in the opposite phase. As we saw in the argument leading to (3.38), this produces frequency-independent audio phase modulation of the light returning from each cavity. The phase of the corresponding (frequency independent) audio sidebands in the light returning from the in-line cavity are opposite in phase from the audio sidebands in the light returning from the perpendicular arm cavity, and all of this audio sideband light exits the interferometer at the antisymmetric port. Thus[‡]

$$H_{v_3\phi_-} = H_{v_3\phi_-DC} \tag{3.50}$$

Now let us consider the response in v_4, the isolator quadrature phase output, to Φ_- and ϕ_-. First we note that the audio sidebands on the carrier produced by changes in Φ_- and ϕ_- interfere destructively on the symmetric side of the beam splitter and therefore are absent at the isolator.

[‡] The audio sidebands on the RF sidebands do not contribute to this signal since $E_{anti\ 0\ 0} = 0$

For the response to ϕ_-, we consider the compound mirror of Figure 2.8 as the source of audio sidebands on the RF sidebands. For the cavity in which these audio sidebands resonate (consisting of the recycling mirror and the compound back mirror),

$$\omega_{rec} = \frac{1 - r_R T_p \cos\alpha}{(r_R T_p \cos\alpha)\tau_{rec}} \qquad \text{with } \tau_{\text{rec}} = \frac{l_I + l_P}{c} \tag{3.51}$$
$$\simeq 800\ kHz$$

in our numerical example. This is far outside of the frequency range of interest and we approximate

$$\frac{1}{1 + \frac{s}{\omega_{rec}}} \simeq 1 \tag{3.52}$$

to get

$$H_{v_4\phi_-} = H_{v_4\phi_- DC} \tag{3.53}$$

For the response to Φ_-, as in (2.66), the source is the small audio sidebands put on the RF sidebands by motion of the arm cavity back mirrors. We repeat the steps leading up to (3.17), using $\phi_{1\,0} \simeq 0 \quad (\text{modulo } 2\pi)$ for an RF sideband in an arm cavity, to get

$$E_{T1\,1} = \frac{t_F e^{-i\omega\tau_{arm}/2}}{1 + r_F r_B e^{-i\omega\tau_{arm}}} S_{1\,1} \tag{3.54}$$

which is essentially constant in the frequency range of interest. The same thing is true for the remaining audio sidebands on RF sidebands, and we conclude that the response is frequency independent:

$$H_{v_4\Phi_-} = H_{v_4\Phi_- DC} \tag{3.55}$$

Common-mode Signals

Next we turn to the response to Φ_+, which corresponds to common mode changes of arm cavity length. When the arm cavity back mirrors shake in phase, the audio sidebands on the carrier interfere constructively at the symmetric side of the beam splitter. Because the carrier audio sideband light coming from the two arm cavities has the same amplitude and phase and because any of this light reflected back towards the cavities will be treated in the same way by the two arm cavities, we can[15], for the purpose of calculating the response to this type of mirror motion, replace the beam splitter and arm cavities with a single arm cavity, as shown in Figure 3.2.

Figure 3.2 Equivalent system for the purpose of deriving common-mode response.

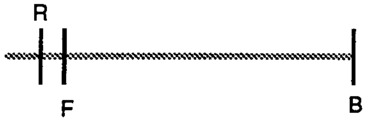

The mirrors R and F form a compound mirror[§16,17] with (using (2.15)) reflectivity from the right of

$$r_{F*R} = \frac{r_F + \left(r_F^2 + t_F^2\right) T_p r_R}{1 + r_F r_R T_p} \tag{3.56}$$

[§] Implicit in this simplifying substitution is the assumption that the reflectivity of the compound mirror is frequency independent. This is in fact a very good approximation. Letting $\phi_0 = \omega\tau_{rec}$ (with $\tau_{rec} = \frac{2l}{c}$ in (2.16), (2.21) gives roughly $\frac{t_F^2}{4}\tau_{rec}$ as the rate of change of phase of the reflectivity with ω. This is exceedingly small compared to τ_{arm}, which is the rate of change of round-trip phase due to the length of the arm cavity.

so that

$$H_{v_1\Phi_+}(s) = H_{v_1\Phi_+DC}\frac{1}{1+\frac{s}{\omega_{cc}}} \tag{3.57}$$

where

$$\omega_{cc} \equiv \frac{1 - r_{F*R}r_B}{r_{F*R}r_B\tau_{arm}} \tag{3.58}$$

Noting that

$$E_{ref\,0\,1} = E_{sym\,0\,1}t_Rt_p \tag{3.59}$$

$$E_{ref\,0\,-1} = E_{sym\,0\,-1}t_Rt_p \tag{3.60}$$

we have immediately

$$H_{v_2\Phi_+}(s) = H_{v_2\Phi_+DC}\frac{1}{1+\frac{s}{\omega_{cc}}} \tag{3.61}$$

It is useful to write our expression for ω_{cc}, in terms of individual mirror parameters, in a more compact form. We write

$$\begin{aligned} r_F &= \sqrt{1 - T_F - \mathcal{L}_F} \\ &\simeq 1 - \frac{T_F}{2} - \frac{\mathcal{L}_F}{2} \end{aligned} \tag{3.62}$$

where $\mathcal{L}_F \equiv 1 - R_F - T_F$ is the loss in mirror F, and

$$T_p = 1 - R_p - \mathcal{L}_p \tag{3.63}$$

$$r_R \simeq 1 - \frac{T_R}{2} - \frac{\mathcal{L}_R}{2} \tag{3.64}$$

to get

$$\begin{aligned} r_{F*R} &\simeq \frac{\left(1-\frac{T_F}{2}-\frac{\mathcal{L}_F}{2}\right)+(1-\mathcal{L}_F)(1-R_p-\mathcal{L}_p)\left(1-\frac{T_R}{2}-\frac{\mathcal{L}_R}{2}\right)}{1+\left(1-\frac{T_F}{2}-\frac{\mathcal{L}_F}{2}\right)\left(1-\frac{T_R}{2}-\frac{\mathcal{L}_R}{2}\right)(1-R_p-\mathcal{L}_p)} \\ &\simeq 1-\frac{1}{2}\left[\mathcal{L}_F+\frac{T_FT_R}{4}+\frac{R_pT_F}{2}\right] \end{aligned} \tag{3.65}$$

and*

$$\omega_{cc}=\frac{1}{2\tau_{arm}}\left(\frac{T_FT_R}{4}+\frac{R_pT_F}{2}+\mathcal{L}_F+\mathcal{L}_B+T_B\right) \tag{3.66}$$

Unlike our previous expression for ω_{cc}, the evaluation of this expression does not require subtracting nearly equal numbers.

The transfer functions from ϕ_+, changes in which correspond to displacement of all four arm cavity mirrors towards (or away from) the beam splitter, are the most complex of the ones we will analyze. As we saw in the analysis leading to (2.74), the low-frequency response in the inphase pick-off signal v_2 is due to the fact that when the recycling cavity length changes, the carrier phase changes in proportion to N_0 and the sideband phases change in proportion to N_1, so that a signal is produced according to (2.7). To generalize this result to the case of mirror motion at arbitrary frequencies, we first use the audio sideband picture to explain the same result. At very low frequencies (where the two models overlap), the resultant phasor formed when the carrier (or one of the RF sidebands) and its two audio sidebands are summed is a phasor slowly rotating back and forth at

---

* The set of terms in parentheses represents the set of "leaks" through which carrier light is able to escape from the system. If the laser were abruptly shut off, it would take the field about 1/10 of a second to decay to 1/e of its initial amplitude; in fact this step response represents an alternate way of calculating the frequency response to certain inputs.

the shaking frequency. The frequency-dependent analog of the statement above involving phases changing at different rates is the remark that the audio sidebands on the RF sidebands beat against the carrier, producing a signal which partially cancels the signal produced when the audio sidebands on the carrier beat against the RF sidebands.

Now we see that as the shaking frequency increases, the contribution to the signal from the audio sidebands on the RF sidebands will be constant (as in (3.52)) whereas the contribution due to the audio sidebands on the carrier may have some frequency dependence proportional to the transmission functions $K_{0\,1}$ and $K^*_{0\,-1}$. Anticipating that $K^*_{0\,-1} = K_{0\,1}$ we write

$$H_{v_2\dot{\phi}_+}(i\omega) = H_{v_2\dot{\phi}_+DC}\frac{N_1 - \frac{K_{01}(\omega)}{K_{01}(0)}N_0}{N_1 - N_0} \tag{3.67}$$

Let us find $K_{0\,1}$. We consider the arm cavities and beam splitter as the compound back mirror and source of audio sidebands for the cavity having the recycling mirror and pickoff as its compound front mirror. The reflectivity of this back mirror is frequency dependent. Using (2.15) with $\Phi_{0\,1}(\omega) = \pi + \omega\tau_{arm}$ we get

$$\begin{aligned} r_c(\pi + \omega\tau_{arm}) &= r_F - \frac{t_F^2 r_B}{1 - r_F r_B(1 - i\omega\tau_{arm})} \\ &= -r_{c0}\left(\frac{1 - \frac{r_F}{r_{c0}}\frac{i\omega}{\omega_c}}{1 + \frac{i\omega}{\omega_c}}\right) \end{aligned} \tag{3.68}$$

Now according to (3.11) and (3.14) with $\phi_{00} = 0$ and* $\omega\tau_{rec} \ll 1$ we have

$$\begin{aligned} E_{sym\,0\,1} &= \frac{1}{1 + r_R T_p r_c(\pi + \omega\tau_{arm})} S_{0\,1} \\ &= \frac{1}{1 - r_R T_p r_{c0}} \frac{1 + \frac{i\omega}{\omega_c}}{1 + \frac{i\omega}{\omega_{cc}}} S_{0\,1} \end{aligned} \tag{3.69}$$

where we have used† $\omega_{cc} = \frac{1 - r_R T_p r_{c0}}{1 + r_R T_p r_F}\omega_c$. To find $K_{0\,-1}$, we repeat the above, using $-\omega$ instead of ω. and conclude that $K^*_{0\,-1} = K_{0\,1}$. Substituting into (3.67), we get

$$H_{v_2\dot{\phi}_+}(s) = H_{v_2\dot{\phi}_+DC}\left(\frac{1 + s\left(\frac{N_1}{N_1 - N_0}\frac{1}{\omega_{cc}} - \frac{N_0}{N_1 - N_0}\frac{1}{\omega_c}\right)}{1 + \frac{s}{\omega_{cc}}}\right) \tag{3.70}$$

Neglecting $\frac{N_0}{N_1 - N_0}\frac{1}{\omega_c}$ next to $\frac{N_1}{N_1 - N_0}\frac{1}{\omega_{cc}}$ we have

$$H_{v_2\dot{\phi}_+}(s) = H_{v_2\dot{\phi}_+DC}\frac{1 + \frac{s}{\frac{N_1 - N_0}{N_1}\omega_{cc}}}{1 + \frac{s}{\omega_{cc}}} \tag{3.71}$$

To derive the response in v_1 to ϕ_+, we use exactly the same argument, substituting augmented bounce numbers N'_0 and N'_1 for the bounce numbers N_0 and N_1, to get:

$$\begin{aligned} H_{v_1\dot{\phi}_+}(s) &= H_{v_1\dot{\phi}_+DC}\frac{1 + i\omega\left(\frac{N'_1}{N'_1 - N'_0}\frac{1}{\omega_{cc}} - \frac{N'_0}{N'_1 - N'_0}\frac{1}{\omega_c}\right)}{1 + \frac{i\omega}{\omega_{cc}}} \\ &\simeq H_{v_1\dot{\phi}_+DC}\frac{1 + \frac{s}{\frac{N'_1 - N'_0}{N'_1}\omega_{cc}}}{1 + \frac{s}{\omega_{cc}}} \end{aligned} \tag{3.72}$$

---

* More relevant here is the fact that $\arg\left(e^{-i\omega\tau_{rec}}\right) \ll \arg\left(-r_c(\pi + \omega\tau_{arm})\right)$

† This can be shown to be equal to our previous expression for ω_{cc} by simplifying as we did in (3.65).

where the approximate equivalence again is derived by neglecting $\frac{N_0'}{N_1'-N_0'}\frac{1}{\omega_c}$ next to $\frac{N_1'}{N_1'-N_0'}\frac{1}{\omega_{cc}}$.

Finally, since we intend to feed back to the recycling mirror, we need to understand the response to recycling mirror motion*. We define $H_{v_i\theta_+}$ to be the set of transfer functions from recycling mirror displacement ($\theta_+ = 4k(\delta x_R)$) to the mixer outputs. We can see immediately that

$$H_{v_i\theta_+} = H_{v_i\phi_+} \tag{3.73}$$

by an argument similar to the one advanced in Section 3.1. There we found that for a Fabry-Perot cavity, the effect of motion of the front mirror differs only by a phase from the effect of back mirror motion. If we shake the recycling mirror, the arm cavity front mirrors, and the arm cavity back mirrors all at the same frequency and in the same phase, then again, to a good approximation† we impose an equal audio phase modulation on each RF frequency, generating no signal. This means that motion of the recycling mirror by itself produces a signal equal and opposite‡ to the signal produced by motion of the other four mirrors.

---

* Together with the response to beam splitter motion of Appendix C, this will complete the analysis of the dynamic response of the interferometer.

† This result is exact if the mirror motions are not exactly in phase, but instead the arm cavity front mirrors lead the recycling mirror by the time it takes light to travel across their respective separations, and the arm cavity back mirrors lead the front mirrors by the time it takes light to travel the length of an arm cavity.

‡ This sign difference does not appear in equation (3.73) because we use the opposite direction of motion for the recycling mirror to define θ_+.

In the next chapter we will compare plots of the frequency response calculated according to our simplified analysis above to plots of the response calculated by a purely numerical model, which makes fewer approximations.

Chapter 4 Numerical Models

Two numerical models have been developed for the purpose of analyzing the optical system.

The first one, the "numerical DC model" calculates the same derivatives that we found in Chapter 2[§]. Written in Mathematica, it finds symbolic expressions for all of the relevant fields in the interferometer. It then differentiates them as required to find the symbolic derivatives of the mixer outputs with respect to the phases. Because Mathematica does not make the approximations we did, the expressions for these derivatives are quite long, typically filling several pages. Into these expressions the program substitutes numerical values for mirror reflectivities and phases, to generate a table of derivatives. The same program is of course also able to find values for the fields at the outputs; these numbers are useful for shot noise calculations.

The second model, called "Twiddle," calculates the frequency response of the interferometer. To understand how it works, we consider the simple Fabry-Perot cavity, fed by a source of light of unit magnitude.

The equations for this system may be written

$$E_a = 1 \tag{4.1}$$

[§] A model which calculated the mixer output signals instead of their derivatives was written in 1991 by S. Whitcomb. The model discussed here was adapted from that earlier model.

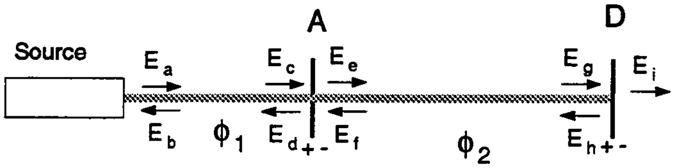

$$E_e = t_A E_c + r_A E_f \tag{4.2}$$

$$E_d = t_A E_f - r_A E_c \tag{4.3}$$

$$E_c = E_a e^{-i\phi_1} \tag{4.4}$$

$$E_b = E_d e^{-i\phi_1} \tag{4.5}$$

$$E_h = r_B E_g \tag{4.6}$$

$$E_i = t_B E_g \tag{4.7}$$

$$E_g = E_e e^{-i\phi_2} \tag{4.8}$$

$$E_f = E_h e^{-i\phi_2} \tag{4.9}$$

There is one equation for the source, a pair of equations for the front mirror, a pair of equations for the space between the source and the front mirror, and so on. These can also be written in matrix form:

$$M \begin{bmatrix} E_a \\ E_b \\ \vdots \\ E_i \end{bmatrix} = \begin{bmatrix} 1 \\ 0 \\ \vdots \\ 0 \end{bmatrix} \tag{4.10}$$

and solved by matrix inversion. The Twiddle program constructs the matrix M from a set of commands specifying mirror properties and separations. For example, a set of commands for constructing the cavity above is:

```
s1 = source[gamma]

m1 = mirror[r1,t1]

connect[s1,1,m1,1,length1]

m2 = endmirror[r2,t2]

connect[m1,2,m2,1,length2]
```

Each command above corresponds to one group of equations from (4.1) to (4.9).

In addition to these commands, the program needs to be given a matrix containing the propagation phase, for the carrier and for each RF sideband, for each connection defined. The program then calculates the propagation phases for the audio sidebands from the lengths of the connections. When calculating the audio sideband fields, the equations are slightly different because the source of this light is in a different location. If the back mirror is shaking, then it is the source of audio sidebands; equation (4.1) becomes

$$E_a = 0 \tag{4.11}$$

and equation (4.6) becomes

$$E_h = r_B E_g + S \tag{4.12}$$

where S is proportional to the amplitude of the mirror motion and the RF field E_g found in the previous step. Thus to find the audio sideband, the program inverts the same matrix (which however contains different values of ϕ_1 and ϕ_2 since the frequency is different) and multiplies it with a different source vector to solve for the fields:

$$M \begin{bmatrix} E_a \\ E_b \\ \vdots \\ E_i \end{bmatrix} = \begin{bmatrix} 0 \\ \vdots \\ S \\ 0 \end{bmatrix} \tag{4.13}$$

In summary, *Twiddle* begins by constructing the matrix M from a set of commands specifying mirror positions, reflectivities and transmissions, and a matrix giving the propagation phase for each frequency. It inverts this matrix and multiplies by the appropriate source vector to find the RF fields everywhere. Next it forms the source vectors for the audio sidebands from the RF fields incident on the mirror being shaken. Finally, for each frequency of interest, it inserts the appropriate propagation phase into the matrix M and solves for the audio sideband fields everywhere. From the values of all of these fields it calculates the mixer output using[||] (3.24) or (3.26).

As mentioned earlier, the numerical models have the advantage of being more precise than the analyses of Chapters 2 and 3. Both numerical models include the effects of loss in the recycling mirror and beam splitter and neither neglects the RF sideband fields in the arm cavities. The numerical frequency response model is not limited to frequencies much smaller than the free spectral range of the arm cavities and is believed to be accurate up to a significant fraction of the modulation frequency.

It is instructive to see how the calculations compare. Table 4.1 shows the values of the derivatives calculated in Chapter 2, evaluated numerically using the parameters of Table 1.1, and the derivatives calculated by the Mathematica model described above. Evidently the amount of accuracy sacrificed to the approximations made in Chapter 2 is not large.

The plots in Figures 4.1 and 4.2 show the comparison between the approximate frequency response analysis of Chapter 3 and the Twiddle program. Each plot is labelled H_nm; the first index indicates the output, i.e., V_1 through V_4, and the second index indicates the driven degree of freedom, i.e., Φ_+, ϕ_+, Φ_-, and ϕ_-, in that order. We see from the plots that the approximate analysis is good up to

---

[||] The program contains a generalized form of these equations which can include the effect of having more RF frequencies, as would be appropriate for larger modulation depth.

Figure 4.1 Table of numerical (upper) and approximate analytic (lower) derivatives of interferometer outputs, for the optical parameters given in Table 1.1.

		Derivative with respect to			
		Φ_+	ϕ_+	Φ_-	ϕ_-
Ouput	V_1	-52.6161 -52.5585	-0.226582 -0.221949	0.	0.
	V_2	-4.06208 -4.09635	0.00664 0.00676	0.	0.
	V_3	0.	0.	-27.9861 -28.1611	-0.213105 -0.214438
	V_4	0.	0.	0.000200 0.000207	0.0263128 0.0271507

frequencies of about 1 kHz. The plot of H_11 extends over a broader frequency range than the others; this is useful for the numerical servo design of Chapter 6. The fact that the two curves in this first plot agree up to very high frequencies is accidental since the approximations made in deriving the approximate analytic expression for this response are violated at high frequencies.

Figure 4.2 Frequency response curves calculated using the approximate analytical method and (dashed) the strictly numerical model.

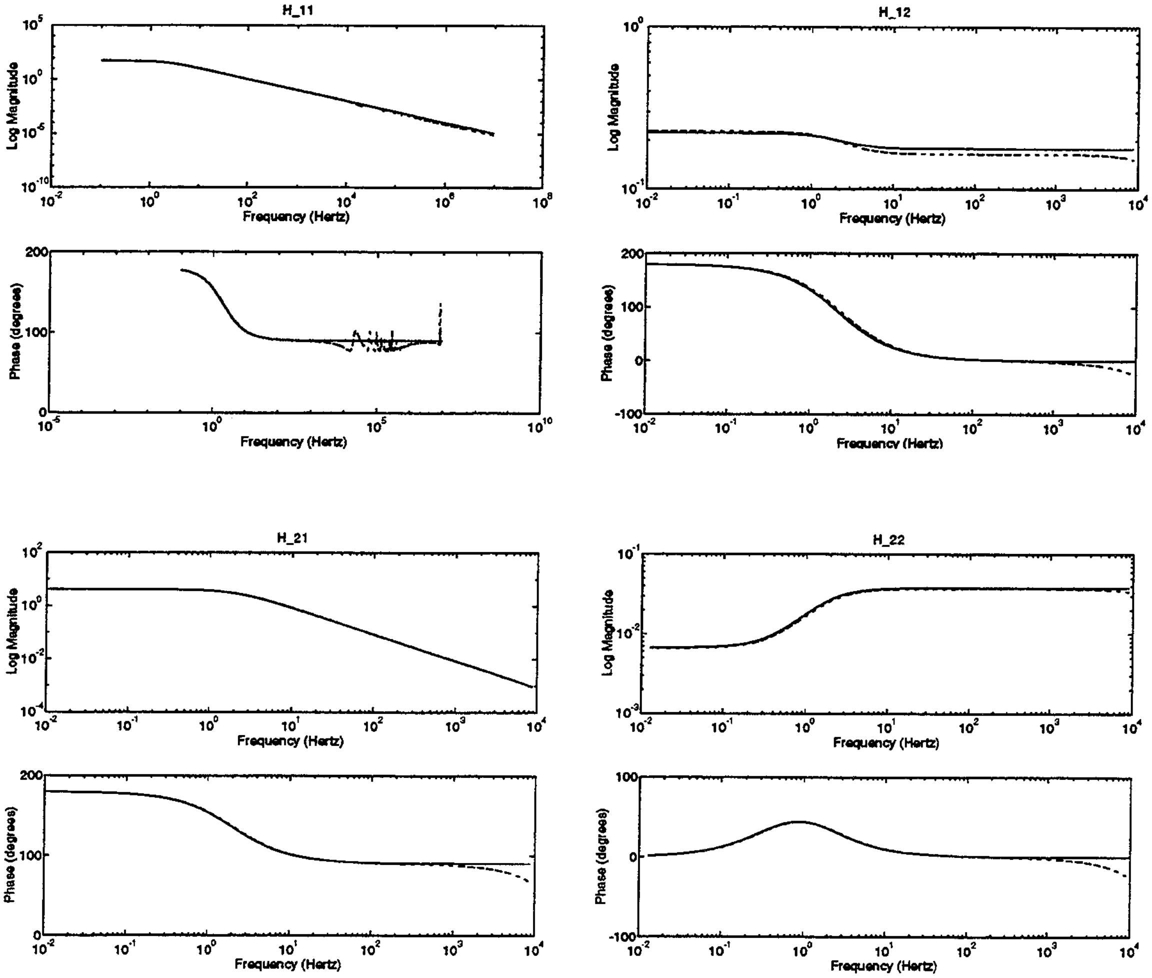

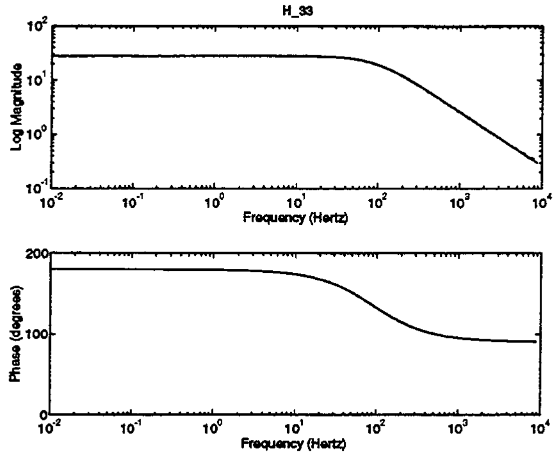
H_33
Log Magnitude
10^2
10^1
10^0
10^{-1}
Frequency (Hertz)
10^{-2} 10^{-1} 10^0 10^1 10^2 10^3 10^4
Phase (degrees)
200
100
0

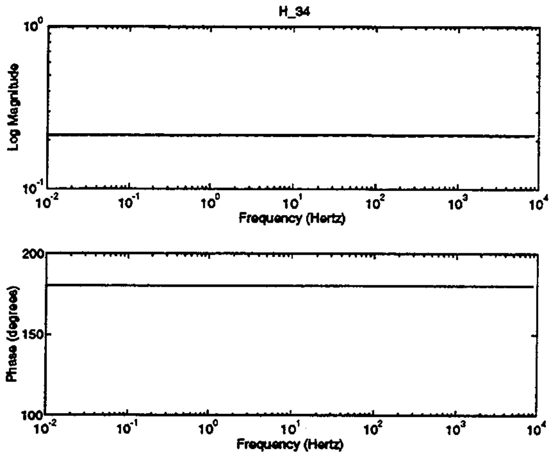
H_34
Log Magnitude
10^0
10^{-1}
Frequency (Hertz)
10^{-2} 10^{-1} 10^0 10^1 10^2 10^3 10^4
Phase (degrees)
200
150
100

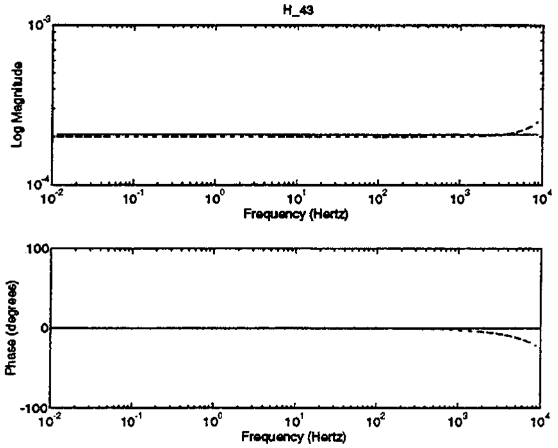
H_43
Log Magnitude
10^{-3}
10^{-4}
Frequency (Hertz)
10^{-2} 10^{-1} 10^0 10^1 10^2 10^3 10^4
Phase (degrees)
100
0
-100

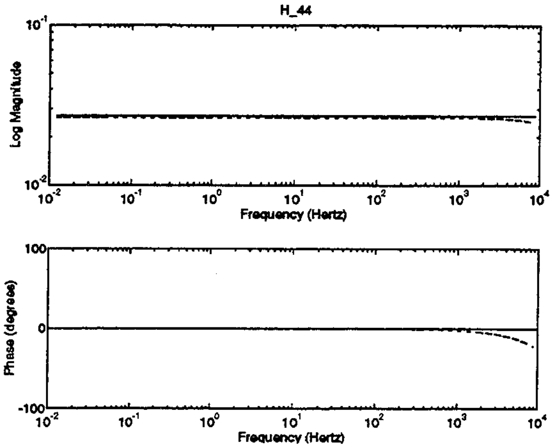
H_44
Log Magnitude
10^{-1}
10^{-2}
Frequency (Hertz)
10^{-2} 10^{-1} 10^0 10^1 10^2 10^3 10^4
Phase (degrees)
100
0
-100

Chapter 5 Experiments with the Table-top Prototype

Several table-top optical configurations of gradually increasing complexity were set up over the past several years. This set of experiments culminated with the construction of a complete interferometer to be described later in this chapter. The formal goal of these experiments was to verify a reasonable number of the predictions of the low-frequency optical model[#]. A secondary motivation was simply to demonstrate the general feasibility of this extraction scheme. A large number of unmodelled effects could in principle make the operation of such a configuration impractical: extreme sensitivity to misalignment, to asymmetry in losses, to mirror imperfections, or difficulty in acquiring lock being important examples. Although the successful construction of a small scale prototype by no means proves that none of these effects will be important in a full-sized interferometer, it nonetheless gives one some comfort.

The first section of this chapter contains a description of the parts from which all of the experiments were set up. The following sections describe the experiments in order of increasing complexity, from the method used to characterize the displacement transducers, to the characterization of a simple

---

[#] It is difficult to test the frequency response model in a table-top experiment because the lengths (hence delays) are shorter and the losses larger; both of these effects lead to optical characteristic frequencies hard to attain with the displacement transducers used.

Fabry-Perot cavity, to the characterization of the three-mirror "coupled cavity" interferometer, and finally, to the characterization of the full interferometer.

5.1 Setup and Hardware

All of the experiments described in this chapter have in common certain aspects of the setup and certain building blocks from which the optical and control configurations were assembled. A (Coherent Innova 100) argon-ion laser operating at 514 nm served as the light source. This laser had been modified by replacing its factory-installed mirrors with mirrors glued to piezo-electric transducers, so that the length of the laser cavity, and thereby the laser wavelength could be adjusted electrically. Furthermore two Pockels cells (Gsänger PM 25) outside of the laser cavity were used to effect high-frequency corrections to the laser wavelength. These feedback elements were driven by a high-bandwidth, low noise amplifier in a configuration which made it possible simply to connect the demodulated signal from an appropriate photodetector to the amplifier input in order to lock the laser frequency to a cavity. This setup had previously been used with another prototype within the LIGO project, and was easily adapted for the work described here. The laser light was phase modulated at 12.33 MHz by an additional Pockels cell (Gsänger PM 25), which was driven by a power amplifier (LIGO 5 Watt Amp #9) and impedance-matching transformer (LIGO Step-Up Transformer). Then the laser beam passed through an acousto-optic modulator (Intra-Action AFD 402) used for power stabilization, through a single-mode optical fiber to improve the beam quality, and through a pair of mode-matching lenses used to produce a beam with a convenient waist size and location. Before entering the fiber, a portion of the beam was diverted to an optical spectrum analyzer which was used to check whether the laser was operating single-mode, and after the fiber, a portion was diverted to a "reference cavity," a Fabry-Perot cavity to which the laser frequency could be locked when a stable frequency was necessary (for example during alignment of the interferometer). Also after the fiber, a stray reflection from a mode-matching lens caught on a photodetector was used to stabilize the power leaving the fiber, by feeding the photodetector signal back to the acousto-optic modulator. A roughly 4 by 10 foot area of optical table was reserved for the construction of various interferometers. A transparent plastic cover with plastic curtains was installed over this area to protect it from air currents and from dust. A small blower equipped with a filter was installed for the purpose of purging the enclosed volume with dust-free air. In addition, a clean bench in the room was operated whenever doing so did not interfere with the experiments. Unfortunately, it was necessary to shut off both the clean bench and the blower whenever it was desired to have an interferometer resonating on the table.

An RF signal was used for phase modulation and as a signal to drive the mixers. Figure 5.1 shows the setup used to generate and distribute the RF

Figure 5.1 RF Distribution.

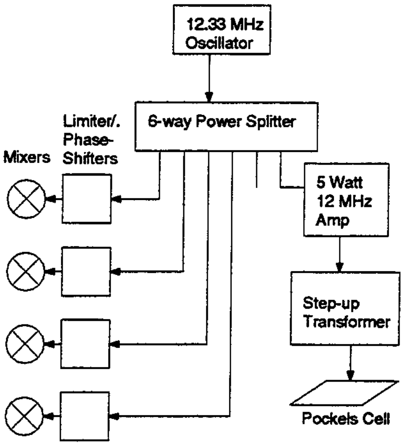

modulation signal.

A relatively small number of building blocks was used to assemble all of the experiments listed herein. Mirrors of various reflectivities were used. Some of the mirrors were mounted on piezo-electric stacks ("displacement transducers") allowing them to be electrically displaced along the beam axis. Some of these were also supported in mirror mounts (Klinger SL25.4BD) provided with piezo-electric fine alignment controls ("orientation transducers"; Marshall Industries #AE0505D08 or AE0505D16, micrometer adapter machined in house). The mirrors were 1 inch diameter mirrors from various manufacturers (but mainly from CVI), with thickness ranging from 1/4 inch to 3/8 inch. Some of the mirrors were superpolished before coating and some were not, but the difference between these two types of mirror was found to be of little importance in the presence of larger losses due to dust. The piezo-electric stacks were made by gluing together (with Stycast #1266 epoxy) two piezo-electric washers (1 inch OD, 0.5 inch ID, type 550, from Piezo Kinetics) with brass washers serving as the electrodes. The mechanical design of the assembly of mirror mounts, displacement transducers, and orientation transducers was adopted, with only minor modifications, from experiments[18,19,20] performed at the Massachusetts Institute of Technology.

Two types of photodiodes were used: tuned RF photodiodes made in house (LIGO #5 and #6), and broadband PIN photodiodes (Thorlabs DET1–Si); the bandwidth of the latter type depends on the load impedance. Photodiodes were used in two applications: low-bandwidth applications where the power at some optical output was measured (here the Thorlabs diodes were used with a 5 k ohm load), and RF applications in which fluctuations in the output intensity at the modulation frequency were measured (by demodulating). Either the less expensive Thorlabs diodes terminated in 50 ohms or the in-house tuned diodes (which provided better signal-to-noise performance) were used in the RF applications. The high-bandwidth photodiodes were sometimes followed with an amplifier (LIGO Comlinear E103 Composite Amplifier, #MEZ 8/17/84, or 1/3 of LIGO Triple W/B Amp) but always with a mixer. Double balanced mixers (Mini-Circuits ZAY–1) were used, followed by low-pass filters to remove the modulation-frequency components from the mixer output. The mixers were driven by limiter/phase shifters (LIGO #3,9,10 and 12), devices which contain an adjustable delay line and a limiting and filtering circuit, so that the output is of fixed amplitude (9 V peak to peak) but the phase delay is adjustable with a pair of knobs on the front panel. The phase-shifters were driven by the output of a 6–way power splitter (Mini-Circuits ZFSC-6–1–BNC), in turn driven by the RF oscillator (LIGO 12.33 MHz Oscillator #4). General purpose adjustable-gain amplifiers were used in various applications and high-voltage amplifiers (LIGO Dual translation PZT Driver, #1 and 2) were used to drive the displacement transducers. These amplifiers (see Figure 5.2 a)) have two inputs (a main input and a "test input," of which a linear combination is formed internally) and two outputs. One output is the high voltage to be applied to the displacement transducer; the other is that voltage divided by 100 and is called the "output monitor" signal.

Figure 5.2 Schematic representation of a high voltage amplifier and the dynamic signal analyzer.

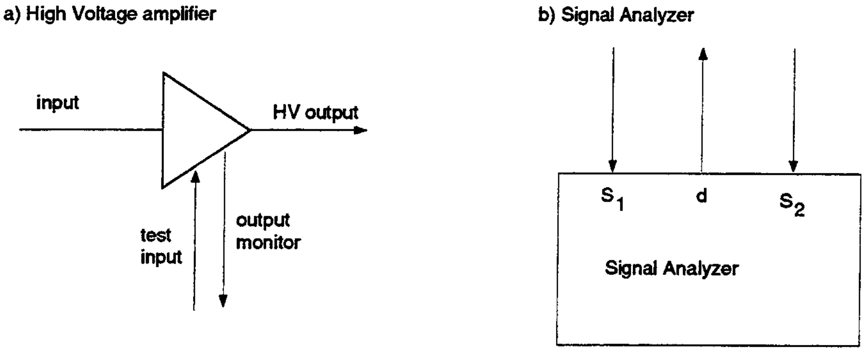

The standard battery of test and measurement equipment was used: oscilloscopes, function generators, and a voltmeter. One piece of equipment which deserves special mention is the HP3562 Dynamic Signal Analyzer (Figure 5.2 b)). This apparatus has the ability to generate a swept frequency sine wave at its output and simultaneously take the ratio of the components at that frequency in the two signals present at its inputs.

5.2 Component Response Measurements

Displacement Transducers

As mentioned earlier, several of the mirrors in the interferometer were supported on piezo-electric transducers (displacement transducers) so that the optical path lengths (and hence the phases) could be modified by applying appropriate voltages to these transducers. The response of each displacement transducer was characterized before installation into the interferometer, for two reasons. First, in order to measure the response of the interferometer to changes in mirror position, it is necessary to know what those changes in position are. Second, it was found that the response of most of the displacement transducers contained a large resonance at around 25 kHz; the installation in the loop of a notch filter, adjusted to cancel the resonance as well as possible, allowed the low frequency loop gain to be increased substantially while keeping the loop gain at the resonance frequency below unity. The setup for displacement transducer characterization is shown in Figure 5.3.

The signal from the photodetector was fed in to a differential amplifier (GP in Figure 5.3), the other input of which was driven by an adjustable voltage source. Before closing the servo loop, the displacement transducer was driven

Figure 5.3 Displacement transducer characterization.

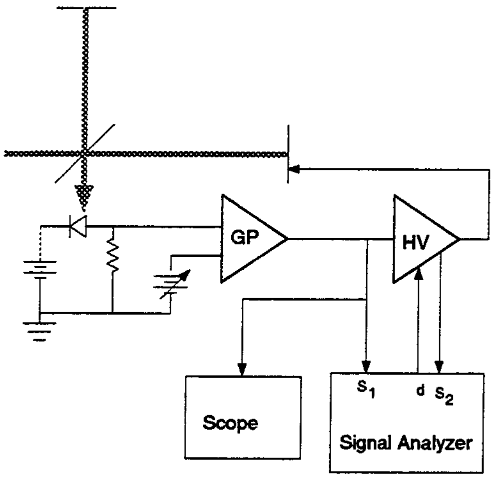

with a large amplitude triangle wave and the voltage supply adjusted so that the differential amplifier output was zero when the signal from the photodetector was halfway between its minimum and maximum values v_{min} and v_{max}. To lock the Michelson, the differential amplifier was fed back to the high voltage amplifier driving the transducer. At this operating point, the derivative of photodetector signal with respect to mirror position is given by

$$\frac{dv}{d(\delta l)} = \frac{2\pi}{\lambda}(v_{max} - v_{min}). \tag{5.1}$$

$\frac{d(\delta l)}{dv_{piezo}}$ was then calculated by dividing this into the response measured with the Michelson interferometer locked, using the signal analyzer.**

** Moving the mirror through a distance of several wavelengths (the displacement transducers typically have a range of $\frac{3}{2}\lambda$) provided an additional opportunity to measure the response of the displacement transducers. This was done simply by counting the number of bright fringes produced at the output for a given voltage change at the displacement transducer. Measurements of displacement transducer response done this way generally yielded values for the response that were about a factor 1.7 larger than the response measured using small driving voltages.

Modulation Index

The modulation index was measured by configuring a Fabry-Perot cavity as an optical spectrum analyzer* (Figure 5.4)

Figure 5.4 Measuring the modulation index.

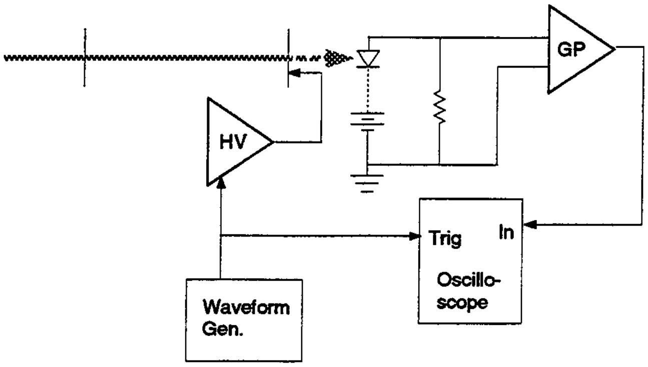

The oscilloscope in this setup would show separate peaks for each frequency component of the light as they individually resonated in the cavity. The modulation index was then calculated from the relative heights of the carrier and RF sideband peaks.

Mixer Gain

The mixer gain was measured by driving the "RF" input (which is normally connected to the photodetector) with a sine wave of known amplitude and at a frequency of 12.3 or 12.4 MHz (the mixer's "Local Oscillator" input was connected to a phase shifter as usual). Under these conditions the (low-passed)

---

* The commercial spectrum analyzer sampling the beam before the fiber had insufficient resolution to measure the modulation index accurately.

mixer output was a sine wave at the difference frequency, a few tens of kilohertz. The mixer response was calculated by taking the ratio of output amplitude to input amplitude.

5.3 Response of a Fabry-Perot Cavity

An initial experiment consisted of measuring the response of a Fabry-Perot cavity. The cavity was locked on resonance and the response measured by driving the summing node, shown in Figure 5.5, and then taking the ratio of the two outputs using the dynamic signal analyzer.

Figure 5.5 Measurement of the response of a Fabry-Perot cavity.

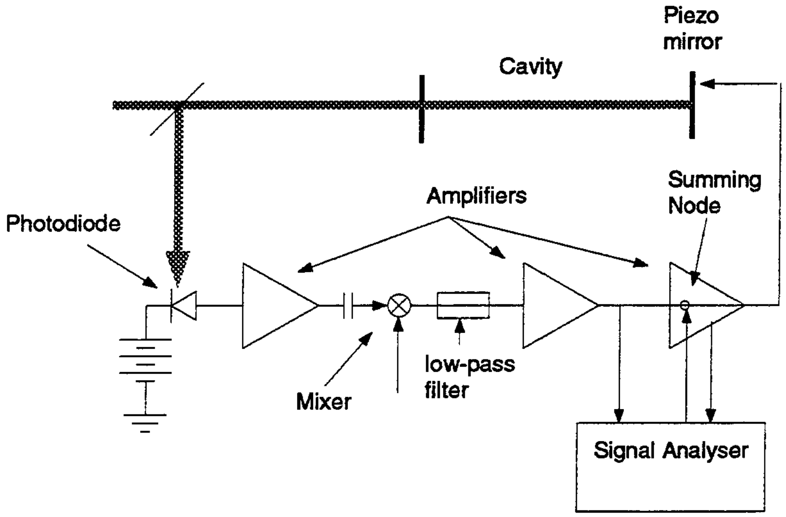

The expected result (calculated by multiplying together the gains of all of the cascaded components) is easily found using (2.7) and (2.19); it is

$$\begin{aligned}\frac{dV_{amp2}}{dV_{piezo}} &= \frac{d(2kx)}{dV_{piezo}} V_{DC} 4 r_{cav} J_0 J_1 N' G_{mixer} G_{amp2} \\ &\simeq 190 \pm 30\end{aligned} \qquad (5.2)$$

Where $\frac{d(2kx)}{dV_{piezo}}$ is the displacement transducer response, V_{DC} is the voltage from the photodiode when the cavity is far from resonance, J_0 and J_1 are Bessel functions evaluated at the modulation index, N' is the augmented bounce number, and G_{mixer} and G_{amp2} are mixer and amplifier gains. The measured result is

$$\frac{dV_{amp2}}{dV_{piezo}} = 172 \pm 9 \tag{5.3}$$

The uncertainty in the measured result is due mainly to fluctuations in alignment. The fact that this is a more accurate way to measure the product of the gains of all of the cascaded elements (than the individual measurement of each factor) was important in obtaining more precise results in experiments with the full interferometer, described below.

5.4 Response of the Coupled-Cavity

The "coupled-cavity" experiment consisted of a three–mirror interferometer as shown in Figure 5.6.

The optical outputs were mixed down and one was fed back to the third mirror, the other to the laser frequency. The response of the interferometer was again measured by injecting a swept-frequency sine wave into a summing node in the displacement transducer-driving amplifier and, using the signal analyzer, taking the ratio of the signal from the mixer to the signal at the displacement transducer.

The DC optical model described in chapter 4 was used to calculate the expected response of the coupled cavity in the absence of any servos. Now let us

Figure 5.6 Coupled-cavity experiment.

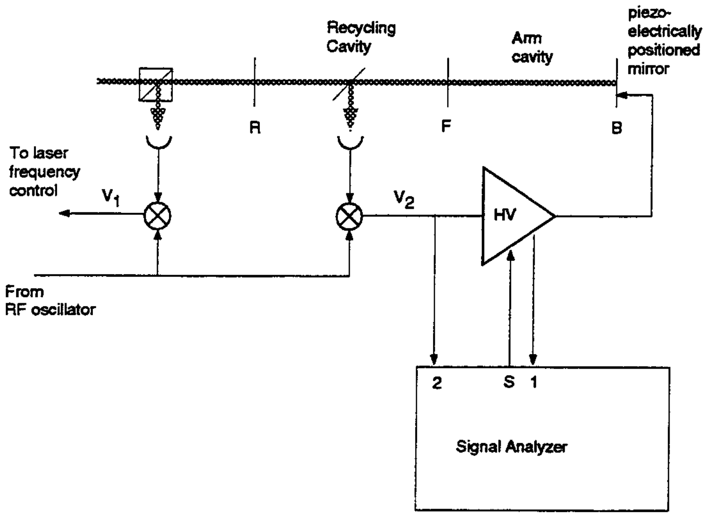

calculate the response in the presence of the servos. We will show that if the gain in the loop feeding back to the laser is sufficiently large, then the measurement described above depends only on the optical response, and not on the gain of either loop. Let the optical response be the matrix $A \equiv \begin{bmatrix} a_{11} & a_{12} \\ a_{21} & a_{22} \end{bmatrix}$ so that

$$\begin{bmatrix} V_1 \\ V_2 \end{bmatrix} = A \begin{bmatrix} x \\ X \end{bmatrix} \tag{5.4}$$

Where X and x represent changes in the length of the arm cavity and the recycling cavity. We want to represent the interferometer as a two-input, two-output device where one of the inputs corresponds to changes in the laser frequency, which is equivalent to equal changes in both X and x. We do this by calling the new system P:

$$\begin{aligned} P &\equiv A \begin{bmatrix} 1 & 0 \\ 1 & 1 \end{bmatrix} \\ &= \begin{bmatrix} a_{11} + a_{12} & a_{12} \\ a_{21} + a_{22} & a_{22} \end{bmatrix} \end{aligned} \tag{5.5}$$

so that

$$\begin{bmatrix} V_1 \\ V_2 \end{bmatrix} = P \begin{bmatrix} \frac{\lambda l}{c} \delta \nu \\ \delta X \end{bmatrix} \tag{5.6}$$

where l is the cavity length and λ the optical wavelength.

The two feedback amplifiers we group into a "controller"

$$C = \begin{bmatrix} g_1 & 0 \\ 0 & g_2 \end{bmatrix} \tag{5.7}$$

Figure 5.7 Block diagram of the control system for the coupled-cavity experiment.

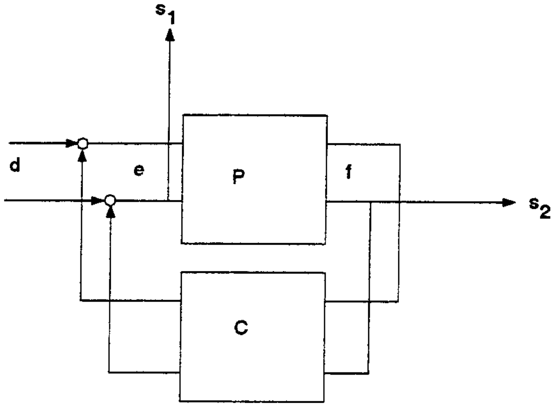

Then the closed-loop response can be calculated with simple matrix manipulations[†]:

$$\begin{aligned} \vec{e} &= \vec{d} + CP\vec{e} \\ &= [1 - CP]^{-1}\vec{d} \end{aligned} \tag{5.8}$$

[†] Historically, in control theory, the points in the loop where signals are summed in have often been taken as differencing, rather than summing nodes. This convention becomes awkward if nodes exist at several points in a loop or if no nodes exist at all (the latter case is of interest when analyzing stability). We will use the convention that no changes of sign occur except where they are explicitly included. Because of this, some of the expressions we derive may differ by a sign from expressions found in some textbooks.

$$\vec{f} = P[1 - CP]^{-1}\vec{d} \tag{5.9}$$

The experiment illustrated above corresponds to this block diagram with

$$\vec{d} = \begin{bmatrix} 0 \\ d_2 \end{bmatrix} \tag{5.10}$$

the signal analyzer then measures

$$\begin{aligned} \frac{s_2}{s_1} &= \frac{a_{22} - g_1 \det A}{1 - g_1(a_{11} + a_{12})} \\ &\simeq \frac{\det A}{a_{11} + a_{12}} \end{aligned} \tag{5.11}$$

where the approximation is valid when g_1 is very large[‡]. As in section 5.3 above, the value of this expression was multiplied by the appropriate factors such as power on the photodiode, $J_0 J_1$, the displacement transducer response, and the amplifier gains, and compared to the measured values.

Table 5.1 below shows the measured and calculated response for two different values of the recycling mirror (labelled "R" in Figure 5.6) and several different values of the modulation index. The agreement was good for small modulation depths and fair for larger modulation depths. It is suspected that the larger discrepancy at larger modulation index is due to the fact that this optical model excludes the effect of the higher harmonics generated in the optical spectrum when the modulation index is large.

[‡] Specifically, for the approximation to be valid, we require $|g_1| \gg |a_{22}/\det(A)|$ and $|g_1| \gg |1/(a_{11} + a_{22})|$

Table 5.1 Results of Coupled-Cavity Experiments

T_1	$\frac{J_1^2}{J_0^2+J_1^2}$	Response (dB)	
		Measured	Calculated
8.9%	0.012	46	49
16.9%	0.012	31	32
16.9%	0.10	36	40
8.9%	0.17	56	58
16.9%	0.17	39	42

5.5 Response of the Complete Interferometer

Once the coupled-cavity experiment was deemed adequately understood, a complete interferometer was set up. Its layout is shown in Figure 5.8. The recycling cavity and both arm cavities were folded in half; the recycling cavity because it needed to be slightly in excess of 6 m in length and the arm cavities to allow the convenient use of cavity back mirrors with the same curvature as that of the recycling mirror. Table 5.2 shows the optical properties of the interferometer. The loss in the arm cavities was mainly due to dust on the mirrors and in the air, and the loss in the recycling cavity is presumed to be mainly due to pick-off reflectivity and dust and scattering loss on the surfaces within that cavity*.

Alignment of each arm cavity was done by observing the light transmitted through the back mirror with an oscilloscope while driving the back mirror with a large amplitude triangle wave. The oscilloscope would show a number of peaks,

---

* Light traveling around the recycling cavity encounters an average of 16 surfaces during one round trip (counting surfaces encountered twice as two surfaces).

Table 5.2 Fixed Mass Interferometer Optical Properties

Fabry-Perot Arm Cavities	Front Mirror Transmission	9 %
	Back Mirror Transmission	13 ppm
	Losses	0.2 %
	Fringe Visibility	9 %
	Cavity Gain	40
Recycling Cavity	Recycling Mirror Transmission	18 %
	Cavity Losses (including Pickoff beams)	16 %
	Fringe Visibilty	88 %
	Recycling Factor	4
Beam splitter	Contrast	99 %

one for each resonant transverse mode, and one for each frequency of light incident on the cavity. The height of the peak corresponding to the carrier resonating in the (degenerate) 01 and 10 transverse modes was then minimized by adjusting the orientation transducer voltages. The recycling mirror was aligned by driving both it and the second arm steering mirror (SAS in Figure 5.8) with triangle waves (at different frequencies) and again minimizing the peak corresponding to the 01 and 10 transverse modes.

The feedback configuration which was used is shown in Figure 5.9[†]. This

---

[†] Although the figure shows loop 4 driving the beam splitter, this drive was actually applied to the second arm steering

Figure 5.8 Layout of complete interferometer.

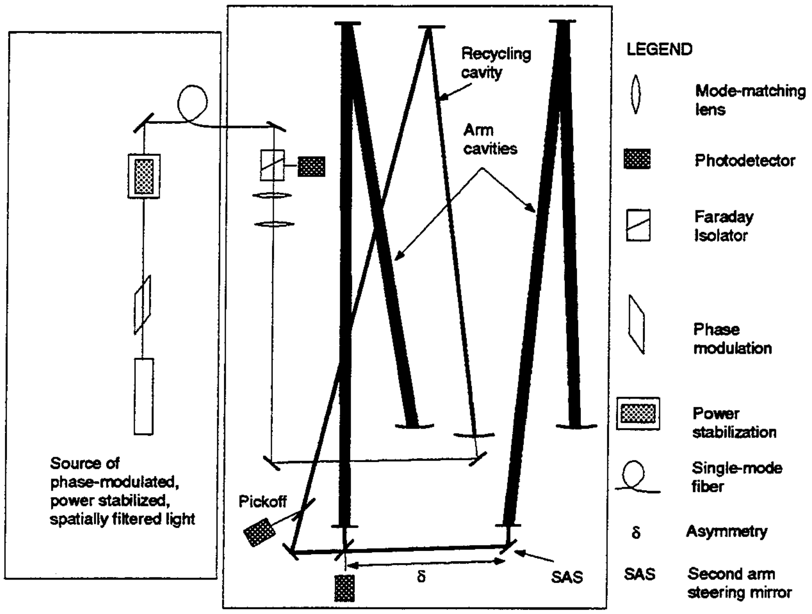

configuration is quite different from the more balanced configuration which would be used in LIGO; however it holds the interferometer on resonance and thus is adequate for the purpose of verifying the calculations made with the optical model.

Arranging for the interferometer to lock initially was a problem which was only solved by the application of considerable amounts of patience. The "method" used to adjust the four gains and mixer phases to their operating values was to observe the light transmitted through one of the cavity back mirrors with a pair of photodiodes connected to a storage oscilloscope, while driving several of the mirrors with low-frequency triangle waves. The drive and whatever other sources

---

mirror (see Figure 5.8). The effect of driving the second arm steering mirror is nearly the same as the effect of driving the beam splitter; one changes only the optical path length (l_P) from the recycling mirror to the first arm, and the other changes only the optical path length (l_I) from the recycling mirror to the second arm.

of disturbance were present would occasionally cause the interferometer to pass close to resonance, and the storage oscilloscope would then record the length of time the servos held it resonant, typically only a fraction of a millisecond when the various connections were first established. The operator would change a setting on some gain or phase dial, and again watch the oscilloscope, to see whether this change improved or worsened the performance. The servos were adjusted in order of the degree to which they are critical to resonance: the laser frequency servo first (because the laser frequency contains the most noise and because deviations in the laser frequency push the interferometer away from resonance most effectively), the servo driven by the gravitational-wave signal second, and the remaining two in either order.

Figure 5.9 Servo configuration of Table-top prototype. Feedback amplifiers not shown.

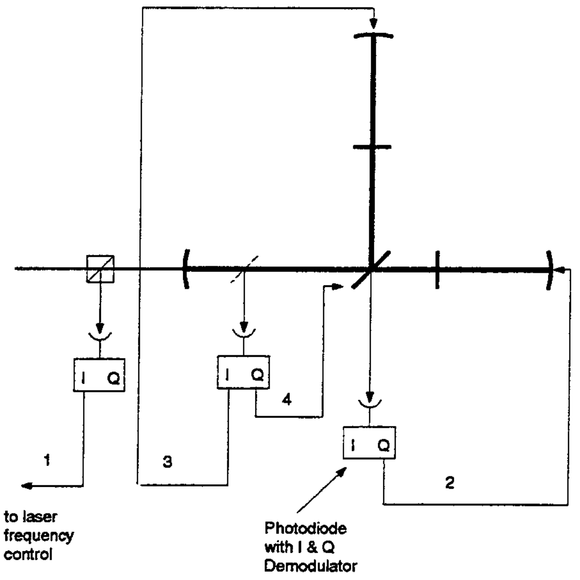

Once the amplifiers and mixers were properly set up, however, the interferometer would acquire lock with remarkable ease. The mechanism by which this occurs is not yet fully understood, but it was found that when the second arm steering mirror was moved back and forth slowly with the other servos active, the other servos would acquire lock and hold it until the continuing motion of the second arm steering mirror destroyed the resonance (resonance is relatively insensitive to the positions of the beam splitter and second arm steering mirror, as we see in Appendix B). This fact made it easy to devise an automatic lock-acquisition system: the power transmitted through each of the two arm cavity back mirrors is compared to a threshold. When either power level is below threshold, the second arm steering mirror displacement transducer is driven by a triangle wave; once both power levels exceed their respective thresholds, the second arm steering mirror drive is disconnected from the triangle wave source and connected to the amplifier which supplies the appropriate feedback signal. Figure 5.10 is a set of oscilloscope traces showing the light levels in the interferometer and the voltage applied to the second arm steering mirror displacement transducer. When the interferometer is knocked out of lock (in this case by rapping one's knuckles on the optical table cover), the voltage begins to ramp up and down; once resonance is re-established the circuitry disconnects the ramp and reconnects the servo loop.

Closed-loop response measurements were made as shown in Figure 5.11. Loop numbering is shown in Figure 5.9. If a driving signal d is applied in loop j

Figure 5.10 Time record of lock interruption.

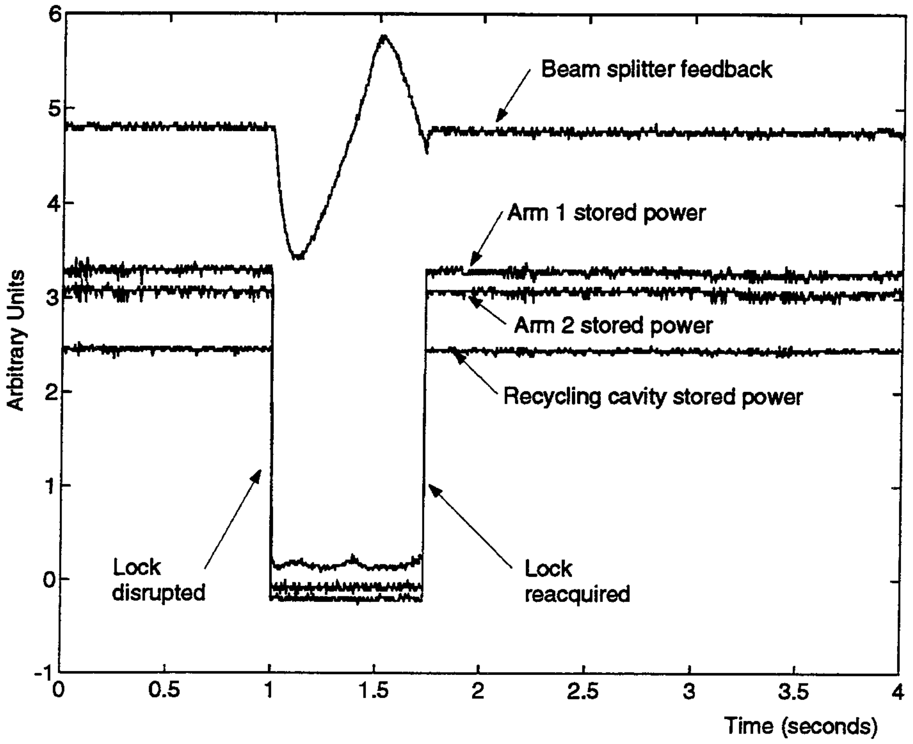

by the signal analyzer, and the analyzer inputs are connected to the displacement drive signal of loop j and to the mixer output in loop k respectively, then the expected ratio* of the signals at the two outputs is

$$\begin{aligned} H_{jk} &\equiv \frac{s_2}{s_1} \\ &= \frac{1}{G_k} \frac{(GBPA)_{row\,k} \cdot \left([1+GBPA]^{-1}\right)_{col\,j}}{\left([1+GBPA]^{-1}\right)_{jj}} \end{aligned} \tag{5.12}$$

---

* Mathematica code was used to calculate the interferometer response, and Matlab® code was used to calculate the closed-loop response given the interferometer response. Matlab® is a registered trademark of The MathWorks, Inc.

Figure 5.11 Block diagram representing setup for closed loop measurements.

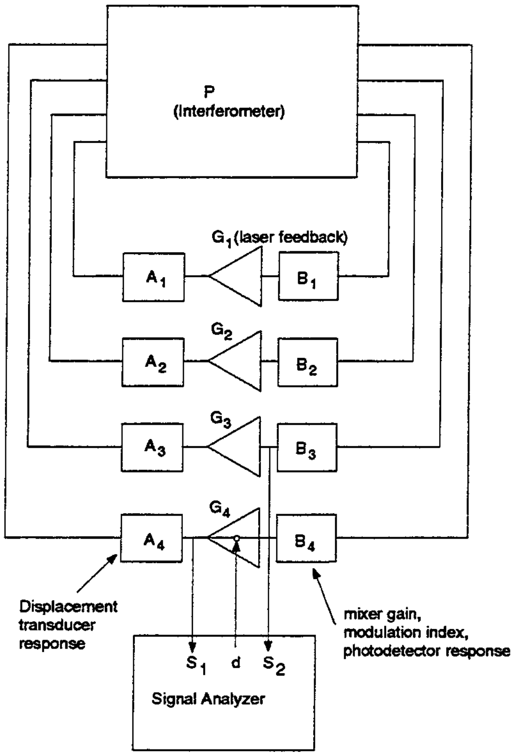

where P is a matrix representing the interferometer response, and A, B, and G are diagonal matrices representing the A_k, B_k, and G_k, respectively. The products $A_i B_k$ were found using

$$\frac{s_2}{s_1}|_{FP} = B_k P_{cavity} A_i \tag{5.13}$$

where $\frac{s_2}{s_1}|_{FP}$ was measured, as shown in Figure 5.12, in each case using a single Fabry-Perot cavity, whose response P_{cavity} is deemed understood.

The responses calculated (and measured) for the full interferometer, unlike the coupled-cavity response, are not frequency independent. Although the plant is still frequency independent, and the gain of the laser frequency servo large enough

Figure 5.12 Setup for measuring the factors A_i and B_k.

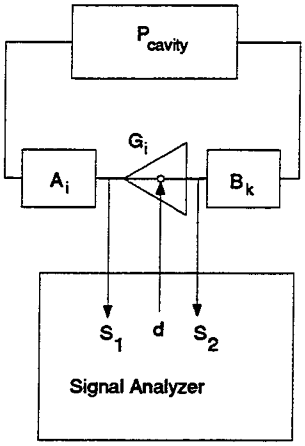

to make changes in it (with frequency) irrelevant, the gains of the remaining loops do change significantly with frequency over the range where the measurements were made. Figure 5.13 shows plots of experimental and calculated response (H_{jk}) for measurements made by driving loop j and measuring the response in loop k, with both of those indices ranging from 2 to 4. Phase plots are modulo 180° and are shown for reference only. The laser frequency loop was excluded from these measurements because it was difficult to achieve adequate signal to noise ratio without disrupting lock in any measurement where a signal was injected into the laser frequency loop*. In addition, samples of the plotted curves (at 2

---

* Some readers may consider this result counterintuitive (this author certainly does). How can it be that the noise is large enough that adding a signal comparable to the noise even in a small frequency band disrupts lock, yet small enough that the entire noise power over all frequencies does not disrupt lock? The answer is that the element which behaves in a non-linear manner, disrupting lock, is in general located at a different point in the loop from the point where we measure the output.

Table 5.3 Sampled values of experimental (bold) and calculated response.

Measured and Calculated Response at 2 kHz (dB)		Loop in which response measured		
		2	3	4
Loop Driven	2	**38.3** 37.7	**9.86** 16.4	**15.4** 17.8
	3	**26.9** 24.6	**19.0** 22.1	**23.6** 23.4
	4	**24.6** 25.8	**27.3** 31.8	**36.3** 36.9

kHz) are presented in Table 5.3, in order to allow the data to be summarized more compactly.

The experimental uncertainty estimated for these results is about ±3 dB, due mainly to uncertainty in the displacement transducer response (about ±1 dB),

---

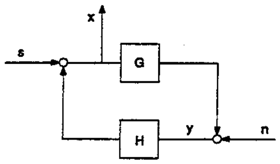

The figure above shows a block diagram of a system with two inputs, a signal s and a noise source n. If the point in the loop which limits the dynamic range (the point where non-linear behavior occurs most easily) is at the input to H, then the condition for maintaining lock can be written

$$y = \frac{n}{1-GH} + \frac{Gs}{1-GH} < y_{max} \tag{5.14}$$

From which

$$n < (1-GH)y_{max} \tag{5.15}$$

$$s < \frac{1-GH}{G} y_{max} \tag{5.16}$$

and the maximum contribution to $x = s/(1-GH) + nH/(1-GH)$ that the inputs can produce is given by y_{max}/G and y_{max}/H for the signal and the noise input, respectively. The dynamic range constrained signal-to-noise ratio can take any value, depending on the distribution of gain within the loop.

uncertainty in the losses in the arm cavities* (about ±1.5 dB), and fluctuations in alignment (about ±2 dB). All of the plots of experimental versus calculated response show reasonable agreement within this uncertainty except for the case of H_{23}, where the discrepancy is perhaps twice the experimental uncertainty. It is not known whether this discrepancy is due to a random large fluctuation in the cumulative error or to an unmodeled systematic effect.

---

* The fractional uncertainty in the arm cavity round trip loss was perhaps +/-50% (due to fluctuating dust levels), but the corresponding fractional uncertainty in the recycling cavity round trip loss only about +/-15%, since arm cavity loss was not the dominant loss in the optical system.

Figure 5.13 Plots of experimental and calculated (dashed) response.

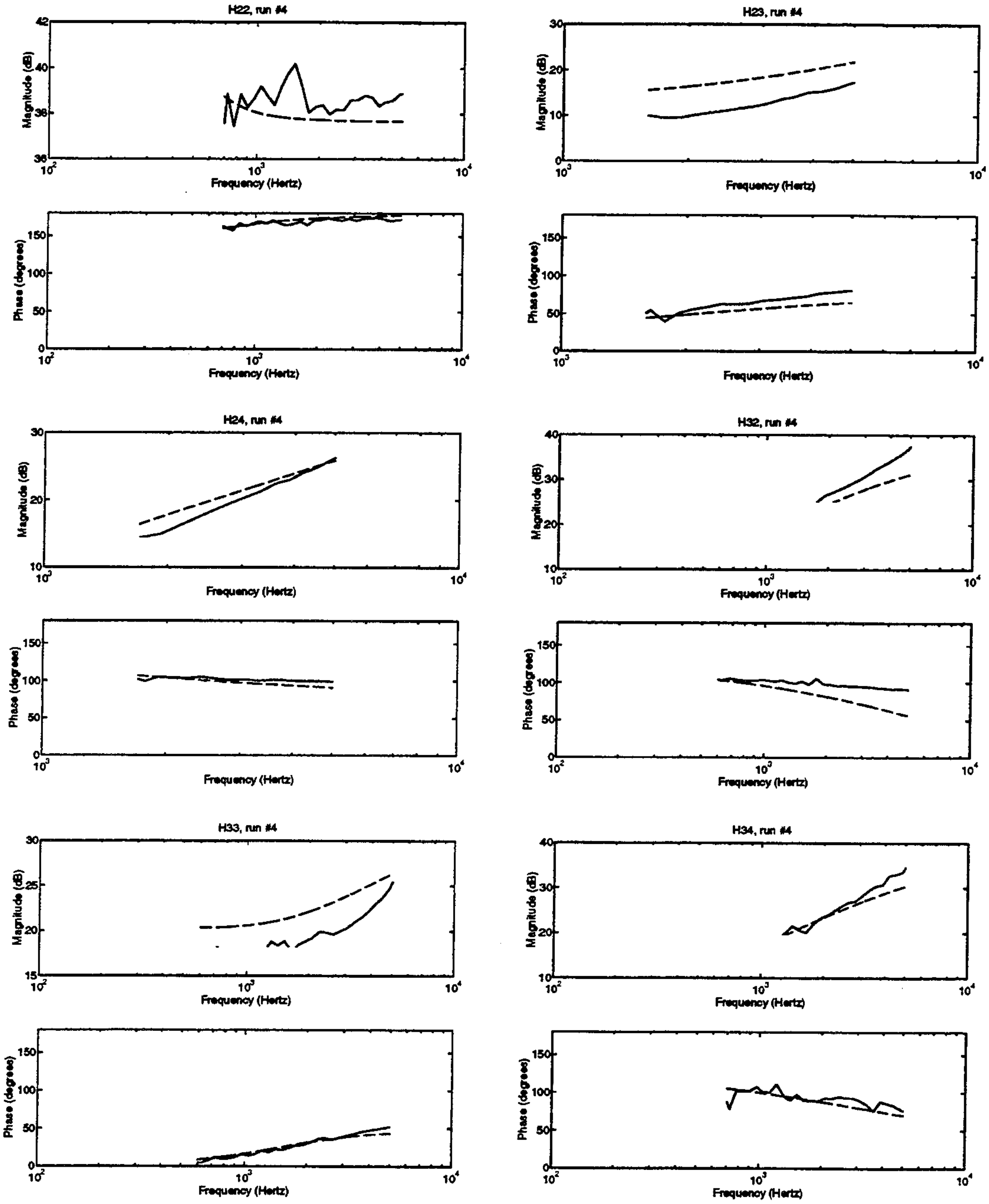

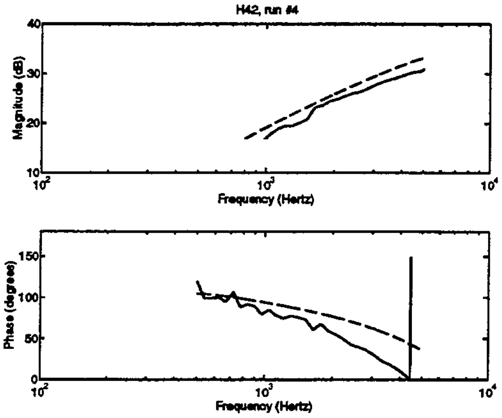
H42, run #4
Magnitude (dB)
40
30
20
10
10^2
10^3
10^4
Frequency (Hertz)
Phase (degrees)
150
100
50
0
10^2
10^3
10^4
Frequency (Hertz)

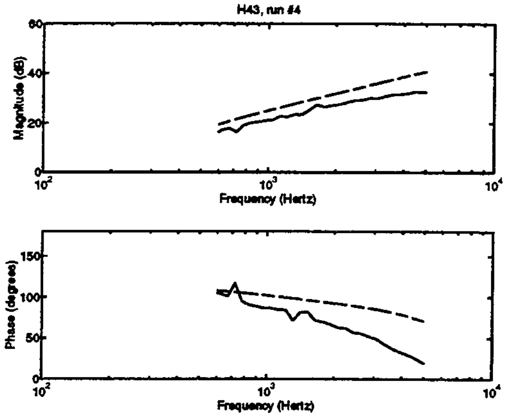
H43, run #4
Magnitude (dB)
60
40
20
0
10^2
10^3
10^4
Frequency (Hertz)
Phase (degrees)
150
100
50
0
10^2
10^3
10^4
Frequency (Hertz)

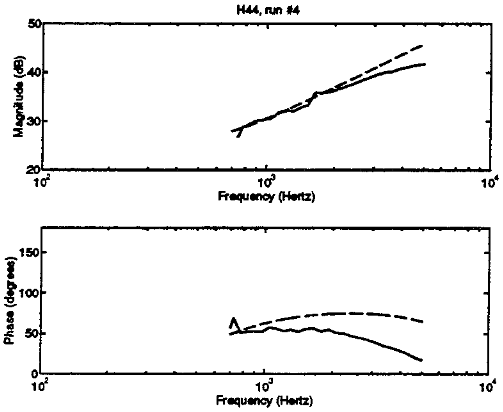
H44, run #4
Magnitude (dB)
50
40
30
20
10^2
10^3
10^4
Frequency (Hertz)
Phase (degrees)
150
100
50
0
10^2
10^3
10^4
Frequency (Hertz)

Chapter 6 Design and Analysis of a Control System

If we consider the interferometer as a four-input, four-output device, then the problem of designing a control system is that of constructing another 4x4 device which when connected to those inputs and outputs will suppress seismic disturbances and keep the interferometer on resonance. At this level of generality the problem is quite complex, and the only systematic approaches known are purely numerical. Our approach will be instead to make a number of simplifying assumptions about the structure of the controller, to develop some guidelines for the design of a control system, and then to use numerical methods to calculate the expected performance.

First let us write the matrix of transfer functions of our interferometer in a simpler form. We assume that we can connect amplifiers with arbitrary (stable) frequency response and gain to the outputs of the interferometer and we will choose the gain and frequency response of these amplifiers to make the new system as simple as possible. This simplified system we will call the "plant." Its transfer functions can be written in matrix form:

$$\begin{bmatrix} V_1 \\ V_2 \\ V_3 \\ V_4 \end{bmatrix} = \begin{bmatrix} 1 & \varepsilon_1(s) & 0 & 0 \\ 1 & \varepsilon_2(s) & 0 & 0 \\ 0 & 0 & 1 & \varepsilon_3(s) \\ 0 & 0 & \varepsilon_4(s) & 1 \end{bmatrix} \begin{bmatrix} \Phi_+ \\ \phi_+ \\ \Phi_- \\ \phi_- \end{bmatrix} \tag{6.1}$$

Figure 6.1 Equivalent block diagrams for the plant.

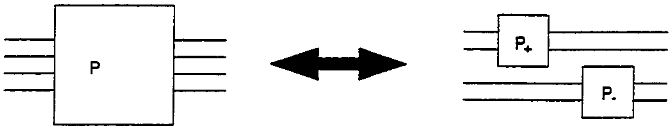

Figure 6.2 Closed-loop system.

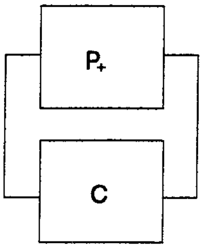

Since the plant is block-diagonal, it is equivalent, as shown in Figure 6.1, to two disconnected sub-plants, the common-mode sub-plant P_+ and the differential-mode sub-plant P_-.

There P_+ and P_- correspond to the upper left and lower right 2x2 blocks of P. P_- is a simple subsystem to control because it is nearly diagonal; it represents two loops which are almost independent. P_+ on the other hand is difficult to control because it consists of two rows which are barely linearly independent. We will spend most of the rest of this chapter considering the problem of designing an adequate control system for P_+.

This problem, then, consists of finding a matrix of transfer functions such that the closed loop system of Figure 6.2 performs adequately. We will make an effort to design a controller C which is diagonal, which means that it consists of two independent feedback amplifiers, C_1 and C_2 as shown in Figure 6.3.

Figure 6.3 Closed-loop system with a diagonal controller.

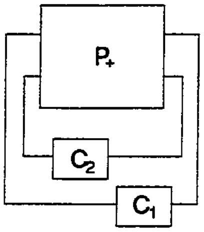

Figure 6.4 Closed-loop system with a "crossed" controller.

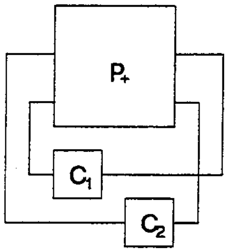

If we can achieve adequate performance with such a controller, then we will have avoided some complexity. Several questions arise in the design of this controller which do not arise in the design of a controller for the P_- sub-plant. For one thing, it is not obvious for the P_+ system which output should be fed back to which input. For P_- that choice of connection scheme is guided by the fairly intuitive rule that each output is fed back to that input to which the output is most sensitive.

In the P_+ system it may be better to connect the feedback in the "crossed" configuration illustrated in Figure 6.4. The system obtained this way is equivalent to the system we get by re-numbering the rows of P_+ (i.e., interchanging ε_1 and ε_2) and connecting the amplifiers in the "straight" configuration illustrated in Figure 6.3.

Another important concern is that the transfer functions of P_+ may contain right-half-plane zeros, as we can see from (3.71) and (3.72). It is well known[21,22] that in a one-dimensional servo loop, right-half-plane zeros in the plant limit the achievable unity-gain frequency. In our case, we may wish to design the optical system to avoid such problems. We will investigate the effects of right-half-plane zeros in the first section of this chapter.

In the second section, we will consider the size of the performance price we are paying by using a signal-extraction system which produces a poorly-conditioned plant. Other signal extraction methods[23], which at the expense of increased complexity produce a very well-conditioned plant, are available for sensing deviations from resonance in the interferometer, and in evaluating the relative merits of the system presented herein against such an alternative, performance benefits are an important criterion.

At the end of this chapter, as a demonstration of the design guidelines we will have seen, we will design a control system for the example interferometer we have been carrying, and we will evaluate its performance numerically.

6.1 Feedback Configuration and Gain Constraint

The frequency-independent 2x2 plant

Consider a system as shown in Figure 6.5, with a plant

$$P = \begin{bmatrix} 1 & \xi_1 \\ 1 & \xi_2 \end{bmatrix} \tag{6.2}$$

Figure 6.5 Block diagram for analysis of system containing frequency-independent plant.

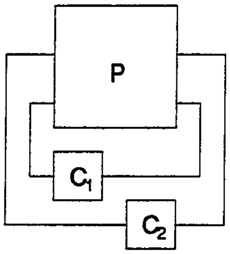

where ξ_1 and ξ_2 are constants. We will use very simple feedback amplifiers with one pole each (both at the same frequency $\omega_a/(2\pi)$) and we will leave ourselves the freedom to adjust the polarity and gain of each amplifier:

$$C_1 = \frac{Q_1K_1}{1+\frac{s}{\omega_a}} \tag{6.3}$$

and

$$C_2 = \frac{Q_2K_2}{1+\frac{s}{\omega_a}} \tag{6.4}$$

where $\omega_a \geq 0$ (for stable amplifiers), the $Q_i = \mp 1$ represent polarity switches, and the $K_i \geq 0$ represent adjustable gain controls. Since C and P are open-loop stable, the closed-loop system is stable if and only if[†] $\det[1-CP]$ contains no right-half-plane zeros[24]. Now

$$\begin{aligned}\det[1-CP] &= 1 - \frac{Q_1K_1}{1+\frac{s}{\omega_a}} - \frac{Q_2K_2\xi_2}{1+\frac{s}{\omega_a}} + \frac{K_1K_2(\xi_2-\xi_1)}{\left(1+\frac{s}{\omega_a}\right)^2} \\ &= \frac{1}{\left(1+\frac{s}{\omega_a}\right)^2}[1 - Q_1K_1 - Q_2K_2\xi_2 + Q_1K_1Q_2K_2(\xi_2-\xi_1) \\ &\qquad + (2 - Q_1K_1 - Q_2K_2\xi_2)\frac{s}{\omega_a} + \left(\frac{s}{\omega_a}\right)^2]\end{aligned} \tag{6.5}$$

[†] We will continue to use the feedback sign convention explained in the footnote on page 84.

We know that a polynomial with real coefficients has zeroes with positive real part if any pair of coefficients has opposite signs[25] (for a quadratic, it can be shown that the latter is also a necessary condition for the former). The last coefficient ($\left(\frac{1}{\omega_a}\right)^2$) in the numerator polynomial (in s) is positive, so for stability, all of the remaining coefficients must be positive.

Now suppose we choose $Q_1 = 1$ and we want to start off with $K_1 = K_2 = 0$ and then increase the gain K_1 first. If we increase it to the point where $K_1 > 1$ the system will be unstable since the coefficient of s^0 becomes negative. This is an undesirable situation because we would prefer to be able to increase the gains arbitrarily and enjoy the resulting improvements in performance. In this case it is easy to understand what is wrong; as in a one-dimensional servo, if the sign of the feedback is wrong, the system will be unstable for gain exceeding a certain threshold. We need to choose $Q_1 = -1$ to avoid this problem. Similarly we find that if $\xi_2 > 0$ then we need to choose $Q_2 = -1$ to be allowed arbitrary K_2 when $K_1 = 0$.

We might ask whether these choices of polarity guarantee stability for all values of the gains K_1 and K_2. The answer is "no": As we can see from the last coefficient of s^0 in (6.5), if $\xi_2 - \xi_1 < 0$, the system is unstable if

$$K_1 K_2 > \frac{1 + K_1 + K_2 \xi_2}{\xi_1 - \xi_2} \tag{6.6}$$

so again the gain is constrained by stability considerations. It is easy to verify that had we numbered our outputs differently we would have had a stable system no matter what (non-negative) values we chose for K_1 and K_2. Equivalently, had we hooked up the amplifiers in the crossed configuration, the corresponding term in the s^0 coefficient would have been $\xi_1 - \xi_2$ and again the system would have been stable for any non-negative K_1 and K_2.

With this motivation, we make the following

Definition:

The closed-loop system consisting of the plant P and two controllers $C_1 = \frac{Q_1 K_1}{1+\frac{s}{\omega_a}}$ and $C_2 = \frac{Q_2 K_2}{1+\frac{s}{\omega_a}}$ is *gain constrained* if $\nexists Q_1, Q_2 \epsilon \{1, -1\}$ such that the system is stable for all positive real values of K_1 and K_2.

Now we can show the following:

Theorem 1:

The system consisting of the plant $P = \begin{bmatrix} 1 & \xi_1 \\ 1 & \xi_2 \end{bmatrix}$ and controllers $C_1 = \frac{Q_1 K_1}{1+\frac{s}{\omega_a}}$ and $C_2 = \frac{Q_2 K_2}{1+\frac{s}{\omega_a}}$ connected in the straight configuration is gain constrained if and only if

$$\xi_2(\xi_2 - \xi_1) < 0 \tag{6.7}$$

Proof:

Sufficiency: $\xi_2(\xi_2 - \xi_1) < 0$ implies either

i. $\xi_2 > 0$ and $\xi_2 - \xi_1 < 0$ or

ii. $\xi_2 < 0$ and $\xi_2 - \xi_1 > 0$

Case i) is the one we looked at in the example and we saw that it is gain-constrained. In case ii), if we choose $Q_2 = -1$ then the term $-Q_2K_2\xi_2$ is negative and the coefficient of s^0 becomes negative for large K_2. If we choose $Q_2 = 1$, the term $Q_1K_1Q_2K_2(\xi_2 - \xi_1)$ is negative.

Necessity: If $\xi_2(\xi_2 - \xi_1) > 0$ we take $Q_1 = -1$ and the sign of Q_2 opposite the sign of ξ_2. Then all of the coefficients in the numerator of (6.5) are non-negative for all values of K_1 and K_2.

Frequency-dependent plant

Now we will prove a weaker but more relevant result.

Theorem 2:

the system consisting of the plant[‡]

$$P = \begin{bmatrix} 1 & \xi_1\left(1 + \frac{s}{\omega_1}\right) \\ 1 & \xi_2\left(1 + \frac{s}{\omega_2}\right) \end{bmatrix} \tag{6.8}$$

and the controllers

$$C_1 = \frac{Q_1K_1}{1 + \frac{s}{\omega_a}} \tag{6.9}$$

and

$$C_2 = \frac{Q_2K_2}{\left(1 + \frac{s}{\omega_a}\right)^2} \tag{6.10}$$

[‡] P_+ can be written in this form by factoring $\frac{1}{1+\frac{s}{\omega_{cc}}}$ out of (3.57), (3.61), (3.71), and (3.72).

connected in the straight configuration is gain-constrained if any of the following is true:

i. $\xi_2(\xi_2 - \xi_1) < 0$

ii. $\xi_2\left(\frac{\xi_2}{\omega_2} - \frac{\xi_1}{\omega_1}\right) < 0$

iii. $\omega_2 < 0$

Proof:

As before, we form

$$\begin{aligned}
\det[1 - CP] &= 1 - \frac{Q_1K_1}{1 + \frac{s}{\omega_a}} - \frac{Q_2K_2\xi_2\left(1 + \frac{s}{\omega_2}\right)}{\left(1 + \frac{s}{\omega_a}\right)^2} \\
&\qquad + \frac{Q_1K_1Q_2K_2\left[\xi_2\left(1 + \frac{s}{\omega_2}\right) - \xi_1\left(1 + \frac{s}{\omega_1}\right)\right]}{\left(1 + \frac{s}{\omega_a}\right)^3} \\
&= \frac{1}{\left(1 + \frac{s}{\omega_a}\right)^3}\{[1 - Q_1K_1 - Q_2K_2\xi_2 + Q_1K_1Q_2K_2(\xi_2 - \xi_1)] \\
&\quad + [3 - 2Q_1K_1 - Q_2K_2\xi_2\left(1 + \frac{\omega_a}{\omega_2}\right) \\
&\qquad + Q_1K_1Q_2K_2\omega_a\left(\frac{\xi_2}{\omega_2} - \frac{\xi_1}{\omega_1}\right)]\left(\frac{s}{\omega_a}\right) \\
&\quad + \left[3 - Q_1K_1 - Q_2K_2\xi_2\frac{\omega_a}{\omega_2}\right]\left(\frac{s}{\omega_a}\right)^2 + \left(\frac{s}{\omega_a}\right)^3\}
\end{aligned} \tag{6.11}$$

Now it is easy to see that if any of the conditions listed in the theorem holds, then at least one of the coefficients of K_1, K_2, or K_1K_2 will be negative and the system will be unstable for some values of these gains.

Implications for the Interferometer

Because of the way in which we numbered the interferometer outputs, the feedback configuration of Figure 1.7 corresponds to the straight configuration for P_+. In Chapter 7 we will see that this has an important advantage over the crossed configuration (with the same numbering). We let

$$\xi_1\left(1+\frac{s}{\omega_1}\right) \equiv \frac{H_{v_1\phi_+}(s)}{H_{v_1\Phi_+}(s)} \tag{6.12}$$

Substituting from (2.77), (2.78), (3.57) and (3.72), we get

$$\xi_1 = \frac{N_0' - N_1'}{N_0'|r_{c0}'|} \tag{6.13}$$

and

$$\omega_1 = \frac{N_1' - N_0'}{N_1'}\omega_{cc} \tag{6.14}$$

Similarly, letting

$$\xi_2\left(1+\frac{s}{\omega_2}\right) \equiv \frac{H_{v_2\phi_+}(s)}{H_{v_2\Phi_+}(s)} \tag{6.15}$$

and using (2.70), (2.74), (3.61), and (3.71), we have

$$\xi_2 = \frac{N_0 - N_1}{N_0|r_{c0}'|} \tag{6.16}$$

and

$$\omega_2 = \frac{N_1 - N_0}{N_1}\omega_{cc} \tag{6.17}$$

Now the necessary conditions for freedom from gain constraint (Theorem 2) become:

(from the third condition, and from (3.66) which implies $\omega_{cc} > 0$)

$$\frac{N_1 - N_0}{N_1} > 0 \tag{6.18}$$

which implies $\xi_2 < 0$ (since, from (2.17) and (2.75), $\frac{N_0 |r'_{c0}|}{N_1} > 0$);

then the first condition gives:

$$\left(\frac{N_1}{N_0} - \frac{N'_1}{N'_0}\right) > 0 \tag{6.19}$$

and the second condition enforces the same constraint as the first. We will explore the consequences of these conditions for the optical design in more detail in Chapter 7.

6.2 System Performance

Let us now address the question of how much performance we sacrifice by operating with a poorly conditioned plant. Figure 6.6 shows a block diagram of the closed-loop system with d_1 and d_2 representing seismic disturbances driving the system away from perfect resonance and e_1 and e_2 the residual deviations from resonance in the presence of the servos.

Figure 6.6 Block diagram used to analyze performance, showing inputs driven by seismic disturbance.

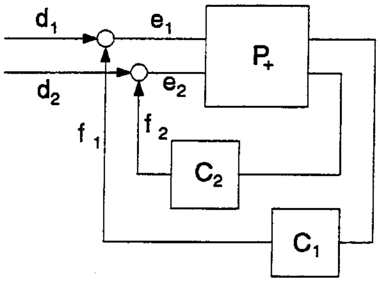

We solve for $\vec{e}$:

$$\vec{f} = CP_{+}\vec{e} \tag{6.20}$$

$$\vec{e} = \vec{d} + \vec{f} \tag{6.21}$$

$$\vec{e} = [1 - CP_{+}]^{-1}\vec{d} \tag{6.22}$$

If we let

$$S \equiv [1 - CP_{+}]^{-1} \tag{6.23}$$

then

$$e_2 = S_{21}d_1 + S_{22}d_2 \tag{6.24}$$

We will consider this term first.

The smaller e_2 is, the better a job our control system is doing. Clearly the larger we can make the elements of C, the better. In a real system there are always aspects of the high frequency performance of the system which limit the unity-gain frequency and thereby the gain one can achieve at those frequencies where one wants to suppress disturbances. In our system, assuming that it is not in a gain-constrained configuration, these high frequency features will be mechanical resonances at about 10 kHz for any loop driving a mirror, and propagation delays in the optical path and wiring, which produce significant phase delays

Figure 6.7 Block diagram showing plant and one feedback loop as a single block.

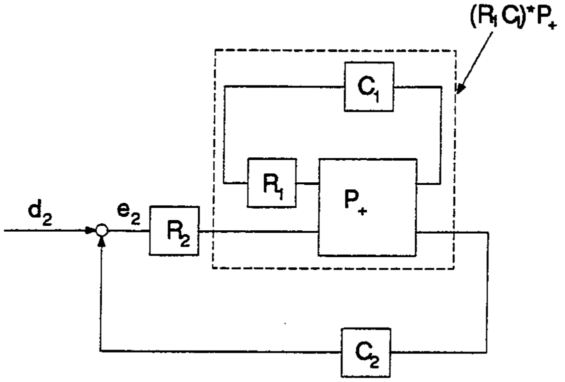

for frequencies exceeding about 1 MHz, for the loop feeding back to the laser. In Figure 6.7 these are shown explicitly as additional factors R_1 and R_2.[*]

When one of the outputs of the plant is connected back to one of its inputs via controller C_1 the resulting one-input, one output system[†]

$$(R_1C_1) * P_+ = C_2\left(\varepsilon_2 + \frac{\varepsilon_1 C_1}{1 - C_1}\right) \tag{6.25}$$

can be treated as a simple block from the point of view of analyzing loop 2. If we assume that $(R_1C_1) * P_+$ is smooth and minimum-phase in the frequency range where R_2 is smooth, then its exact frequency response is irrelevant since we can in principle cancel it by appropriate choice of frequency response of C_2. Then the minimum achievable value of S_{22} depends only on R_2, and, in particular, not on whether or not P_+ is diagonal. The other contribution to e_2 is $S_{21}d_1$, and we

---

[*] These factors have not been relevant until now because we model them as equalling unity at the frequencies where we want to suppress seismic noise, typically frequencies of less than 10 Hz.

[†] For brevity, we will write ε_1 and ε_2 instead of $\varepsilon_1(s)$ and $\varepsilon_2(s)$ throughout this section.

may ask how the size of this contribution compares to the other, since if we had a diagonal plant, this contribution would vanish. We can write S explicitly:

$$\begin{aligned} S &= [1 - CP_{+}]^{-1} \\ &= \frac{1}{\Delta}\begin{bmatrix} 1 - C_2\varepsilon_2 & C_1\varepsilon_1 \\ C_2 & 1 - C_1 \end{bmatrix} \end{aligned} \tag{6.26}$$

where

$$\Delta = 1 - C_1 - C_2\varepsilon_2 + C_1C_2(\varepsilon_2 - \varepsilon_1) \tag{6.27}$$

and see that

$$\frac{S_{21}}{S_{22}} = \frac{C_2}{1 - C_1} \tag{6.28}$$

In other words, the fact that our plant is not diagonal does not degrade performance significantly if

$$|C_2| \ll |1 - C_1| \tag{6.29}$$

A more useful expression can be derived by writing this in terms of the *loop gains,* G_1 and G_2:

$$\begin{aligned} G_1 &\equiv C_1(P_{+} * C_2) \\ &= C_1\left(1 + \frac{\varepsilon_1 C_2}{1 - C_2\varepsilon_2}\right) \\ &\simeq C_1\left(1 - \frac{\varepsilon_1}{\varepsilon_2}\right) \end{aligned} \tag{6.30}$$

where we have assumed that $|C_2\varepsilon_2| \gg 1$. Similarly

$$\begin{aligned} G_2 &\equiv C_2(C_1 * P_{+}) \\ &\simeq C_2(\varepsilon_2 - \varepsilon_1) \end{aligned} \tag{6.31}$$

and if $C_1 \gg 1$ we get the approximate result:

$$\left|\frac{S_{21}}{S_{22}}\right| = \left|\frac{G_2}{G_1\varepsilon_2}\right| \tag{6.32}$$

In other words, we do not sacrifice a significant amount of performance by adopting this scheme as long as G_1 is sufficiently large. The required ratio of G_1 to G_2 is $1/\varepsilon_2$; typically a few hundred*. This is easy to achieve for any reasonable loop shape in loop 2 since the unity gain limitations on loop 1 are so much less severe.

Next we look at loop 1 to see whether performance there is degraded. Here

$$e_1 = S_{11}d_1 + S_{12}d_2 \tag{6.33}$$

and the relevant ratio is

$$\begin{aligned}\left|\frac{S_{12}}{S_{11}}\right| &= \left|\frac{C_1}{1-\varepsilon_2 C_2}\right| \\ &\simeq \left|\frac{G_1\varepsilon_1}{G_2}\right|\end{aligned} \tag{6.34}$$

Since ε_1 is typically larger than ε_2, this means that as we increase G_1 we first start to experience a degradation in performance in loop 1† (over what it could have been with a diagonal plant) and then we stop experiencing any degradation in loop 2. One of the loops always experiences some degradation. In the numerical analysis presented later in this chapter, G_1 is very large, so that the performance

---

[*] In our numerical example, $\varepsilon_1 \simeq 0.0043$ and $\varepsilon_2 \simeq -0.0016$.

[†] The performance in loop 1 does not become worse as we increase G_1; it just ceases to improve. If we had a diagonal plant, the performance in this loop would continue to improve as we increased the gain.

in loop 1 is not as good as it would be with a diagonal plant. Nonetheless, according to the predictions of this numerical analysis, adequate performance can be achieved in both loops. If the specs on loop 1 were much tighter or if we found that we had trouble meeting them, then we might want to consider using a different signal extraction scheme or implementing a "decoding matrix" to improve the performance in loop 1.

A decoding matrix is a set of amplifiers interconnected so as to form a 2x2 system which, when connected to the outputs of P_+, produces a new plant, say

$$\tilde{P}_+ = \begin{bmatrix} 1 & \tilde{\varepsilon}_1 \\ 1 & \tilde{\varepsilon}_2 \end{bmatrix} \tag{6.35}$$

For an ideal decoding matrix, $\tilde{P}_+$ would be nearly diagonal (i.e., $\tilde{\varepsilon}_1 \simeq 0$ and $\tilde{\varepsilon}_2 \simeq \infty$). Under these circumstances the noise injected into either loop by the other would become negligible. For a more realistic decoding matrix all of the relations between the matrix P_+ and stability and performance derived above apply equally to $\tilde{P}_+$, and performance can be improved if the new plant is more nearly diagonal than the original plant. When analyzing such a system, it is especially important to consider the imperfections in the components used to build the electronic decoding matrix, and possible fluctuations in the interferometer response, due to misalignment or deviations from resonance. The design of an ideal decoding matrix would be straight forward if one had ideal electronic components and a non-varying interferometer response; a real device with imperfections may yield smaller performance benefits.

6.3 Numerical Example of a Control System Design

Mainly for the sake of illustrating some of the ideas developed above, a controller was designed and evaluated numerically[*]. The design was done by trial and error. Poles and zeros were added to the controller and their frequencies changed until adequate performance was achieved and all of the constraints satisfied. The poles and zeros of the final design[†][26], as well as the performance predicted for this design, are shown in Table 6.1.

Simple numerical models were used to represent the plant and the controller. For the plant, the rational function approximation derived in Chapter 3 was used; for the controller, a rational function (pole/zero) representation was used. Thus the numerical model did not contain the effect of internal resonances in the mirrors, nor the effect of propagation delays. That these unmodeled effects would not cause instability in a real system was checked by inspection during the design process.

---

[*] Almost all of the analysis described in this section was done using Matlab® code.

[†] L. Sievers first observed that adequate performance could be achieved, and all of the design constraints satisfied, with controllers containing only real poles and zeros (i.e., no complex conjugate pairs of poles or zeros).

Constraints

Stability As mentioned above, a mirror resonance could cause instability if the loop gain at the resonant frequency were to exceed unity. Since the resonances are expected to have quality factors of up to 10^7 and are expected to occur at frequencies as low as 10 kHz[27], this type of instability was ruled out by assuring that the magnitude of the loop gain in any of the loops driving a mirror was less than 10^{-7} at frequencies exceeding 10 kHz[*][28].

In the loop feeding back to the laser frequency the criterion was simply that the unity gain frequency be less than 1 MHz. At that frequency 80 ns of delay (corresponding to 24 m of optical path), together with 15 degrees of phase change seen in the high frequency interferometer response (H_11 of Figure 4.2), still leaves a phase margin of up to 70 degrees.

The simplified rational function model of the closed loop system could also be unstable by itself. This was checked by finding the eigenvalues of the "A" matrix in the state-space representation[†] of the closed-loop system, to make sure that their real parts were positive.

Noise One additional constraint was observed during the design. As we saw in Chapters 2 and 3, the gravitational wave output, in addition to being sensitive to

---

[*] A Mathematica program was written to check this particular constraint. This was necessary because the Matlab® code, using the state-space formalism, underestimated the attenuation at high frequencies.

[†] The (Matlab®) software used to do this part of the analysis and design does all of its calculations in state space.

Φ_-, is also sensitive to ϕ_-. If ϕ_- is controlled by a loop containing a noisy sensor, then the induced noise in ϕ_- will contaminate the gravitational wave signal[*].

Quantitatively, we require, at frequencies where we want interferometer performance to be limited only by shot noise at the antisymmetric output (above 100 Hz),

$$|\varepsilon_3|\left[S_{\phi_-}^{\frac{1}{2}}(f)\right]\left|\frac{G_{\phi_-}}{1+G_{\phi_-}}\right| \ll S_{\Phi_-}^{\frac{1}{2}}(f) \tag{6.36}$$

where $S_{\phi_-}^{\frac{1}{2}}(f)$ and $S_{\Phi_-}^{\frac{1}{2}}(f)$ are the shot-noise limited sensitivity to ϕ_- at the isolator and to Φ_- at the antisymmetric output, and G_{ϕ_-} is the open-loop gain in the ϕ_- loop. In our numerical example, this corresponds to

$$G_{\phi_-} \ll 0.1 \tag{6.37}$$

and we use $G_{\phi_-} < 0.01$ as our constraint.

Performance

Figure 6.8 shows the expected seismic disturbance driving each of the interferometer mirrors[†][29]. To calculate the rms deviation from resonance, this spectrum is first multiplied by a number M_k corresponding to the number of mirrors being

---

[*] In principle, this noise, being separately measurable in the ϕ_- loop, could be subtracted out of the gravitational wave signal. However, the precision with which this can be done is limited by practical considerations, and the additional complexity is undesirable.

[†] This curve was calculated from a combination of estimated and measured spectra of the seismic motion, and from the transfer functions of the mechanical anti-seismic isolation.

perturbed, and multiplied at each frequency by the closed loop gain of the system. This set of operations is represented diagrammatically in Figure 6.9. This produces the spectrum of residual deviations, which is then squared, integrated, and raised to the power of 1/2.

Figure 6.8 Seismic spectrum.

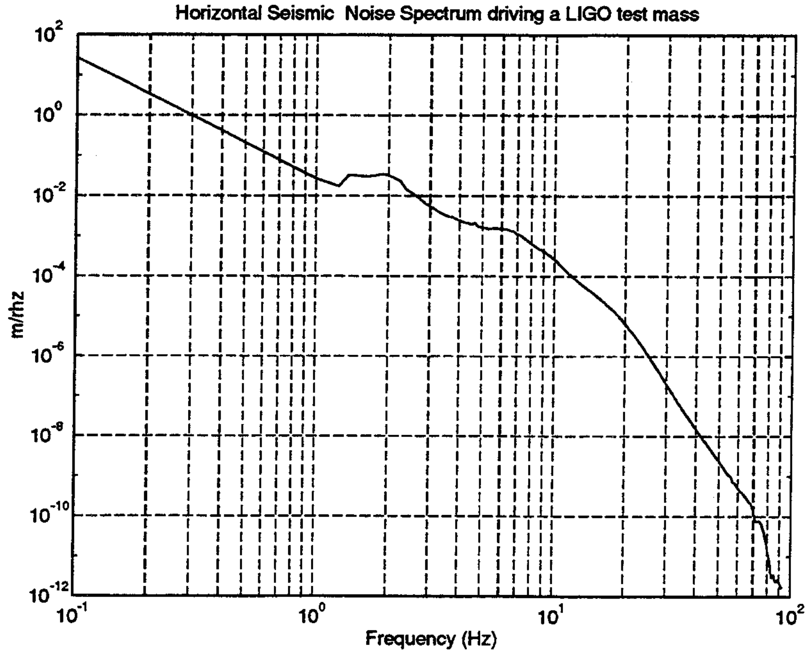

Figure 6.10 shows the magnitude of the open-loop gains, and the spectra of residual motion for the common-mode degrees of freedom. We see that the ratio of open loop gains easily exceeds $1/\varepsilon_2$ at all frequencies where the seismic disturbance is significant, and, as expected, the residual deviations are due mainly to the disturbance input in loop 2. This is illustrated by Figure 6.11, which shows

Figure 6.9 Block diagram for the propagation of seismic disturbance.

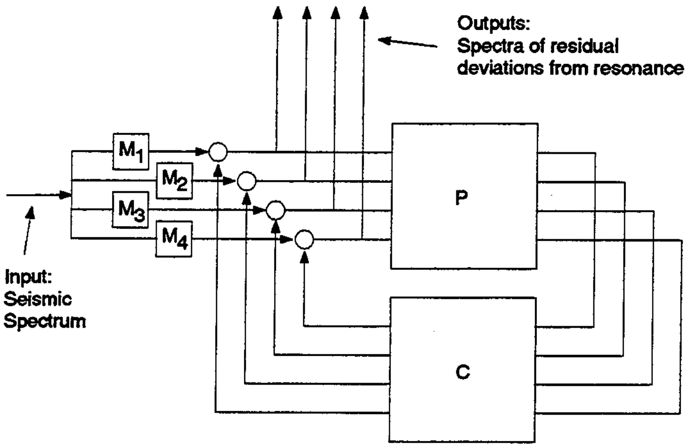

the contributions to the residual deviations in loop 1 and loop 2, due to seismic disturbances entering loops 1 and 2.

Finally we note that although the performance specifications set forth in Chapter 1 and Appendix B were only barely met in this design, considerable improvements are possible at the cost of modest additional complexity. In loops 2 and 3, which are limited in bandwidth by mirror resonances, gain increases can be achieved by installing notch filters in these loops, to partially cancel the effects of the resonances. The gain in loop 4 can be increased without contaminating the gravitational-wave output if subtraction circuitry is installed to re-subtract the noise introduced by this loop from the gravitational-wave output.

Figure 6.10 Loop gains (a)) and residual motion (b)) in common-mode degrees of freedom. Curves corresponding to the ϕ_+ loop are dashed.

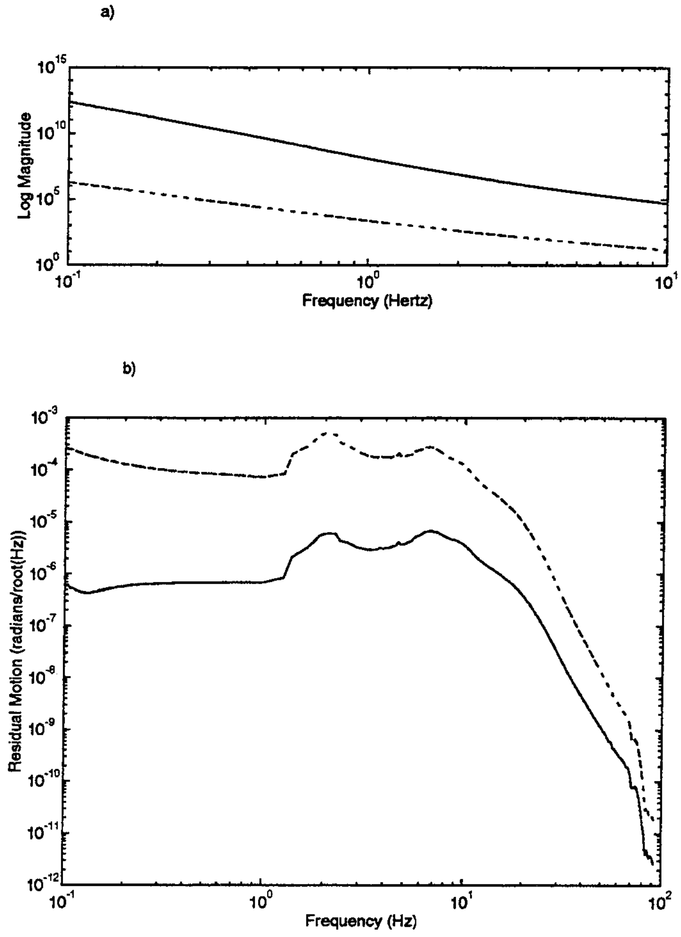

Figure 6.11 Contributions from loop 1 and loop 2 (dashed) to residual deviations from resonance in loop 1 (a) and in loop 2 (b).

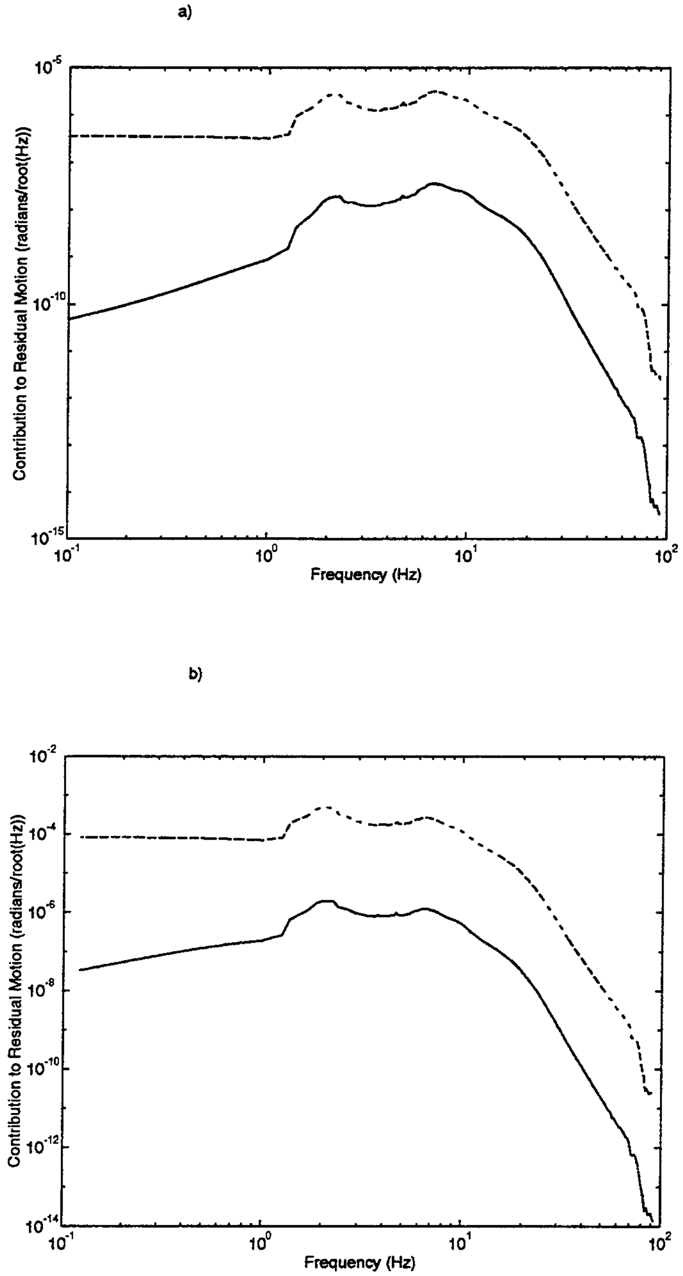

Table 6.1 Loop shapes and performance predictions for numerical servo design.

		pole frequencies (Hz)	zero frequencies (Hz)	Unity-gain frequency	Performance (RMS residual deviation, radians)
Degree of Freedom	Φ_+	0.0016, 3 at 0.016	1.6, 1.6, 16, 16,	300 kHz	7.3×10^{-6}
	ϕ_+	0.0016, 2 at 0.016 4 at 3000	1.6, 16	70 Hz	7.2×10^{-4}
	Φ_-	3 at 0.016 4 at 3000	92, 16, 16	60 Hz	3.8×10^{-4}
	ϕ_-	2 at 0.0016, 30, 30	3	9 Hz	2.5×10^{-2}

Chapter 7 Optical Design Considerations

In previous chapters, a number of somewhat arbitrary choices of optical parameters and layout have been made. In this chapter we will investigate the motivation behind some of those choices. In particular, we will consider the choice of common-mode feedback configuration, of asymmetry, of recycling mirror reflectivity, and of modulation depth.

7.1 Common-mode Feedback Configuration

In Figure 1.7 we showed the feedback to the laser frequency coming from the isolator inphase output and the feedback to the recycling mirror position from the pick-off inphase output. In principle one could reverse these connections for some optical configurations. One compelling reason to feed back to the laser frequency with v_1 is that the shot-noise limited sensitivity to Φ_+, is better in v_1 than in v_2 (typically by a factor of about 30). Since we insist on high gain in this loop, any sensing noise in this loop will be impressed on the laser frequency[*]. This noise can be measured, and it could in principle be subtracted out of the gravitational wave signal, but this is technically difficult, and would require a separate low-noise frequency reference[†].

---

[*] Although the gravitational wave output of an ideal interferometer is insensitive to v_1, a small asymmetry in the arm cavities can compromise this common-mode rejection.

[†] The currently proposed mode cleaner (see footnote, page 8) is almost quiet enough, and could be made sufficiently quiet by narrowing its bandwidth.

7.2 Asymmetry

An immediate consequence of this choice of feedback configuration is that (according to (6.18)) avoiding gain constraint will require

$$\frac{N_1 - N_0}{N_1} > 0 \tag{7.1}$$

which implies (using (2.71) and (2.75))

$$\cos\alpha > r_{c0} \tag{7.2}$$

A number of other aspects of interferometer behavior are affected by the value we choose for the asymmetry δ. One of these is the shot-noise limited sensitivity in v_3 to Φ_-, the gravitational wave signal:

$$S^{\frac{1}{2}}_{\Phi_-}(f) \equiv \frac{\sqrt{\overline{S_{v_3v_3}}(f)}}{H_{v_3\Phi_-}(i2\pi f)} \tag{7.3}$$

where

$$\overline{S_{v_3v_3}}(f) = |E_{excess}|^2 + 3|E_{anti\ 1}|^2 \tag{7.4}$$

and

$$H_{v_3\Phi_-} = E_l^2 J_0(\Gamma) J_1(\Gamma) \left(\frac{E_{r\ 0}}{E_{inc\ 0}}\right)\left(\frac{E_{anti\ 1}}{E_{inc\ 1}}\right) t_p r'_{c0} \tag{7.5}$$

The above expression is complicated and its optimization is usually done numerically. However, δ affects only the term $3|E_{anti\ 1}|^2$ in the numerator and $\left(\frac{E_{anti\ 1}}{E_{inc\ 1}}\right)$ in the denominator. The numerator increases with $E_{anti\ 1}$ more slowly than does the denominator, so increasing $\left(\frac{E_{anti\,1}}{E_{inc\,1}}\right)$ improves the shot-noise limited sensitivity to Φ_-. Now

$$\left(\frac{E_{anti\,1}}{E_{inc\,1}}\right) \propto \frac{\sin\alpha}{1 - r_R T_p \cos\alpha} \tag{7.6}$$

is maximum when

$$\cos\alpha = r_R T_p \tag{7.7}$$

which corresponds to $\alpha \simeq 0.2$ in our numerical example. However, the following considerations motivate us to choose a smaller value for α:

1. The vacuum envelope must be able to accommodate the test mass positions corresponding to the desired asymmetry. This may be easier with a smaller value of δ.
2. The shot-noise limited sensitivity to Φ_+ in v_1 is degraded if the amount of sideband reflected from the recycling mirror $\left(\frac{E_{ref\,1}}{E_{inc\,1}}\right)$ is too small. From (2.77) we can see that in fact the signal will vanish when $\left(\frac{E_{ref\,1}}{E_{inc\,1}}\right) = 0$, which happens when $\cos\alpha = \frac{r_R}{T_p}$, a value uncomfortably close to the value in (7.7) above.
3. As mentioned above, if we wish to be free from gain constraint, we must choose $\cos\alpha > r_{c0}$; moreover, we will see in the next section that we wish to choose $r_R \simeq r_{c0}$, so again this motivates the use of a smaller value of α.
4. The shot-noise limited sensitivity to Φ_- is quite a weak function[‡] of α. This

---

[‡] A numerical survey over a large range of values for contrast defect, recycling mirror transmission and losses showed that the shot noise limited sensitivity to gravitational waves was degraded by at most 5% when α was reduced to 0.15.

is because a lack of efficiency in transmission to the antisymmetric port can be partially compensated by an increase in the modulation index.

From the above arguments we conclude that the choice of α is not critical, and we choose one which is roughly 75% of the value which would give optimum shot noise performance.

7.3 Recycling Mirror Reflectivity

The recycling factor (see footnote, page 26) is maximum for $r_R = T_p r_{c0}$, and we would like to operate as close as possible to this value. Before choosing r_R we will make sure that condition (6.19) is not violated.

$$\frac{N_1}{N_0} - \frac{N_1'}{N_0'} > 0 \tag{7.8}$$

implies

$$\left(1 - \frac{r_R - T_p r_{c0}}{r_R - T_p \cos\alpha}\right) > 0 \tag{7.9}$$

which is satisfied if

$$\cos\alpha > r_{c0} \tag{7.10}$$

But we have already chosen to satisfy this in Section 7.2, in order to achieve $\omega_2 > 0$ (no right-half-plane zero in $H_{v_2\phi_+}(s)$). We are free to choose any recycling mirror reflectivity we want. It is interesting to note that this would not be the case were we to demand that $H_{v_1\phi_+}(s)$ also be free of right-half-plane zeros.

7.4 Modulation Index

The shot noise limited gravitational wave sensitivity of the instrument is a relatively sensitive function of the modulation index Γ, especially if E_{excess} is large, and for large E_{excess} the optimum value of Γ is also large. For large Γ the approximation (2.2) is no longer valid, and one needs to add (at least) an additional pair of terms:

$$E_{inc} \simeq E_l\Big(J_0(\Gamma) + J_1(\Gamma)\Big(ie^{i\Omega t} + ie^{-i\Omega t}\Big) - J_2(\Gamma)\Big(e^{i2\Omega t} + e^{-i2\Omega t}\Big)\Big) \quad (7.11)$$

We call the frequency components separated from the optical carrier by 2Ω *second-order RF sidebands*; they are reflected almost perfectly from the recycling mirror

$$\left(\frac{E_{ref\,2}}{E_{inc\,2}}\right) \simeq 1 \quad (7.12)$$

since (by design)* they do not resonate in the arm cavities nor in the recycling cavity. They are capable of beating against the first-order RF sidebands to create a signal at the mixer output. Generalizing (2.4):

$$v_I = Re\{E_{-2}^* E_{-1} + E_{-1}^* E_0 + E_0^* E_1 + E_1^* E_2\} \quad (7.13)$$

If $E_{-2} = E_2$ and these fields as well as E_0 are real, and if $E_{-1} = E_1$ then

$$v_I = 2Re\{E_1(E_0 + E_2)\} \quad (7.14)$$

The fields at the isolator satisfy these conditions, and the above explanation holds for v_1, the inphase signal at the isolator. We see that the signal generated in v_1

---

* See footnote page 27.

when the carrier phase changes is unaffected by the presence of the second-order sidebands, so that $H_{v_1\Phi_+}(s)$ is unaffected by the presence of the second-order RF sidebands. The contribution to $H_{v_1\phi_+}(s)$ due to the change in phase of the first-order sidebands is affected, however; the size of this contribution changes by a factor[*]

$$\frac{E_0 + E_2}{E_0} = 1 + \frac{E_{ref\,2}}{E_{ref\,0}} \tag{7.15}$$

This contribution remains frequency independent, since the signal is due to audio sidebands on the first-order RF sidebands, and we account for it by defining $\tilde{N}_1 \equiv \left(1 + \frac{E_{ref\,2}}{E_{ref\,0}}\right) N_1'$ and replacing N_1' by $\tilde{N}_1$ in all of our formulae. In particular, (7.9) becomes

$$\frac{r_R - T_p r_{c0}}{r_R - T_p \cos\alpha} \left(1 + \frac{E_{ref\,2}}{E_{ref\,0}}\right) < 1 \tag{7.16}$$

Using (7.11), (7.12) and (2.38), we find

$$\frac{E_{ref\,2}}{E_{ref\,0}} \simeq -\frac{J_2(\Gamma)}{J_0(\Gamma)} \frac{1 - r_R T_p r_{c0}}{r_R - T_p r_{c0}} \tag{7.17}$$

Now if (motivated by the arguments in Section 7.2) we have $r_R - T_p \cos\alpha < 0$ then regardless of whether $r_R - T_p r_{c0}$ is positive or negative[†], (7.16) is harder to satisfy than (7.10).

---

[*] The fields E_2 and E_{-2} are unaffected by the phases in the interferometer since they do not resonate in it.

[†] These two cases correspond to having the carrier be "undercoupled" or "overcoupled," respectively, at the recycling mirror.

A sufficient condition for this effect to be small is

$$\frac{E_{ref\ 2}}{E_{ref\ 0}} \simeq \frac{-J_2(\Gamma)}{J_0(\Gamma)\frac{r_R - T_p r_{c0}}{1 - r_R T_p r_{c0}}} \ll 1 \tag{7.18}$$

or

$$J_2(\Gamma) \ll \left| \frac{r_R - T_p r_{c0}}{1 - r_R T_p r_{c0}} \right| \tag{7.19}$$

This effect of the second-order RF sidebands is inconvenient because it implies that the frequency response of the interferometer depends on modulation index. Increasing the modulation index to optimize the sensitivity will require not only adjusting the servo gains to compensate for the change in overall response, but will carry a risk of significantly degrading the control system performance.

One solution, although itself inconvenient, is to amplitude modulate the beam at 2Ω before or after the phase modulation occurs[‡]. If properly tuned, the sidebands applied this way will exactly cancel those due to the phase modulation.

Another potential solution is to arrange the arm cavity lengths so that the second-order RF sidebands are exactly resonant in the arm cavities. This possibility has not been investigated in any detail.

[‡] If an electro-optic modulator is used as the power-stabilizing feedback element, then a convenient and power-efficient way to apply this modulation will be to insert an additional crystal driven at 2Ω between the polarizers, or to sum the power stabilizer and 2Ω signals electronically before applying them. A stand-alone amplitude modulator is power-inefficient because the beam must be attenuated to some extent for the modulator response to be quasi-linear.

7.5 Arm Cavity and Recycling Cavity Lengths

The arm cavity length which is easiest to analyze is one for which the first-order RF sidebands are exactly antiresonant, i.e., a length of $\left(n+\frac{1}{2}\right)\frac{\lambda_{mod}}{2}$ with n a whole number. In this case the sidebands experience no phase change upon reflection from the arm cavities and the average length of the recycling cavity is chosen to be $\left(m+\frac{1}{2}\right)\frac{\lambda_{mod}}{2}$. Then when the carrier resonates in all three cavities, the sidebands resonate only in the recycling cavity[30]. This configuration has the disadvantage that it allows the second-order RF sidebands to resonate in all three cavities as well, making the response of the interferometer harder to understand, and very sensitive to small deviations from these design lengths. For this reason, in our numerical example the arm cavity lengths were chosen to be slightly different from those which would make the first-order RF sidebands exactly antiresonant.

It is also possible to use virtually arbitrary arm cavity lengths, so long as the first-order RF sidebands do not resonate[§][||] in the arm cavities. However, if the sidebands are far from being antiresonant in either arm, then they will experience significant phase changes upon reflection from that arm, and the average recycling cavity length as well as the asymmetry must be adjusted to compensate for this phase.

[§] If the sidebands resonate in the arm cavities, then the RF sideband phase becomes quite sensitive to Φ_+ and the plant becomes more ill-conditioned.

[||] To avoid an exaggerated sensitivity to alignment it is also important to avoid allowing the sidebands to fall onto the resonant frequency of other low-order transverse modes.

Chapter 8 Summary and Conclusion

When the system for extracting signals described herein was first conceived, a number of concerns existed about whether the asymmetric layout would fit into the proposed vacuum system, whether the asymmetry would cause excessive losses because of the different mode-matching demands imposed by the two arms[#][31], how the system would respond to imperfections in the optical components or in their alignment, and whether it would be possible to acquire lock with such a system. In addition, it was unclear whether the fact that two of the outputs are proportional to barely independent linear combinations of two of the degrees of freedom (that the plant is ill-conditioned) would prove to be a formidable technical problem.

Since then, a number of these issues have become better understood. An experimental prototype has demonstrated that, at least for a particular set of optical parameters, the assumptions made in constructing interferometer models have been reasonable. The issue of whether it is possible to control the ill-conditioned system adequately has been resolved. The performance sacrifices involved are understood, and the construction of a working prototype is further evidence that this problem is not critical. The dynamics of the interferometer are also believed fairly well understood. The approximate results from a simple analysis agree well with an independently assembled numerical model, and both predict behavior

---

[#] A. Abramovici has since shown that this effect is completely negligible.

which is simple enough not to require additional complexity from the controller. Optical configurations corresponding to a plant which is hard to control have been identified, and are easily avoided.

Other issues remain less well settled. The following sections describe a number of such issues.

8.1 Robustness

Although the prototype interferometer described in chapter 5 showed, for one geometry and set of optical parameters, that the system is not dangerously sensitive to imperfections, very little was done to quantify the magnitude of the imperfections existing there, and in any case, it would be difficult to make predictions for the behavior of a full-sized interferometer this way. In its full generality, the issue of interferometer behavior in the presence of imperfections is very complicated. However, with a combination of analysis of imperfections perceived as likely to cause trouble, and careful prototyping, the risk that an important problem may surface very late can be reduced. One area which remains largely unexplored concerns robustness. This is loosely defined as the ability of a control system to maintain good performance in the presence of various imperfections. These imperfections can include differences between actual and ideal mirror reflectivities, misalignment, imperfections in electronic components, and even the effect on the interferometer response of deviations from resonance.

Both experimental prototyping and numerical analysis are powerful methods for testing robustness. The former automatically tests for the simultaneous effect of a large number of imperfections, whereas the latter permits a carefully controlled calculation of the effect of a relatively small number of imperfections. The system presented herein may merit some additional numerical investigation before the next stage of prototyping is attempted. Some types of imperfections, which are likely both to occur and to affect system performance, are listed below.

Beam Splitter Reflectivity

Even with today's best coating techniques it is difficult to produce a beam splitter having a reflectivity differing by less than about 5% from the specified value of 50%. Consequently the RF sidebands sample the lengths l_I and l_P in different proportions; the effective average recycling cavity length and the effective asymmetry δ are both affected. The effect of an asymmetric beam splitter can be partly cancelled[32] by an appropriate modification of l_I and l_P; this has been checked in a limited number of numerical tests.

Mixer Phase Error

In our model each mixer is driven by a local oscillator signal which is either exactly in phase with the phase modulating signal or exactly in quadrature phase. In a real interferometer, these phases will be affected by propagation delays in the optical beam path, in cables, and in circuitry. The output v_4 is particularly vulnerable to this type of phase error because the inphase signal at the same photodetector is more sensitive to Φ_+ and to ϕ_+ than the quadrature phase is to ϕ_-. In our numerical example the performance in loop 4 is not significantly degraded even for a mixer phase error as large as 20 degrees (the derivation of this result is in Appendix D). Future design changes could however reduce the tolerance to this type of error.

Changes in Interferometer Response due to Deviations from Resonance

For arbitrary positions of the interferometer mirrors, the output signals are non-linear functions of these positions[**] and any substantial deviation from resonance can cause the interferometer response to further small mirror displacements to be changed. This change in response can affect the performance of the control system, allowing even larger deviations to occur. This mutual dependence of control system performance and interferometer response makes this a difficult problem to analyze, and further protoyping may be the most effective approach. A preliminary numerical exploration was done to see how the matrix of derivatives (of chapters 2 and 4) is affected by a few selected types of deviation from resonance. The magnitude of the deviations explored was comparable to the deviations permitted within the specifications of Appendix B. It was found that for deviations in ϕ_+ alone there was no significant change in the matrix, for si-

---

[**] For example, the outputs are periodic in the round-trip phases.

multaneous changes in ϕ_+ and ϕ_- or in ϕ_+ and Φ_-, the matrix changed, but the diagonal elements changed by less than 10%, and each off-diagonal elements changed by less than 10% of the diagonal element in the same row. It remains to be seen how these changes in the plant matrix would affect performance and whether other combinations of deviations from resonance will have more serious effects on the plant matrix.

8.2 Lock Acquisition

When the laser and control electronics for an interferometer are first switched on, the mirrors are in essentially arbitrary positions, and, for an interferometer with suspended components, moving with a wide range of velocities. In this situation, the interferometer output signals are non-linear functions of the mirror positions and of the laser frequency. When the interferometer is locked, the mirrors and laser frequency are not allowed to deviate except very slightly from resonance, and, to a good approximation, the signals at the output are related to the mirror positions and laser frequency by a (linear) matrix of transfer functions. The transition from the former "out-of-lock" state to the locked state is difficult to analyze because of the non-linear response of the system in the out-of-lock state. Low-order systems have been analyzed[33,34], but the generalization to higher order or multi-dimensional systems is not obvious.

It is in principle possible to model the out-of-lock state numerically in the time domain, and this has been done with limited success for a servo loop controlling a simple Fabry-Perot cavity*. The algorithms used are computationally intensive and a thorough exploration of initial-value space for a complete interferometer will require a large amount of computer time. Model development is also time-consuming because few analytic or experimental results exist to confirm or refute any numerical result.

8.3 Conclusion

In addition to modeling efforts which will likely continue for some time, an important next step in the development of this signal extraction and control system will be prototyping in the 40m interferometer on the Caltech campus. In two important respects, this instrument is much more like a LIGO interferometer than the tabletop prototype described herein. The mirrors are suspended, and the losses and lengths are such that the optical dynamics occur much more slowly. The fact that the mirrors are suspended means that the spectrum of the seismic noise to be suppressed is quite similar to that in LIGO. The fact that the dynamics are slower will make it possible to measure the response to mirror motion for comparison with the numerical and analytic models.

---

* A program called Simulink® was used. Simulink® is a trademark of The MathWorks, Inc.

Cited References

[1] R. Weiss, *Quarterly Progress Report of the Research Laboratory of Electronics of the Massachusetts Institute of Technology*, **105**, 54, (1972).

[2] R. Forward, *Phys. Rev. D*, **17,** 379, (1978).

[3] A. Abramovici, W.E. Althouse, R.W.P. Drever, Y. Gursel, S. Kawamura, F.J. Raab, D. Shoemaker, L. Sievers, R.E. Spero, K.S. Thorne, R.E. Vogt, R. Weiss, S.E. Whitcomb, and M.E. Zucker,*Science* **256,**325, (1992).

[4] R. Weiss, *Quarterly Progress Report of the Research Laboratory of Electronics of the Massachusetts Institute of Technology*, **105**, 54, (1972).

[5] R. W. P. Drever, G. M. Ford, J. Hough, I. M. Kerr, A. J. Munley, J. R. Pugh, N. A. Robertson, and H. Ward, “A Gravity-Wave Detector Using Optical Cavity Sensing,” 9th International Conference on General Relativity and Gravitation at Jena, GDR, (1980).

[6] R. W. P. Drever, in *Gravitational Radiation,* ed. N Deruelle and T. Piran, North Holland, Amsterdam, (1983), p. 321.

[7] L. Schnupp, unpublished, (1986), describes the use of a similar scheme for the extraction of the gravitational-wave signal from a recycled Michelson interferometer.

[8] R. W. P. Drever (unpublished) suggested the adaptation of L. Schnupp’s scheme to a recycled Michelson interferometer with Fabry-Perot arms (1991).

[9] S. Whitcomb (private communication) realized that the scheme could be used to sense all of the critical degrees of freedom (1991).

[10] A. Yariv, *Optical Electronics*, 4th ed. Saunders College Publishing, Philadelphia, (1991), p. 331.

[11] J. W. Goodman, *Introduction to Fourier Optics,* McGraw-Hill, New York (1968), p. 9.

[12] Z.Y. Ou and L. Mandel, *Am. J. Phys.* **57** ,66, (1989).

[13] Y. Gursel, P. Lindsay, P. Saulson, R. Spero, R. Weiss and S. Whitcomb, *The response of a Free Mass Gravitational Wave Antenna,* LIGO internal document, (1983).

[14] J. P. Monchalin and R. Heon, *Appl. Phys. Lett.,* **55,** 1612, (1989).

[15] B. J. Meers, *Phys. Lett. A,* **142,** 465, (1989).

[16] B. J. Meers, *Phys. Lett. A,* **142,** 465, (1989).

[17] P. Fritschel, "Techniques for Laser Interferometer Gravitational Wave Detectors," MIT Ph.D. Thesis, (1992).

[18] P. Fritschel, "Techniques for Laser Interferometer Gravitational Wave Detectors," MIT Ph.D. Thesis, (1992).

[19] P. Fritschel, D. Shoemaker, R. Weiss, *Appl. Optics,* **31,** 1412, (1992).

[20] D. Shoemaker, P. Fritschel, J. Giaime, N. Christensen, R. Weiss, *Appl. Optics,* **30,** 3133, (1991).

[21] J. M. Maciejowski, *Multivariable Feedback Design.* Addison-Wesley, Reading (1989), p 27.

[22] M. Morari, and E. Zafiriou, *Robust Process Control.* Prentice-Hall, Englewood Cliffs, (1989), pp. 339ff.

[23] D. Shoemaker and R. Weiss, *Analysis of an Externally Modulated Recycled Interferometer,* internal LIGO document (1992).

[24] Morari, M. and Zafiriou, E., *Robust Process Control,*Prentice-Hall, Englewood Cliffs, (1989), p 220.

[25] G. J. Thaler and R. G. Brown, *Servomechanism Analysis.* McGraw-Hill, New York, (1953), pp 149–151.

[26] L. Sievers, private communication, (1994).

[27] A. Gillespie, private communication, (1993).

[28] T. Lyons, private communication (1994).

[29] L. Sievers, private communication (1994).

[30] P. Fritschel, "Techniques for Laser Interferometer Gravitational Wave Detectors," MIT Ph.D. Thesis, (1992).

[31] A. Abramovici, private communication, (1991).

[32] S. Whitcomb, private communication, (1991).

[33] F. M. Gardner, *Phaselock Techniques.* Wiley, New York, (1979).

[34] A. J. Viterbi, *Principles of Coherent Communications.* McGraw-Hill, New York, (1966).

Appendix A Shot Noise at the Mixer Output

To quantify the noise performance of an instrument, we must somehow characterize the random process $\mathbf{x}(t)$ corresponding to the output in the absence of any signal. For stationary noise, this is most conveniently done using the one-sided power spectrum $S_{xx}(f)$ of $\mathbf{x}(t)$, defined as the Fourier transform of the autocorrelation $R_{xx}(\tau)$ of $\mathbf{x}(t)$:

$$R_{xx}(\tau) = E\{\mathbf{x}(t+\tau)\mathbf{x}(t)\} \tag{A.1}$$

$$S_{xx}(f) = 2\int_{-\infty}^{\infty} R_{xx}(\tau)e^{2\pi i f\tau}d\tau \tag{A.2}$$

$$R_{xx}(\tau) = \int_{0}^{\infty} S_{xx}(f)\cos 2\pi f\tau \, df \tag{A.3}$$

(As in the widely-used text by Papoulis[1] we use boldfaced symbols for random variables and the notation $E\{\}$ to mean expectation value or ensemble average.) The reason that this is a useful way to characterize the noise is that if $\mathbf{x}(t)$ is the input of a linear system $H(f)$, and $\mathbf{y}(t)$ its output, then

$$S_{yy}(f) = |H(f)|^2 S_{xx}(f) \tag{A.4}$$

and

$$E\left\{\mathbf{y}(t)^2\right\} = R_{yy}(0) = \int_0^\infty S_{yy}(f)df = \int_0^\infty |H(f)|^2 S_{xx}(f)df \tag{A.5}$$

Now if, for example, $H(\omega)$ were an ideal "brickwall" bandpass filter (one which passes frequencies within the bandpass unattenuated but attenuates out of band frequencies infinitely) with passband $[f_1, f_2]$ in an ideal spectrum analyzer, then the expected power out of that filter (expected power "in that frequency band") would be

$$\int_0^\infty S_{yy}(f)\,df = \int_{f_1}^{f_2} S_{xx}(f)\,df \,. \tag{A.6}$$

The output $\mathbf{i_o}(t)$ of our model, in the absence of signal, is not stationary since the photocurrent fluctuates at twice the modulation frequency and since it is then demodulated at the modulation frequency. Similar problems to this have been analyzed previously[2,3]. Neither of these solutions was derived within the formalism of Papoulis's text, and a re-derivation in this more standard language is useful.

We note that $\mathbf{i_o}(t)$ is cyclostationary; for any t_0 the statistics of $\mathbf{i_o}(t_0)$ are the same as those of $\mathbf{i_o}(t_0+T)$ where T is the period of the modulation. Consequently, the autocorrelation $R_{i_o i_o}(t+\tau, t) = E\{\mathbf{i_o}(t+\tau)\mathbf{i_o}(t)\}$ is also periodic in t. For an arbitrary cyclostationary process $\mathbf{x}(t)$ with period T, if we define an average autocorrelation

$$\overline{R_{xx}}(\tau) = \frac{1}{T} \int_{t}^{t+T} R_{xx}(t' + \tau, t')dt' , \tag{A.7}$$

and its Fourier transform, the average power spectrum

$$\overline{S_{xx}}(f) = 2 \int_{-\infty}^{\infty} \overline{R_{xx}}(\tau) e^{2\pi i f \tau} d\tau , \tag{A.8}$$

then the latter also has the important properties ascribed to $S_{xx}(f)$ above[4]. Now, if $\mathbf{y}(t)$ is again the output of a linear system $H(f)$ to which $\mathbf{x}(t)$ is the input, then $\overline{R_{yy}}(0)$ has the significance of being the time average (over the period T) of the variance of $\mathbf{y}(t)$. In the example of the spectrum analyzer, we expect the power at the output of our filter to fluctuate with period T, but the average of the expected power over an integral number of periods is given by $\overline{R_{yy}}(0)$.

Our goal is to calculate $\overline{S_{v_I v_I}}(f)$ and $\overline{S_{v_Q v_Q}}(f)$, the average power spectrum of the signal at the mixer output. In Chapter 2 we modeled the mixer as being a device which multiplies by $\cos \Omega t$ or by $\sin \Omega t$ and then averages over some time interval T, and for convenience we chose T to be an integral multiple of the modulation period. We begin by defining $i_I \equiv i_p \cos \Omega t$ and $i_Q \equiv i_p \sin \Omega t$ to be the signal after multiplication by the appropriate sinusoid but before low-pass filtering, and finding $\overline{S_{i_I i_I}}(f)$ and $\overline{S_{i_Q i_Q}}(f)$.

To calculate $\overline{R_{i_I i_I}}(\tau)$, we first find the expected photodetector signal $i_p(t)$:

$$
\begin{aligned}
i_p(t) &= \left|E_0 + E_1 e^{i\Omega t} + E_{-1} e^{-i\Omega t}\right|^2 \\
&= |E_0|^2 + |E_1|^2 + |E_{-1}|^2 \\
&+ 2Re\left\{E_0^* E_1 e^{i\Omega t} + E_{-1}^* E_0 e^{i\Omega t}\right\} \qquad \text{(A.9)} \\
&+ 2Re\left\{E_{-1}^* E_1 e^{i2\Omega t}\right\} \\
&\equiv A_0 + A_1 \cos \Omega t + B_1 \sin \Omega t + A_2 \cos 2\Omega t + B_2 \sin 2\Omega t
\end{aligned}
$$

Next we model the shot noise process as a process of Poisson impulses with density $\lambda(t)$

$$\lambda(t) = A_0 + A_1 \cos \Omega t + B_1 \sin \Omega t + A_2 \cos 2\Omega t + B_2 \sin 2\Omega t \qquad \text{(A.10)}$$

Each impulse corresponds to the generation of one photoelectron in our photodetector, and the units of i_p are photoelectrons/second because of our definition (2.1) of the fields. A Poisson process $\mathbf{x}(t)$ is defined[5] as a process which is constant except for unit increments at random points in time $\mathbf{t}_i$, where the density of the points $\mathbf{t}_i$ is $\lambda(t)$, and the process of Poisson impulses $\mathbf{z}(t)$ is its derivative[6]

$$\mathbf{z}(t) = \frac{d\mathbf{x}(t)}{dt} \qquad \text{(A.11)}$$

i.e.,

$$\mathbf{z}(t) = \sum_i \delta(t - \mathbf{t}_i) \ . \qquad \text{(A.12)}$$

The autocorrelation of a non-uniform Poisson process is given by[7]:

$$R_{xx}(t_1, t_2) = \begin{cases} \int_0^{t_2} \lambda(t)dt \left[1 + \int_0^{t_1} \lambda(t)dt\right] & t_1 > t_2 \\ \int_0^{t_1} \lambda(t)dt \left[1 + \int_0^{t_2} \lambda(t)dt\right] & t_2 > t_1 \end{cases} \qquad \text{(A.13)}$$

and the autocorrelation of the derivative of a random process is given by[8]

$$R_{x'x'}(t_1, t_2) = \frac{\partial^2 R_{xx}(t_1, t_2)}{\partial t_1 \, \partial t_2} \quad . \tag{A.14}$$

Since $\mathbf{z}(t) = \mathbf{x}'(t)$ we have only to substitute into the equation above to find the autocorrelation we seek.

$$Rzz(t_1, t_2) = \frac{\partial^2 R_{xx}(t_1, t_2)}{\partial t_1 \, \partial t_2} \tag{A.15}$$

For $t_1 > t_2$,

$$R_{xx}(t_1, t_2) = \int_0^{t_2} \lambda(t)dt \left[1 + \int_0^{t_1} \lambda(t)dt \right] \tag{A.16}$$

$$\frac{\partial R_{xx}(t_1, t_2)}{\partial t_1} = \int_0^{t_2} \lambda(t)dt \, \lambda(t_1) \tag{A.17}$$

$$\frac{\partial^2 R_{xx}(t_1, t_2)}{\partial t_1 \, \partial t_2} = \lambda(t_1)\lambda(t_2) \tag{A.18}$$

Similarly, for $t_1 < t_2$,

$$R_{xx}(t_1, t_2) = \int_0^{t_1} \lambda(t)dt \left[1 + \int_0^{t_2} \lambda(t)dt \right] \tag{A.19}$$

$$\frac{\partial R_{xx}(t_1, t_2)}{\partial t_1} = \lambda(t_1) + \int_0^{t_2} \lambda(t)dt \, \lambda(t_1) \tag{A.20}$$

and we have

$$\frac{\partial^2 R_{xx}(t_1, t_2)}{\partial t_1 \, \partial t_2} = \lambda(t_1)\lambda(t_2) \tag{A.21}$$

again. However, there is a discontinuity in $\frac{\partial R_{xx}(t_1,t_2)}{\partial t_1}$ at $t_1 = t_2$, so

$$R_{zz}(t_1, t_2) = \lambda(t_1)\lambda(t_2) + \lambda(t_1)\delta(t_1 - t_2) \quad . \tag{A.22}$$

We can use this result to find the average autocorrelation of the inphase signal i_I:

$$\begin{aligned} R_{i_I i_I}(t+\tau, t) &= E\{\mathbf{i}_p(t+\tau)\cos\Omega(t+\tau)\mathbf{i}_p(t)\cos\Omega t\} \\ &= E\{\mathbf{i}_p(t+\tau)\mathbf{i}_p(t)\}\cos\Omega(t+\tau)\cos\Omega t \\ &= [\lambda(t+\tau)\lambda(t) + \lambda(t+\tau)\delta(\tau)]\cos\Omega(t+\tau)\cos\Omega t \end{aligned} \tag{A.23}$$

and of the inphase mixer output v_I

$$\begin{aligned} \overline{R_{i_I i_I}}(\tau) &= \frac{1}{T}\int_0^T R_{i_I i_I}(t+\tau, t)dt \\ &= \frac{1}{T}\int_0^T [\lambda(t+\tau)\lambda(t) + \lambda(t+\tau)\delta(\tau)]\cos\Omega(t+\tau)\cos\Omega t\, dt \; . \end{aligned} \tag{A.24}$$

The first term in the above will turn out to be irrelevant to our analysis; it is

$$\begin{aligned} &\frac{1}{T}\int_0^T [\lambda(t+\tau)\lambda(t)]\cos\Omega(t+\tau)\cos\Omega t\, dt \\ &\quad = \frac{1}{8}[2A_1^2 + \left(4A_0^2 + 4A_0A_2 + A_2^2 + B_2^2\right)\cos\Omega\tau \\ &\qquad + \left(A_1^2 + B_1^2\right)\cos 2\Omega\tau + \left(A_2^2 + B_2^2\right)\cos 3\Omega\tau] \end{aligned} \tag{A.25}$$

The second term is

$$\frac{1}{T}\int_{0}^{T}[\lambda(t+\tau)\delta(\tau)]\cos\Omega(t+\tau)\cos\Omega t\,dt = \frac{1}{2}\delta(\tau)\left(A_0+\frac{A_2}{2}\right) \tag{A.26}$$

To find the average power spectrum, we take the Fourier transform:

$$\begin{aligned}\overline{S_{i_I i_I}}(f) &= 2\int_{-\infty}^{\infty}\overline{R_{i_I i_I}}(\tau)e^{2\pi i f\tau}d\tau \\ &= A_0+\frac{A_2}{2} \\ &\quad + 4A_1^2\delta(2\pi f) \\ &\quad + \left(4A_0^2+4A_0A_2+A_2^2+B_2^2\right)\delta(2\pi f-\Omega) \\ &\quad + \left(A_1^2+B_1^2\right)\delta(2\pi f-2\Omega) \\ &\quad + \left(A_2^2+B_2^2\right)\delta(2\pi f-3\Omega)\end{aligned} \tag{A.27}$$

This power spectrum has four sharp components, one at DC[†], and three more at harmonics of the modulation frequency, as well as a broadband component. It is only the broadband component which interests us, since only it falls into the frequency range where we expect to detect gravitational radiation. The lowpass filter in our model of the detection system will leave this part of the noise spectrum unaffected, and will attenuate the very high frequency components. Hence we

---

[†] It is interesting to note that the DC component of the above spectrum will vanish or be very small if our servos are effective since A_1 and B_1 are proportional to the mixer outputs.

write

$$\begin{aligned}\overline{S_{v_I v_I}}(f) &= A_0 + \frac{A_2}{2} \\ &= |E_0|^2 + |E_1|^2 + |E_{-1}|^2 + Re\{E_{-1}^* E_1\}\end{aligned} \tag{A.28}$$

For the average shot noise spectral density at the inphase mixer output.

We take the same approach for the quadrature mixer output. We write "sin" instead of "cos" in (A.23) and (A.24), and evaluate the same integrals to get

$$\begin{aligned}\overline{S_{v_Q v_Q}}(f) &= A_0 - \frac{A_2}{2} \\ &= |E_0|^2 + |E_1|^2 + |E_{-1}|^2 - Re\{E_{-1}^* E_1\}\end{aligned} \tag{A.29}$$

We have, in the process of deriving this last result again thrown away sharp components in the spectrum at DC and at harmonics of the modulation frequency.

At either output, there could of course be light due to other sources than the idealized fields we have modeled here. Two examples are light present in orthogonal transverse modes because of mirror imperfectons, and light from an incandescent bulb which might be used to perform a shot noise calibration. When there is excess light on the photodetector, it frequently contributes only to A_0 and we write

$$\overline{S_{v_I v_I}}(f) = |E_{excess}|^2 + |E_0|^2 + |E_1|^2 + |E_{-1}|^2 + Re\{E_{-1}^* E_1\} \tag{A.30}$$

and

$$\overline{S_{v_Q v_Q}}(f) = |E_{excess}|^2 + |E_0|^2 + |E_1|^2 + |E_{-1}|^2 - Re\{E_{-1}^* E_1\} \tag{A.31}$$

where $|E_{excess}|^2$ is the additional optical power (in units of photons/second).

Cited References

[1] A. Papoulis, *Probability, Random Variables, and Stochastic Processes*, McGraw-Hill, New York, (1965).

[2] S. Whitcomb, unpublished, (1984).

[3] T. M. Niebauer et al., *Phys. Rev. A*, **43**, 5022, (1991).

[4] Papoulis, pp. 449-451

[5] Papoulis, p. 284.

[6] Papoulis, p. 287.

[7] Papoulis, p. 286 and equation (9–18).

[8] Papoulis, pp. 316–317 and equation (9–79).

Appendix B Specification of Allowable RMS Deviations from Perfect Resonance

B.1 Introduction

In this appendix we will see a set of specifications on allowed root-mean-square (RMS) deviations from resonance. Each specification is motivated by some mechanism through which a low-frequency (less than 10 Hz) deviation from resonance degrades the in-band (100 Hz to 10 kHz) signal-to-noise ratio either by reducing the signal strength or by increasing the noise. Since the signal to noise ratio at the output depends on a number of factors, only one of which is the deviation from resonance being considered, setting specifications on all of these factors involves an analysis of the costs and benefits of changing any one of the specifications. A thorough treatment of these issues is impossible here. It is likely that as research progresses and new information becomes available, the costs of changing certain specifications will be reassessed and it is possible that new mechanisms will be found which will impose additional constraints on the specifications.

Our goal here will be only to derive a sample set of specifications for illustrative purposes. It is hoped that although the numerical examples worked out in this text will lose their applicability as these numbers evolve, the analysis and design methods outlined will remain relevant and useful.

The remainder of this appendix deals with four mechanisms by which deviations from resonance can degrade interferometer performance. These involve the need to keep ample power circulating in the arm cavities, the need to prevent laser frequency or intensity fluctuations from producing a signal in the gravitational wave output, and the need to keep the antisymmetric output dark.

B.2 Power in the Arm Cavities

As we saw in chapter 3, the generation of audio sidebands on the carrier in the arm cavities produces the gravitational wave signal. A deviation from resonance that reduces the power in the arm cavities by 10% would reduce the gravitational wave signal strength by 5%. We will adopt this number as our specification on power stability in the arm cavities.

From (2.13) we know that the power in a cavity AD (as in Figure 2.3) is

$$\begin{aligned} P_{cav} &\propto \left| \frac{1}{1 - r_A r_D e^{-i\delta\phi}} \right|^2 \\ &\simeq \left| \frac{1}{1 - r_A r_D} \right|^2 \left| \frac{1}{1 + i\frac{r_A r_D}{1 - r_A r_D}\delta\phi} \right|^2 \end{aligned} \tag{B.1}$$

and $P_{cav} = 0.9 P_{cav\ max}$ for

$$\delta\phi \simeq 0.3 \frac{1 - r_A r_D}{r_A r_D} \tag{B.2}$$

We can derive a number of specifications by interpreting this for the different degrees of freedom.

If the arm cavity back mirrors move equal amounts in the same direction, then the relevant equivalent cavity is the one of Figure 3.2, which has a compound mirror consisting of the recycling mirror and a front mirror; then

$$\Phi_+ < (2)0.3\frac{1 - r_{F*R}r_B}{r_{F*R}r_B} \tag{B.3}$$

$$\simeq 3 \times 10^{-5} \ (radians)$$

For changes in ϕ_+ we take $r_A = r_F$ and $r_D = r_{c0}$; then

$$\phi_+ < 0.3\frac{1 - r_R r_{c0}}{r_R r_{c0}} \tag{B.4}$$

$$\simeq 0.01$$

These two specifications are similar to numbers quoted elsewhere[1].

B.3 Frequency Noise

D. Shoemaker[2,3] has shown that in order to avoid degrading the expected 99% frequency noise rejection ratio due to the symmetry of the arm cavities, we require*

$$\delta\Phi_I^2 - \delta\Phi_P^2 = \Phi_+\Phi_- < 2 \times 10^{-6} \tag{B.5}$$

If Φ_+ satisfies the specification above, then we require

$$\Phi_- < 0.07 \tag{B.6}$$

---

[*] Shoemaker derives the constraint assuming that all mirrors are stationary except for one arm cavity back mirror. His result is easily generalized to the one shown here.

B.4 Intensity Noise

Since the gravitational wave signal is proportional to the product of the laser power and Φ_-, low frequency deviations in the latter can couple in-band fluctuations in the former into the gravitational wave output. If 100 mW of laser power is picked off for the purpose of power stabilization, then the relative intensity noise (just after the pick-off, assuming that it is limited by shot noise in the reference photodetector) will be

$$\frac{S_I^{\frac{1}{2}}(f)}{I} = 2.8 \times 10^{-9}/\sqrt{Hz} \tag{B.7}$$

Now if the pick-off is located between the mode-cleaner (see footnote on p.8) and the recycling mirror, then the low-pass nature of the recycling cavity will reduce this noise at the beam splitter by about a factor of 50 ($\simeq \omega_c/\omega_{cc}$):

$$\frac{S_I^{\frac{1}{2}}(f)}{I} = 5.6 \times 10^{-11}/\sqrt{Hz} \tag{B.8}$$

If our target interferometer sensitivity is $4 \times 10^{-20} m/\sqrt{Hz}$, corresponding to $S_{\Phi_-}^{\frac{1}{2}} = 2 \times 10^{-12}/\sqrt{Hz}$, then we require

$$\Phi_- < 4 \times 10^{-2} \tag{B.9}$$

B.5 Dark at the Antisymmetric Output

If the light returning from the two arm cavities does not interfere perfectly destructively at the antisymmetric output, then the additional photons hitting the photodetector there will generate excess shot noise. It is believed that about 1% of the power returning to the beam splitter will arrive at the antisymmetric port photodiode because of mirror-imperfection-induced differences in beam shape or intensity. We adopt the requirement that no more than an additional 0.1% of the power returning to the beam splitter exit the antisymmetric port due to deviations in ϕ_- and Φ_-.

For $\Phi_- = 0$, $E_{anti\,0} = E_{r\,0} \sin\left(\frac{\phi_-}{2}\right)$, so we require

$$\sin^2\left(\frac{\phi_-}{2}\right) < 0.001 \tag{B.10}$$

and[†]

$$\phi_- < 6 \times 10^{-2} \tag{B.11}$$

To derive the specification for Φ_-, we note that the phase of the light returning to the beam splitter changes $N'_{arm} \equiv \frac{|r'_{c0}|}{r_{c0}} \simeq 130$ times faster for Φ_- than for ϕ_-, so that the specification must be tighter by this factor:

$$\Phi_- < 5 \times 10^{-4} \tag{B.12}$$

B.6 Summary

For our final set of specifications, we choose the tightest constraint on each of the degrees of freedom:

[†] Specifying separate limits on ϕ_- and Φ_-, in order to ensure darkness at the antisymmetric port, is a conservative strategy since the power leaving the antisymmetric port is actually proportional to $\phi_- + N'_{arm}\Phi_-$. A slightly more sophisticated numerical servo model than the one in Chapter 6 would show that the effect of residual deviations in ϕ_- is partially cancelled by opposing deviations produced in Φ_- by the loop feeding back to Φ_-.

$$\Phi_+ < 3 \times 10^{-5} \tag{B.13}$$

$$\phi_+ < 0.01 \tag{B.14}$$

$$\Phi_- < 5 \times 10^{-4} \tag{B.15}$$

$$\phi_- < 6 \times 10^{-2} \tag{B.16}$$

We demand that the RMS deviations in any of these degrees of freedom not exceed the above-listed bounds.

Cited References

[1] Technical Supplement to the LIGO Construction Proposal, internal LIGO document, (1993), p. B-3.

[2] D. Shoemaker, LIGO Working Paper #109, Internal LIGO document, (1991).

[3] D. Shoemaker, Modulation and topology: Deviations from resonance, Internal LIGO document, (1991).

Appendix C Alternative Feedback Configurations

In this appendix we consider two alternative feedback configurations and outline the consequences of adopting one of these configurations instead of the one described in Chapter 1.

The first modified configuration we consider is shown in Figure C.1; it differs from the configuration of Figure 1.7 only in that the quadrature phase signal from the isolator, instead of being fed back to the arm cavity mirrors, is fed back to the beam splitter and the recycling mirror in proportion such that l_I and l_P are changed in equal and opposite amounts.

Figure C.1 First alternative configuration: feed-back to beam splitter.

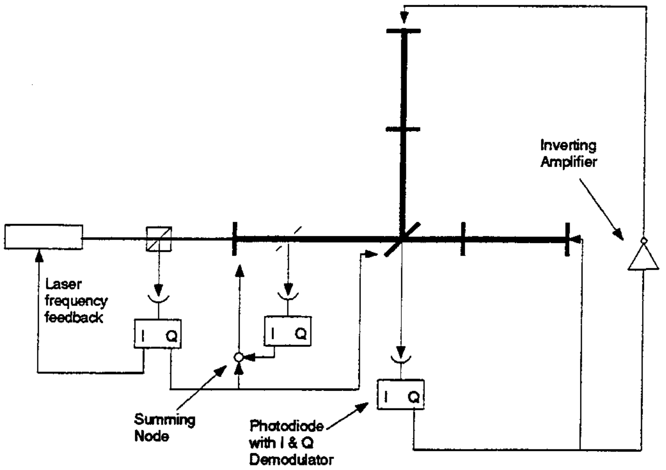

Let us find the response of the interferometer to this type of mirror motion. Since the beam splitter affects only l_P and since the beam splitter is angled at 45°, this occurs when the beam splitter is displaced by $\sqrt{2}$ as much as the recycling mirror ($\delta x_{BS} = \sqrt{2}(\delta x_R)$) and we let

$$\theta_- \equiv 2k\left(\delta x_R - \frac{1}{\sqrt{2}}\delta x_{BS}\right) \tag{C.1}$$

represent this combination of displacements. To derive the transfer function from θ_- to v_3 we first note that motion of the recycling mirror produces no signal here, and we choose to use that combination of beam splitter and recycling mirror motion which makes the audio sidebands propagating towards the two input mirrors exactly equal in amplitude and opposite in phase. This occurs for $\delta x_R = \frac{1}{r_R\sqrt{2}}\delta x_{BS}$. Then these audio sidebands will interfere destructively on the symmetric side of the beam splitter and constructively on the antisymmetric side, so that

$$H_{v_3\theta_-} \propto r_c(\pi + \omega\tau_{arm}) \tag{C.2}$$

$$H_{v_3\theta_-} = H_{\theta_-V_3DC}\frac{1 - \frac{r_f}{r_{c0}}\frac{i\omega}{\omega_c}}{1 + \frac{i\omega}{\omega_c}} \tag{C.3}$$

This result has no important effects on system performance since we still have $H_{v_3\theta_-} \ll H_{v_3\Phi_-}$.

Next we note that

$$H_{v_4\theta_-} = H_{v_4\phi_-} = H_{v_4\phi_-DC} \tag{C.4}$$

since, as before, the characteristic frequencies experienced by the sidebands are all very high.

Finally we look at the response in v_1 and v_2. The above combination of displacements, with $\delta x_R = \frac{1}{r_R\sqrt{2}}\delta x_{BS}$, must produce a frequency-independent signal in v_1 and v_2 because the audio sidebands present at these optical outputs have not interacted with the arm cavities. Let us find the difference between this displacement and θ_-. We want to consider the beam splitter and recycling mirror as a compound mirror which is a source of audio sidebands, and we want to solve for the proportion of displacement for which the sidebands generated in the direction of the perpendicular arm are exactly equal and opposite those generated in the direction of the in-line arm. Motion of the beam splitter alone produces sidebands propagating towards both arms, in the amount $\left[r_2^2 E_{retP}(T_p r_1) + t_p E_r r_2\right] x_{BS}/\sqrt{2}$ in the direction of the perpendicular arm and in the amount $r_2 E_{retP} T_p r_1 t_2 x_{BS}/\sqrt{2}$ in the direction of the in-line arm. The recycling mirror when displaced produces sidebands of the same size $r_1 E_f t_p r_2 x_R$ (if we take $r_2 = t_2$) propagating towards both arms. Setting the total sidebands propagating towards the two arms equal and opposite, and neglecting beam splitter loss, we get:

$$x_R = \frac{1}{2}\left(1 + \frac{1}{r_1 r_{c0} T_p}\right) x_{BS}/\sqrt{2} \qquad \text{(C.5)}$$

for the ratio of displacements which produces a frequency-independent response in v_1 and v_2. Since

$$H_{v_1\theta_-DC} = H_{v_2\theta_-DC} = 0 \qquad \text{(C.6)}$$

we must have

$$\begin{aligned} H_{v_1\theta_-} &= \frac{1}{2}\left(\frac{1}{r_1 r_{c0} T_p} - 1\right)\left[H_{v_1\dot{\phi}_+} - H_{v_1\dot{\phi}_+DC}\right] \\ &= \frac{1}{2}\left(\frac{1}{r_1 r_{c0} T_p} - 1\right) H_{v_1\dot{\phi}_+DC} \frac{N_1'}{N_1' - N_0'} \frac{\frac{s}{\omega_{cc}}}{1 + \omega_{cc}} \end{aligned} \tag{C.7}$$

and

$$H_{v_2\theta_-} = \frac{1}{2}\left(\frac{1}{r_1 r_{c0} T_p} - 1\right) H_{v_2\dot{\phi}_+DC} \frac{N_1}{N_1 - N_0} \frac{\frac{s}{\omega_{cc}}}{1 + \omega_{cc}} \tag{C.8}$$

These effects can be summarized by writing the new plant $\tilde{P}$ as follows

$$\tilde{P} = \left[\begin{array}{cccc} \multicolumn{2}{c}{P_+} & 0 & H_{V_1\theta_-} \\ & & 0 & H_{V_2\theta_-} \\ 0 & 0 & \multicolumn{2}{c}{\tilde{P}_-} \\ 0 & 0 & & \end{array}\right] \tag{C.9}$$

where $\tilde{P}_-$ differs from P_- only in its upper right element. The analysis and design methods presented in Chapter 6 still apply. The non-zero elements in the upper right sub-block represent additional noise summed into the common-mode subsystem from the differential subsystem. These will degrade the performance of the system. In a numerical analysis using the same controllers as in Table 6.6, the predicted performance is the same as in that example, except that in the Φ_+ loop the RMS residual deviation is increased to 1.5×10^{-5}. A word of caution is appropriate here. The specs derived in Appendix B implicitly assumed very-low-frequency deviations from resonance and their generalization to dynamic deviations is not obvious. Moreover, because of the method used to assess performance numerically, we implicitly changed the dynamic generalization of the performance specifications when we switched plants, and this is partly responsible for the degradation in predicted performance. Only a more careful derivation of the specifications on allowable deviations from resonance, which specifies, as a function of frequency, the constraints on mirror displacements or changes in laser optical frequency, can resolve this issue properly.

The second alternative configuration to consider involves no feedback to the arm cavity back mirrors[1]. Instead the front mirrors are driven. This is shown in Figure C.2.

Figure C.2 Second alternative feedback configuration.

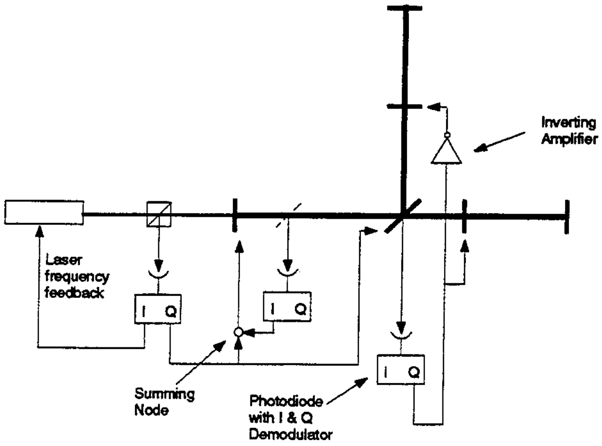

The corresponding plant matrix is

$$\tilde{\tilde{P}} = \begin{bmatrix} P_+ & & 0 & H_{V_1\theta_-} \\ & & 0 & H_{V_2\theta_-} \\ 0 & 0 & H_{V_3\Phi_-} - H_{V_3\dot{\phi}_-} & H_{V_3\theta_-} \\ 0 & 0 & H_{V_4\Phi_-} - H_{V_4\dot{\phi}_-} & H_{V_4\theta_-} \end{bmatrix} \qquad \text{(C.10)}$$

The main consequence of this change is to make the lower left element of $\tilde{\tilde{P}}$ comparable in magnitude to its lower right element. This means that residual deviations in loop 4 will produce a larger signal in loop 3. This effect is unlikely to be important since the specifications are tighter for deviations in loop 4 than in loop 3.

One additional consideration in analyzing these alternatives is that in the presence of mixer phase error, the common mode and differential subsystems become fully coupled. They can no longer be analyzed (as in Figure D.1) as two subsystems which are independent except that one injects noise into the other, since signals now flow in both directions. Both performance and stability can be affected.

Cited References

[1] L. Sievers, private communication, (1993).

Appendix D Effect of Mixer Phase Error

In this appendix, we will fill in the derivation of the effect of mixer phase error mentioned in Chapter 8. As mentioned there, the output v_4 is particularly vulnerable to this type of phase error because the inphase signal at the same photodetector is more sensitive to Φ_+ and to ϕ_+ than the quadrature phase is to ϕ_-. This error transforms the interferometer plant matrix from the block-diagonal form of equation 6.1 to the modified form[‡]

$$\tilde{P} = \begin{bmatrix} 1 & \epsilon_1 & 0 & 0 \\ 1 & \epsilon_2 & 0 & 0 \\ 0 & 0 & 1 & \epsilon_3 \\ K & K\epsilon_1 & \epsilon_4 & 1 \end{bmatrix} \tag{D.1}$$

where

$$K = \frac{\frac{\partial v_1}{\partial \Phi_+}}{\frac{\partial v_4}{\partial \phi_-}} \sin\beta \tag{D.2}$$

and β is the phase error in the local oscillator at the v_3 mixer. If we neglect the small coupling between loops 3 and 4, then the effect of this error can be analyzed using the block diagram of Figure D.1.

$$\begin{aligned} e_4 &= \frac{d_4}{1 - C_4} + [Ke_1 + K\epsilon_1 e_2]\frac{C_4}{1 - C_4} \\ &\simeq \frac{d_4}{C_4} + Ke_1 + K\epsilon_1 e_2 \\ &\simeq 2.5 \times 10^{-2} + 1.5 \times 10^{-2} \sin\beta + 6.5 \times 10^{-3} \sin\beta \end{aligned} \tag{D.3}$$

[‡] We neglect the frequency dependence of the plant since we seek only a rough estimate of the size of the effect.

Figure D.1 Block diagram used to analyze the effect of mixer phase error.

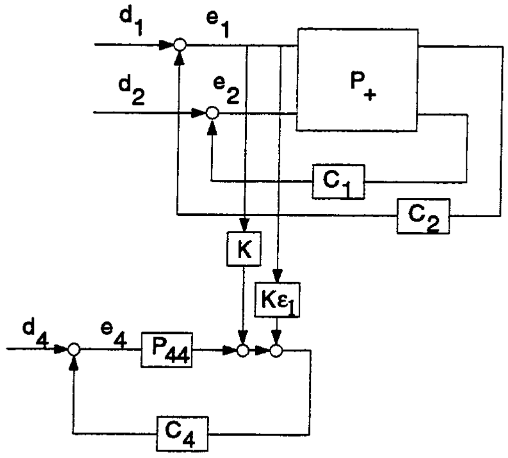

In the second line of this last equation, we have used the approximation that $|C_4| \gg 1$, and in the third line we have substituted values from our numerical example (where $K \simeq 2100 \sin \beta$). This is the result we use in Chapter 8.